DOCTORAL DISSERTATION

Study on Reductive Deposition of Thin Films Based on Ballistic Electron Incidence

Department of Electronic and Information Engineering,
Graduate School of Engineering
Tokyo University of Agriculture and Technology

Ryutaro Suda

Academic supervisor: Jun-ichi Shirakashi

Abstract

Thin film deposition using the reducing activity of ballistic electrons emitted from nanocrystalline silicon (nc-Si) diode has been investigated. Energetic electrons emitted from nc-Si electron emitters reduce positive ions in solution. First, thin group-IV film deposition was demonstrated by injecting ballistic electrons into a very small amount of semiconductor salt solution dripped on the emitter surface. Spectroscopic analyses revealed that when ballistic electrons were injected into $SiCl_4$ or $GeCl_4$ solution, thin Si or Ge films were deposited on the emitter surface. The Cl contamination of the deposited films was below the detection limit of EDX and XPS measurements. In the mixture solution of $SiCl_4$+$GeCl_4$, it was found that the SiGe thin film was also deposited.

Subsequently, a thin film deposition scheme on various substrates including insulating substrates was developed. In this method, by irradiating ballistic electrons to a solution-coated substrate, a thin film can be deposited on various substrates like a printing method. By irradiating ballistic electrons close to the target Si and SiO_2/Si substrates coated with the $CuCl_2$ solution, thin Cu films were deposited on the target substrates. It was revealed that ballistic electrons directly reduced the Cu^{2+} ions in the solution followed by thin film deposition. Based on this result, printing deposition of thin group-IV semiconductor films such as Si and Ge were performed. Thin Si and Ge films were deposited on the target Cu substrates as in the case of printing deposition of thin Cu films. Spectroscopic measurements revealed that the deposited thin film consists of very small nanoclusters. It is shown that the thin film deposition process of the ballistic printing method can be explained by using thermodynamic nucleation model and reaction-diffusion law.

Table of Contents

Abstract 1

Chapter 1 Introduction 4

1.1 Background 4
1.2 Advanced thin film deposition techniques 5
1.2.1 Dry techniques 5
1.2.2 Wet techniques 6
1.2.3 Others 7
1.3 Aims and objective of the present work 8

Chapter 2 Nanocrystalline silicon ballistic hot electron emitter and their applications 12

2.1 Introduction 12
2.2 Nanocrystalline porous silicon 12
2.3 Nanocrystalline silicon ballistic hot electron emitter 14
2.3.1 Emission mechanism and property 14
2.3.2 Possible applications 20
2.3.2.1 In vacuum 20
2.3.2.2 In atmospheric-pressure gases 22
2.3.2.3 In solution 22
2.4 Summary 26

Chapter 3 Reductive thin-film growth under dripping mode 27

3.1 Introduction 27
3.2 Experimental 27
3.2.1 Emitter fabrication 27
3.2.2 Deposition scheme 29
3.3 Results and discussion 30
3.3.1 Thin Si and Ge films 30
3.3.2 Thin SiGe films 36
3.3.3 Deposition rate 38
3.3.4 Structural and electrical properties 40
3.4 Summary 42

Chapter 4 Ballistic-electron printing of thin films **43**
4.1 Introduction 43
4.2 Experimental 43
4.3 Results and Discussion 45
4.3.1 Thin Cu films 45
4.3.2 Thin Si and Ge films 50
4.3.3 Comparison with dripping mode 56
4.4 Summary 57

Chapter 5 Deposition mechanism **58**
5.1 Introduction 58
5.2 Modeling 58
5.3 Thermodynamic analysis 64
5.4 Mass transport 68
5.5 Further evidence 77
5.6 Characteristic features 79
5.7 Summary 85

Chapter 6 Conclusions **86**
6.1 Summary of each chapter 86
6.2 Future prospects 88

References **89**

Publications list **96**

Acknowledgements **99**

Chapter 1

Introduction

1.1 Background

We own so many various semiconductor integrated circuits like laptop computers, smartphones, and other consumer electronics. The improving the functionality of semiconductor integrated circuits has been supported by lithography and thin film deposition technologies since Fairchild Semiconductor International, Inc. had developed the first silicon based integrated circuit in 1960s [1]. Modern circuits has required that metallic, semiconducting, and insulating layers in excess of twenty are deposited with appropriate thickness and quality [1]. As a method of depositing these thin films, a dry process such as chemical vapor deposition (CVD) or physical vapor deposition (PVD) technique has been mainly used in semiconductor industry [1-11].

It is often thought that integrated circuits are manufactured on rigid substrates such as glass and Si wafers, but it can also be fabricated on flexible materials like plastic which can be stretched and bent. Such a device is called a flexible device [12]. Various applications have already been proposed, such as wearable sensors and electronic paper, and thus it is anticipated that they will become big markets in the future [13]. (Fig. 1.1) From the viewpoint of production cost and compatibility with a substrate material, these flexible devices are often fabricated using printing techniques (inkjet or screen printing, etc.) and organic semiconductors [12]. By contrast, many inorganic semiconductors such as Si and Ge exhibit high carrier mobility and excellent stability. However, current thin Si and Ge film deposition techniques often require high temperature and high vacuum environment, resulting in high production cost. In addition, the plastic substrate often used for flexible devices plastically deforms above 200 °C [14]. Therefore, it is particularly important to deposit high-quality inorganic semiconductor films on various flexible substrates such as metal foils, plastic sheets, and papers at a low temperature like a printing method.

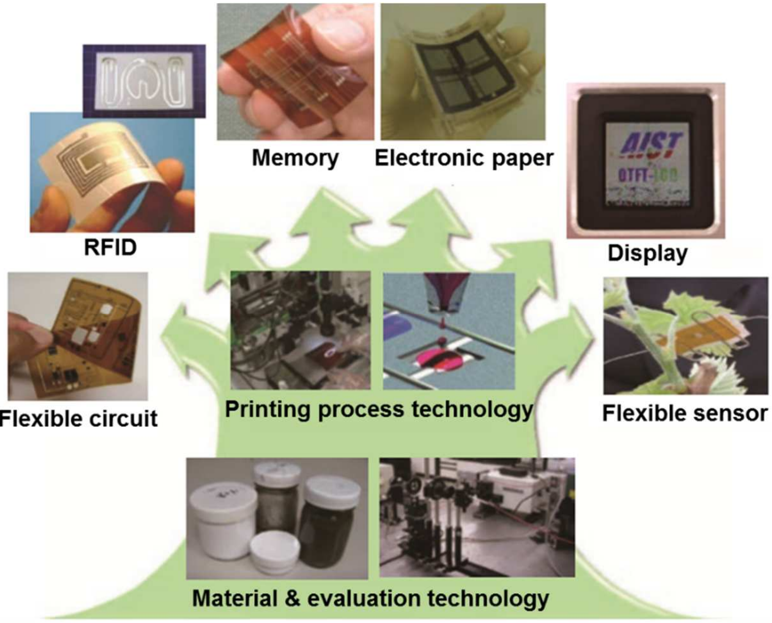

Figure 1.1 Research and development trend of flexible electronics. Development of material, evaluation, process, and device technologies has been desired to realize the next generation information terminal equipment [13].

1.2 Advanced thin film deposition techniques

Thin film deposition has been conducted using either physical vapor, chemical vapor, or electrochemical process in correspondence to substrate materials. Especial attention has been paid on thin film deposition technique onto flexible substrates for both organic and inorganic semiconductors, as flexible electronics has intensively been developed in recent 20 years [14]. In this section, research trends in thin film deposition methods of inorganic semiconductors are summarized mainly for flexible substrates.

1.2.1 Dry techniques

CVD techniques are most widely used for depositing silicon [1-11]. Among them, thermal CVD (T-CVD) has a long history, and until the 1970s it had been used to deposit all epitaxial silicon films. Even in the current semiconductor process, T-CVD method has been still used in the formation of dielectric films. Thin film deposition proceeds through molecule decomposition induced by

thermal energy, so T-CVD basically has a high process temperature (~1000 °C). The high-temperature processes may affect the junction depth, junction abruptness, and gate performance of transistors. Thus, as the importance of low temperature deposition is increased in the semiconductor process, alternative plasma-enhanced CVD (PE-CVD) has been mainly used. In addition, although ordinary amorphous Si (a-Si) film deposition by PE-CVD is performed at 250 °C [1,14], a thin a-Si film deposition at low temperature has also been studied for flexible electronics. For example, a-Si was deposited on a polyethylene terephthalate (PET) substrate at 75 °C by radio frequency plasma-enhanced CVD (RF-PECVD) to fabricate thin-film transistors (TFTs) [14]. In general, when the film deposition temperature is lowered, the mobility of the a-Si thin film is remarkably decreased, and then the device performance tends to deteriorate. Although it is possible to improve the mobility by using a laser annealing process [15], it is necessary to a buffer layer such that the heat is not transferred to the plastic substrate.

PVD techniques such as sputtering and vacuum deposition have been mainly used for metal layer formation in semiconductor manufacturing [1]. An oxide semiconductor such as ZnO can be formed at room temperature by PVD such as magnetron sputtering [16] or laser pulse deposition [17]. Polycrystalline ZnO thin films have been successfully formed on polyimide sheets by laser pulse deposition [17]. Since these materials have a large band gap and are transparent with respect to visible light, application as TFTs for flat panel display has been considered. Although the dry processes (CVD and PVD) has been widely used as a semiconductor film deposition technique in general, it requires a high vacuum, so the cost of film deposition tends to be high.

1.2.2 Wet techniques

Electroplating has been intensively studied by many researchers for advanced thin film deposition. This wet process is very simple and cost effective in comparison with dry processes such as CVD and PVD [18]. For example, in the recent ultra-large-scale integration (ULSI) technology, Cu films are formed by electroplating in order to form wiring layers [1,18-20]. Electroplating of thin semiconducting films has also been studied over many years [18]. Since Si and Ge have a very high

reduction potential, these compounds react with water and immediately form oxides. For this reason, it is necessary to use a non-aqueous solvent for electroplating of Si. Electroplating of Si and Ge using molten salts [21-23], organic solvents [24-32], and ionic liquids [33-36] has been reported. Application studies on electroplating of silicon have been conducted in the fields of solar cell [37] and lithium ion battery anode [38-40]. Deposited thin silicon films are, however, still poor in the film quality and crystallinity compared with those obtained from dry processes [18].

Thin film deposition technology using a solution has the potential to realize a low cost process without vacuum system by combining with spin coating and printing technology [12]. Actually, deposition of a-Si or oxide semiconductors has been studied using ~~a~~ solution processes [41,42]. In these methods, a substrate coated with a mixture solution of cyclopentasilane and toluene [41], or a solution containing chemically synthesized ZnO nanoparticles [42] is annealed. However, in order to obtain a high carrier mobility film by these methods, it is necessary to set the sintering temperature to be higher than the decomposition temperature of plastics [41,42], and thus at present it is difficult to use it as a flexible device fabrication technology.

1.2.3 Others

Chemically synthesized nanowires and nanoribbons with single crystals have high mobility. Various nanowires and nanoribbons (Si, Ge, III-V group, and II-VI group semiconductors) for TFT channels have already been reported [14]. However, since the characteristics of these devices depend on the number of nanowires in the channels, there are variations in the characteristics between the devices. In addition, the mobility of one nanowire is as large as that of a single crystal, but the total output current of a device is small.

In recent years, a technique of taking out thin wire/ribbon structures from a single crystal substrate and transferring it to a plastic substrate has been reported [43]. In this method, since the wires and the ribbons were taken out from the high quality substrate by etching technology, the performance of the fabricated devices was very high. Since the basic processes are done on the mother wafer, there is no temperature limitation for device fabrication. Although the fabricated devices have

high performance similar to that of semiconductor integrated circuits, since the existing semiconductor processes are used, the cost of the process is higher than that of the printing method.

While the accelerated focused electron beam is usually used for microscope or lithography, possible applications to thin film deposition has also been investigated [44-47]. This deposition technique is called the electron-beam-induced deposition (EBID). A precursor gas such as metalorganic molecular are introduced into a scanning or transmission electron microscope chamber, and then high-energy electron irradiation leads to decomposition of adsorbed precursor gas on the substrate followed by thin film formation. The advantage of EBID is that fine patterns can be directly formed with high resolution. In fact, Pt dots with a width of 10 nm or less and 10 nm Pt nanowires were formed by EBID [46]. In addition, since the process is performed at room temperature, it is possible to form a thin film on a plastic substrate, and thus formation of Co, W, and Pt nanowires on polycarbonate (PC) has been reported [48]. However, there remains a serious problem in EBID that the purity and structure of the deposited thin films are poor because of incorporation of decomposed species into the thin films and significant irradiation damages during the process [46].

1.3 Aim and objective of the present work

As mentioned in the above section, it is required to deposit thin films at low temperatures on varied substrates including plastic flexible substrates. In this study, an alternative thin film deposition method is proposed utilizing the high reducing activity of ballistic hot electrons emitted from nanocrystal line silicon (nc-Si) diode [49-53]. In this method, a salt solution containing an objective material such as copper dichloride ($CuCl_2$), silicon tetrachloride ($SiCl_4$), or germanium tetrachloride ($GeCl_4$) is coated on a target substrate, and then irradiated with ballistic electrons. The electrons injected into the solution preferentially reduce the target ions followed by thin film deposition. The schematic of ballistic electron printing is shown in Fig. 1.2. In conventional electroplating in $SiCl_4$ or $GeCl_4$ solution, it is necessary to apply a voltage higher than the respective electrochemical window of 3.76 or 1.24 V, respectively, as indicated in Fig. 1.3. As a consequence, unnecessary reactions

possibly proceed simultaneously with electroplating. In addition, as described in the above section, the deposited thin film is contaminated due to gas evolution and decomposition of solvent caused by the oxidation reaction at the anode electrode. In contrast, the electrons emitted from the nc-Si diode have energies high enough to reduce Si^{4+} or Ge^{4+} ions with a large reduction potential. It is noted that since the irradiated electrons directly reduce positive ions, it does not require an anode electrode in principle. From this feature, it looks that a thin film patterning can be achieved like a printing method by designing the electron irradiation area. It is expected that thin films with less contamination compared to electroplating or EBID can be formed due to no gas evolutions at the anode electrode.

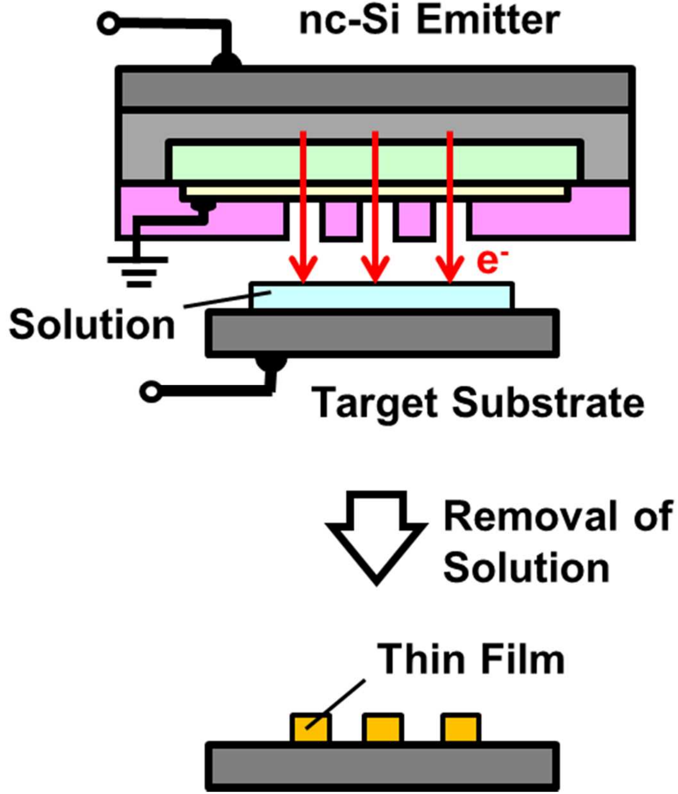

Figure 1.2 Schematic illustration of ballistic printing scheme using nc-Si ballistic hot electron emitter. Thin group-IV semiconductor films can be formed like printing method such as inkjet and screen printing.

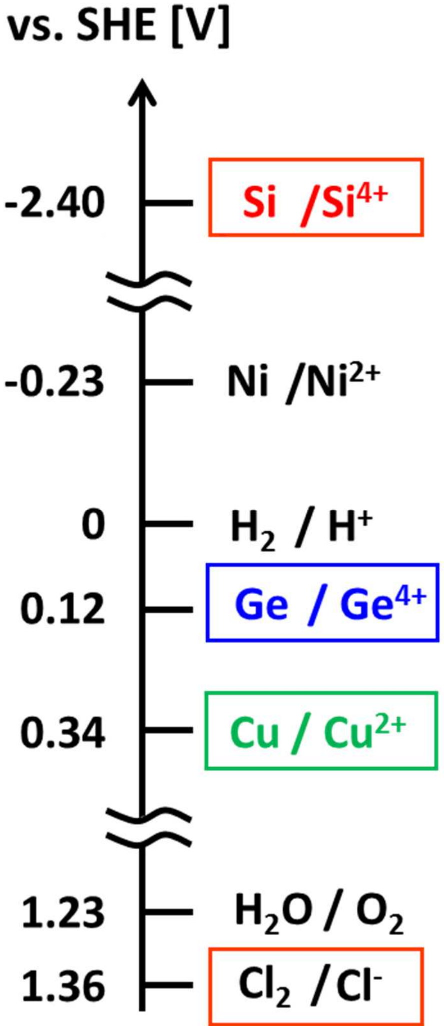

Figure 1.3 Redox potential of each ion with respect to the standard hydrogen electrode [52,53].

In this research, it is pursued to print thin group-IV semiconductor films such as Si and Ge by low temperature process utilizing nc-Si ballistic hot electron emitter. The overview of this research is shown in Fig. 1.4. The structure of this paper is as follows. In chapter 2, the operating mechanism of nc-Si ballistic hot electron emitter, fabrication method, and features are discussed. The chapter also describes the previous research on various application of ballistic electron emitters such as flat panel display, electron beam lithography, and thin film deposition. Subsequently, ballistic electrons are injected into a small amount of solution dripped on the emitter surface, and then thin film deposition due to the reducing activity of ballistic electrons are verified in Chapter 3. In addition to thin film deposition of Si and Ge, the results of deposition of SiGe thin film are also described. Based on the

results of Chapter 3, the printing deposition of Cu, Si, and Ge films in the setup of Fig. 1.2 is demonstrated in Chapter 4. A simplified deposition model of the printing mode is provided employing classical nucleation theory and reaction-diffusion law (Chapter 5). Finally, the summary of this research is described in Chapter 6.

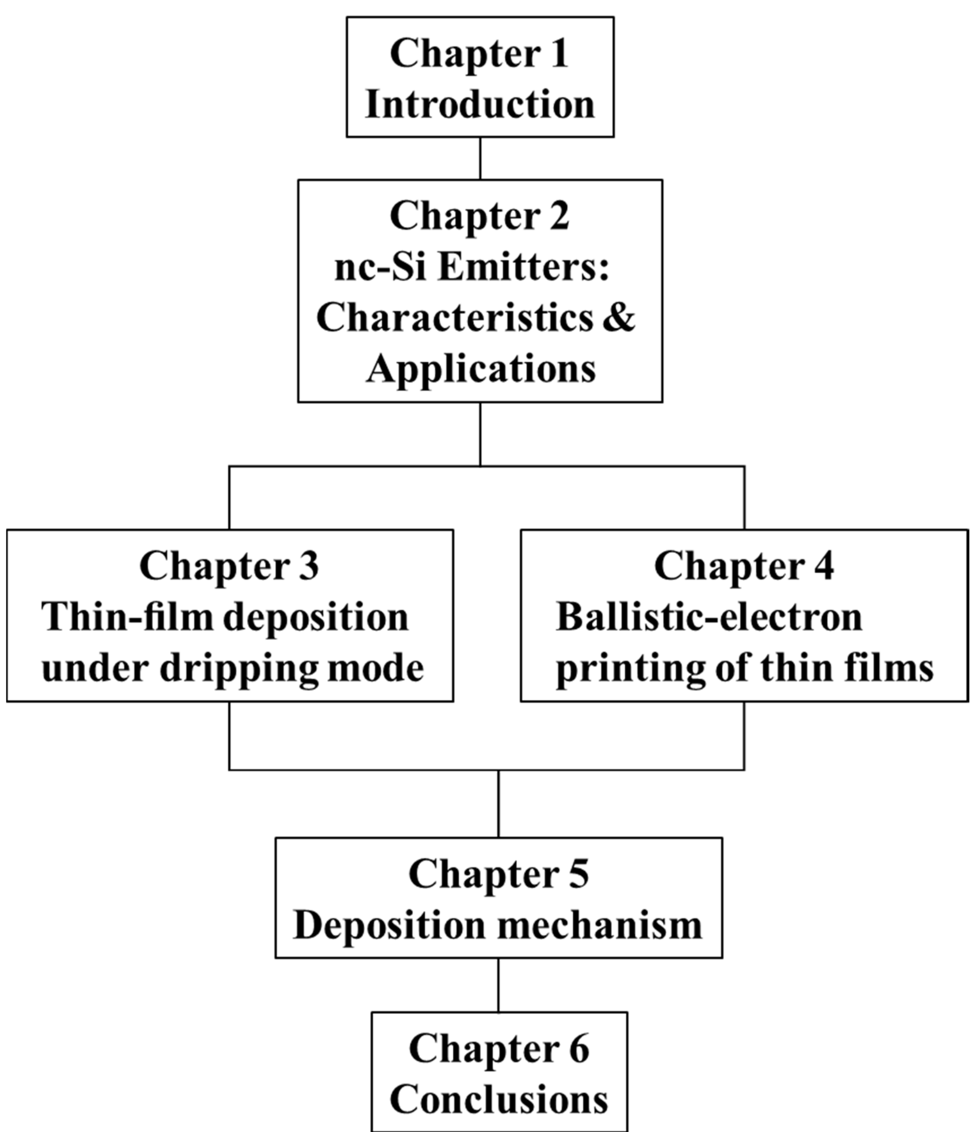

Figure 1.4 The overview of this research.

Chapter 2
Nanocrystalline silicon ballistic hot electron emitters and their applications

2.1 Introduction

This chapter briefly summarizes the fabrication method, operation mechanism, characteristic features, and applications of nanocrystal line silicon (nc-Si) ballistic hot electron emitter. The nc-Si layer, which acts as an electron drift layer, is fabricated electrochemically by anodization process. In this layer, electrons are accelerated via multiple tunneling through nc-Si dots and transport under a ballistic mode. As a result, ballistic electrons with high directivity are uniformly emitted from the surface electrode. From these features, it can be applied not only to electron sources for flat panel displays and electron beam lithography but also to thin film deposition.

2.2 Nanocrystalline porous silicon

When a Si wafer substrate is anodized in a hydrofluoric acid (HF) solution, elution reaction of Si progresses self-organically, and then a porous Si layer is formed [54], as shown in Fig. 2.1. The structure of the porous Si layer can be controlled by the HF concentration, the carrier type and resistivity of the Si wafer, and the current density of anodization [55]. In the porous Si layer, the optical, thermal, and chemical properties change dramatically compared to bulk Si due to the increase in the Si surface area and the quantum confinement effect [54,55]. Although Si is an indirect transition semiconductor and thus does not emit visible light, it has been confirmed that porous Si emits visible light by band gap widening and its emission wavelength can be controlled from red to blue [56]. Also, both of the thermal conductivity and the heat capacity of the porous Si are remarkably lowered due to the carrier depletion [55]. By utilizing these properties, it is possible to apply to visible light emitting devices [56] and speakers using thermo-acoustic effect without mechanical vibration [57].

Properties of porous Si are summarized in Table 2.1. On the other hand, when the nanoporous Si layer is oxidized under appropriate conditions, a chain structure is formed in which nanocrystal line Si (nc-Si) dots are separated by thin oxide films. In this structure, the size of nc-Si dots is smaller than the mean free path of electrons in silicon (~4 nm), so that the electrons in the nc-Si layer are significantly suppressed in scattering, and thus exhibit ballistic behavior [58]. The mean free path of electrons in the nc-Si layer is greatly increased. Using this effect, it is possible to fabricate an electron emitter in which the nc-Si layer act as an electron drift layer. Details of the nc-Si emitter are described in the next section.

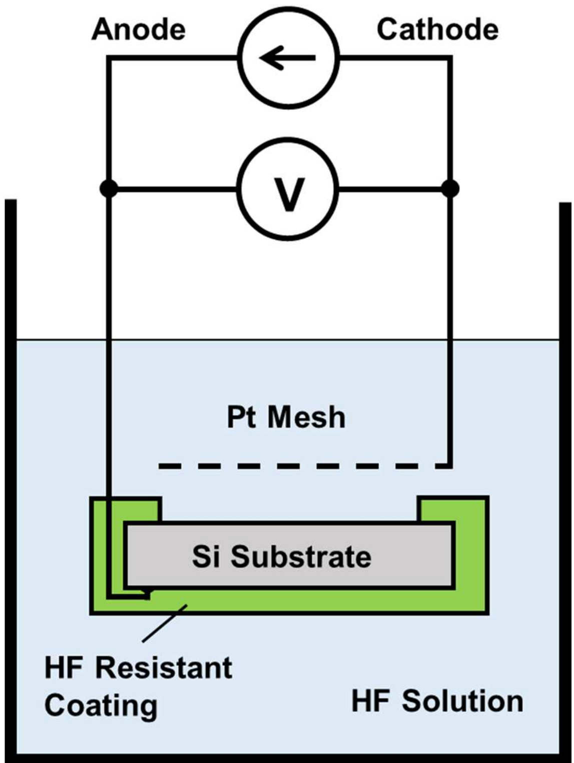

Figure 2.1 Schematic illustration of anodization for porous silicon production. The structure of the porous silicon can be controlled by HF concentration, the current density, and the carrier type and resistivity of the Si substrate.

Table 2.1 Characteristic features of nanocrystal line silicon [56-58].

Function of nc-Si			Function
Confinement	**Bandgap**	↗	**Visible luminescence**
Field effect	**Effective electron drift length**	↗	**Ballistic electron emission**
Depletion	**Thermal conductivity, heat capacity**	↘	**Thermo-acoustic effect**

2.3 Nanocrystalline silicon ballistic hot electron emitter

2.3.1 Emission mechanism and property

The schematic of the nc-Si ballistic hot electron emitter is shown in Fig. 2.2. The electron emitter consists of Au surface electrode / nc-Si layer / n^+-Si wafer substrate / Al back contact which has a structure similar to metal-insulator-semiconductor (MIS) diode [49]. The inset shows transmission electron microscope (TEM) image of the nc-Si layer. It seems that nc-Si dots are connected with a thin oxide film in between. When a positive bias is applied to the Au surface electrode of the emitter, electrons are injected from the Si substrate into the nc-Si layer. The electrons in the nc-Si layer are accelerated via multiple tunneling through the nc-Si dots. Finally ballistic hot electrons are emitted through the surface electrode.

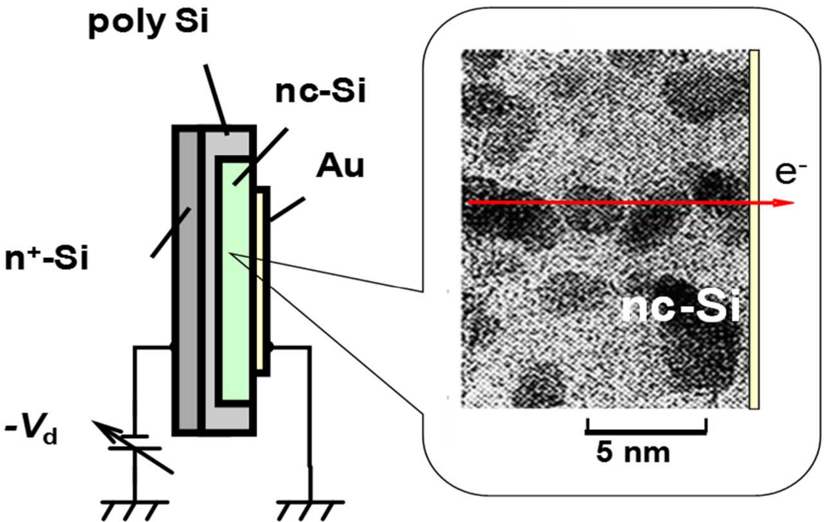

Figure 2.2 Schematic illustration of the device structure of nc-Si ballistic hot electron emitter. By applying a positive bias voltage to the Au surface electrode, ballistic electrons are emitted through the surface electrode. The inset shows the TEM image of the nc-Si layer [49].

Figure 2.3 shows *I-V* characteristics of the nc-Si emitter. Electron emission starts from the vicinity of the applied voltage of 6 V, and electron current density of 100 μA/cm^2 is obtained at 16 V. The Fowler-Nordheim (FN) plots obtained from Fig. 2.3 are shown in Fig. 2.4. The linear relationships suggest that the electron emission is basically originated from the field induced tunneling in the nc-Si layer. Figure 2.5 shows the energy distribution of electrons emitted from the nc-Si emitter at each bias voltage. It can be seen that at an applied voltage of 14 V, electrons with energy of 6 eV are emitted at room temperature. The ballistic behavior in the energy distribution becomes more apparent at a low temperature of 100 K.

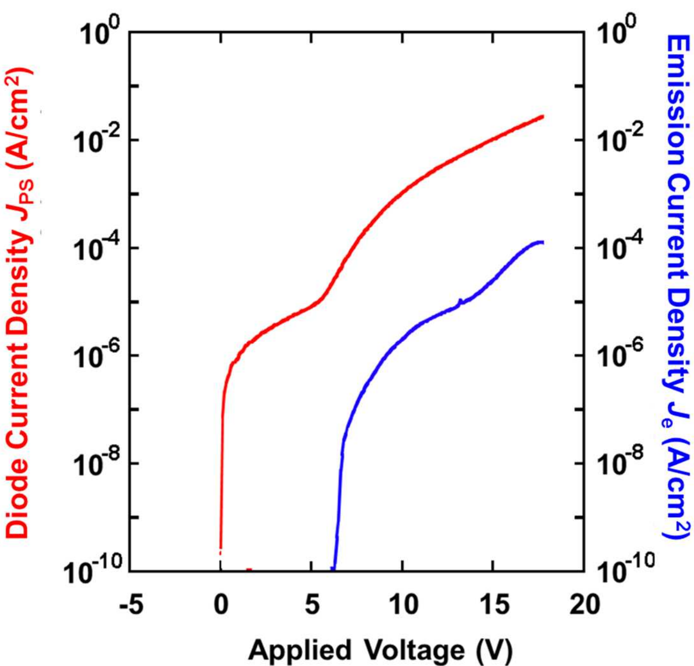

Figure 2.3 *I-V* characteristics of nc-Si emitter. The electron emission starts at 6 V, and the emission current density increases with the increasing the applied voltage [49].

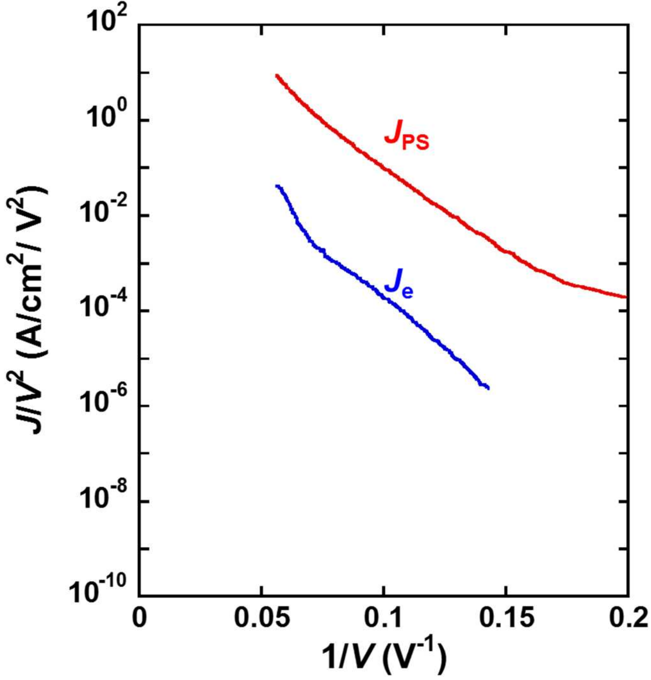

Figure 2.4 The FN plots obtained from the *I-V* characteristics in Fig. 2.3. Each plot properly shows a linear relationship [49].

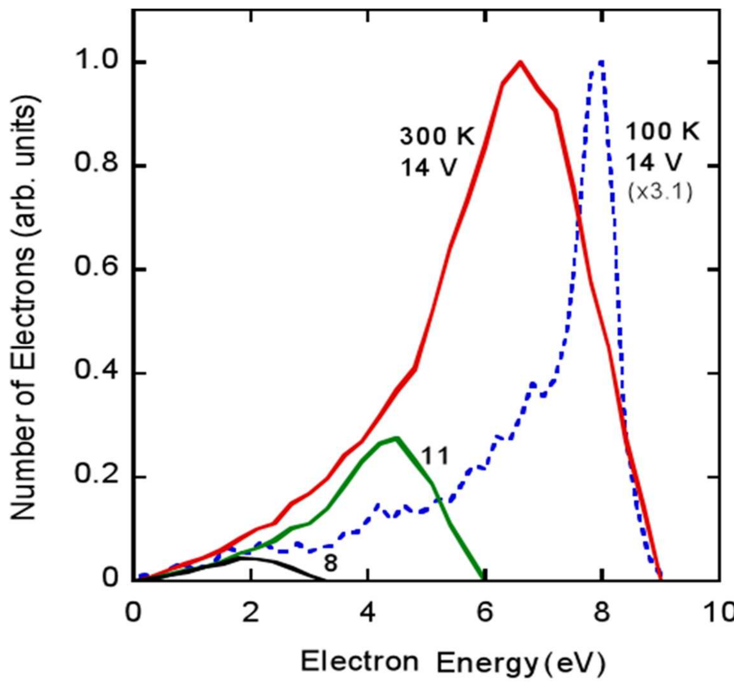

Figure 2.5 Energy distribution of ballistic electrons emitted from nc-Si diode in each bias voltage. At a temperature of 100 K, the energy peak shifts to the high energy side [49].

Similar properties were also seen in nc-Si emitters fabricated by dry process [59]. Also, the emission electron current strongly depends on the film thickness of the Au surface electrode. The thinner the film thickness, the more exponentially the emitted electron current increases, as shown in Fig. 2.6 [59]. In the graphene surface electrode with a thickness of about one atomic layer, electron scattering at the surface electrode is significantly suppressed, and a sharp energy distribution is obtained even at room temperature [60].

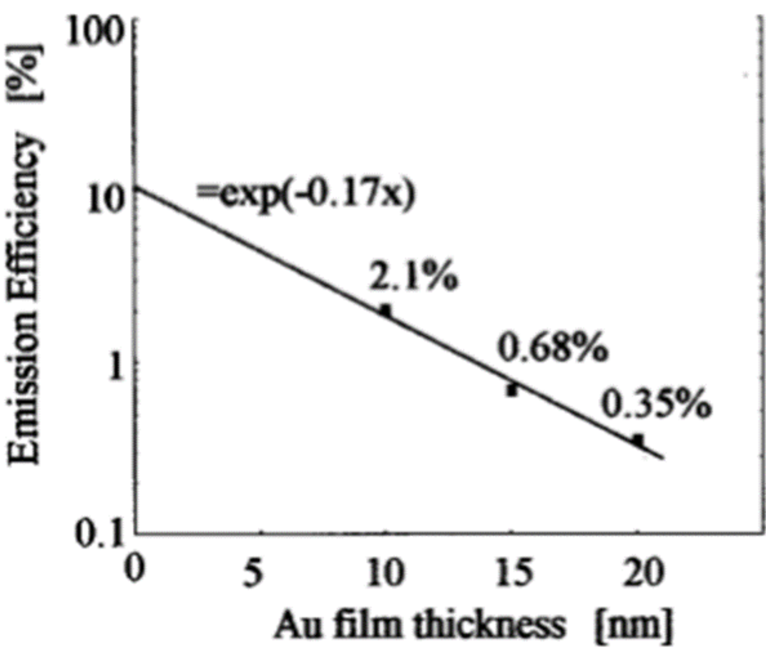

Figure 2.6 Relationship between the electron emission efficiency and the film thickness of Au surface electrode observed in an nc-Si emitter [59].

The conduction mechanism of electrons in the nc-Si layer was described by an atomistic tight-binding combined with semi-classical Monte Carlo simulation [61]. According to the simulation study, in the chain structure of silicon nano-dots separated by a thin oxide film (Figs. 2.7(a) and 2.7(b)), the electronic state in the low energy level is discretized, and additionally, the optical-phonon scattering is suppressed. As a result, the electrons in the nc-Si layer tunnel to the next dot before the energy relaxation. The simulation results show that the acoustic-phonon scattering is further suppressed at a low temperature of 100 K or less, and the ballistic behavior of electrons becomes more apparent, as shown in Figs. 2.8(a) and 2.8(b) [61]. The simulation results were supported by the time of flight measurement [62]. It was estimated that the mean free path of electrons in the free standing film of nc-Si is 1.6 μm, which value is much larger that of crystalline silicon.

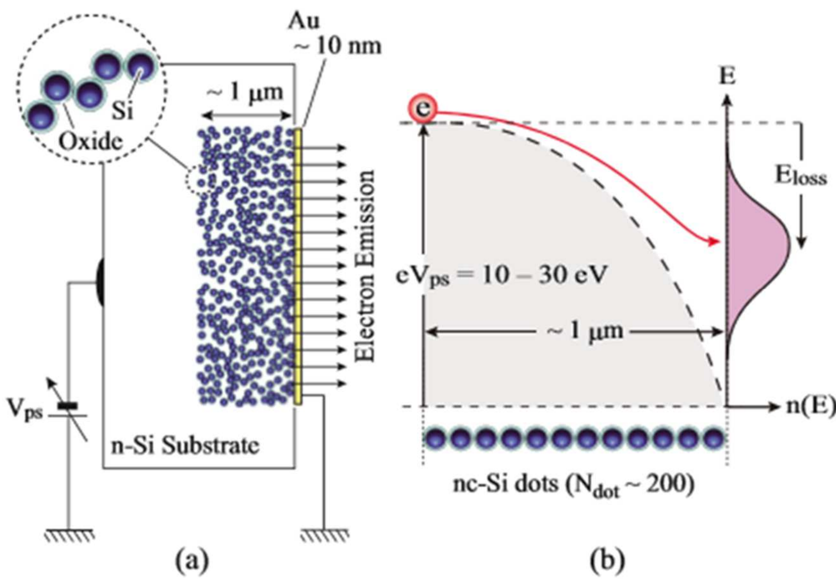

Figure 2.7 (a) Schematic illustration of the nc-Si diode. Electrons are emitted through the surface electrode under a positive bias V_{PS}. Conduction band profile and electron energy distribution at the diode surface, $n(E)$, are shown in (b). Here, the energy difference between the Fermi level of the substrate and the peak energy of the electron distribution $n(E)$ is defined as the energy loss E_{loss} [61].

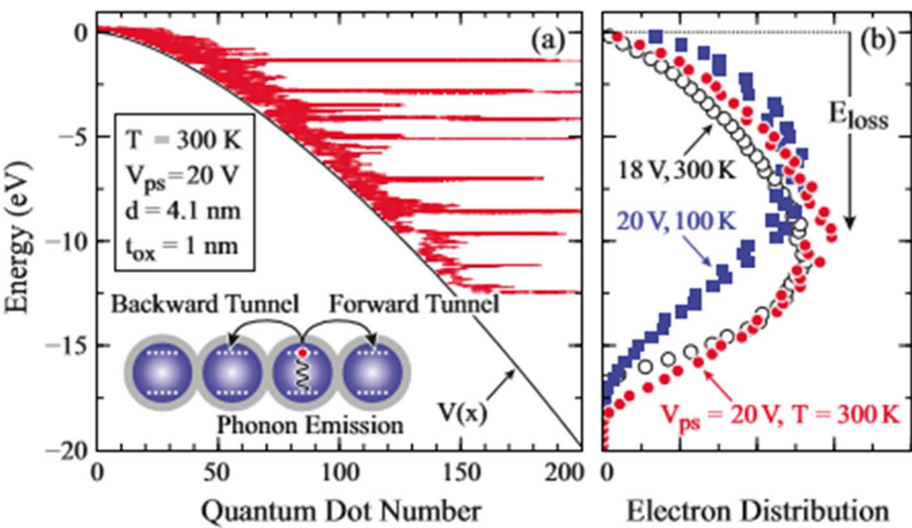

Figure 2.8 (a) An example of calculation result of electron trajectory with potential profile. A schematic illustration of the simulation model for the nc-Si dot array is shown in the inset. The right-side shows the electron energy distribution at the diode surface [62].

2.3.2 Possible applications

Since the nc-Si ballistic electron emitter is a planar structure, electrons uniformly emit from the surface electrode with high directivity. In addition to these features, due to the above mechanism, the electron energy is much higher than thermalized electrons emitted from conventional electron emitters. Therefore, the nc-Si emitters can operate not only in vacuum but also in air and solution [49]. In these media ballistic electrons physically and chemically act on substances in the medium. Characteristic features of nc-Si emitter are summarized in Table 2.2. The application of the nc-Si emitter in each medium is summarized below.

Table 2.2 Characteristic features of nc-Si ballistic hot electron emitter [49].

	nc-Si emitter	Conventional electron emitter
Energy	5～7 eV	~ kT
Angle	Directional	Dispersive
Mode	Surface	Point
Media	Vacuum, Air, Solutions	High vacuum

2.3.2.1 In vacuum

Flat panel display is an application utilizing the nc-Si ballistic hot electron emitter [63]. When ballistic electrons are irradiated on the phosphor, light is emitted with the same principle as cathode ray tube (CRT). By arraying a large number of nc-Si emitters in two dimensions, it is possible to fabricate a flat panel display with the same motion picture performance and contrast as CRT. In fact, prototype full color display panels with diagonals of 7.6 inch, with pixel counts of 336 (RGB) × 252 pixels, respectively, have been fabricated, as shown in Fig. 2.9 [63].

Figure 2.9 Emission image of fabricated 7.6-in.-diagonal prototype model [63].

This emitter can also be used as an electron source of an electron beam lithography. In 1:1 electron projection lithography using nc-Si emitter as an exposure source, the formation of a line pattern of 30 nm or less in the region of 0.2×0.2 μm^2 was reported by Koshida et al. despite the low acceleration voltage (5 kV) [64]. Similar to the application of the electron source to the flat panel display, it is possible to realize a maskless multi-beam electron beam exposure system (Fig. 2.10) with high throughput and high resolution by arraying the electron emitters in two dimensions [65,66]. In this system, 100×100 emitter arrays (each irradiation area is 10×10 μm^2) were fabricated on a Si substrate, and every emitter was connected with the LSI driver using through-silicon-via (TSV) interconnect technology [65]. 1:1 electron projection lithography using this emitter array has already been reported [67], and an electron optics dedicated to the emitter array has been simulated for the realization of reduced projection exposure [68].

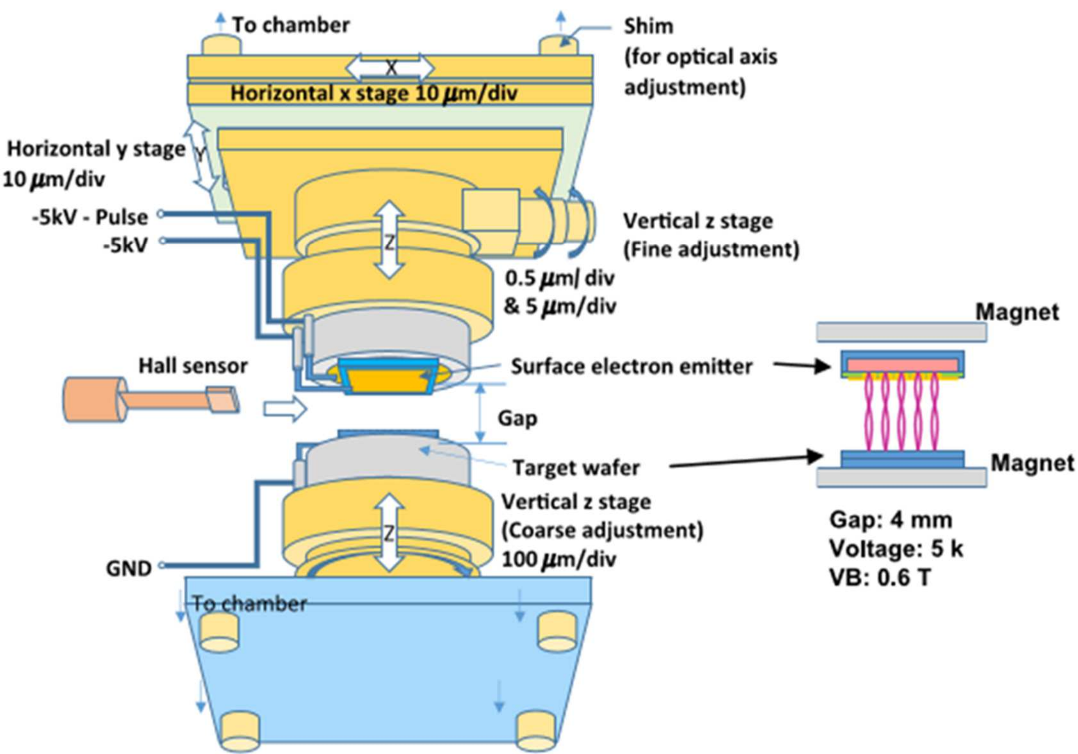

Figure 2.10 Schematic illustration of a developed 1:1 multi-beam exposure system using active matrix consisting of nc-Si emitter array [65].

2.3.2.2 In atmospheric-pressure gases

Ballistic hot electrons behave as an excitation source in low vacuum to atmospheric pressure [49]. For example, when an nc-Si emitter is operated in Xe gas, ballistic electrons excite Xe molecules and generate ultraviolet light [69]. In the atmosphere, emitted ballistic electrons cause dissociative electron attachment to oxygen molecules in the atmosphere to generate negative ions [70,71].

2.3.2.3 In solution

One of the important features of nc-Si emitter is that ballistic hot electrons have a highly reducing activity when injected into solution [49]. Since electrons are directly injected into the solution, unlike a conventional electrochemical reaction, an oxidation reaction at the counter electrode is not required. Therefore, in pure water, ballistic electrons directly reduce only hydrogen ions followed by H_2 gas generation without byproducts such as oxygen [72,73]. It has also been

confirmed by cyclic voltammogram measurements that when the electron source was driven in pure water, the ionic conduction current in the solution increased [72]. In addition, due to hydrogen evolution, the concentration of hydroxide ions (OH^-) in the solution increased, and then the pH shifted to the alkaline side, as shown in Fig. 2.11 [73].

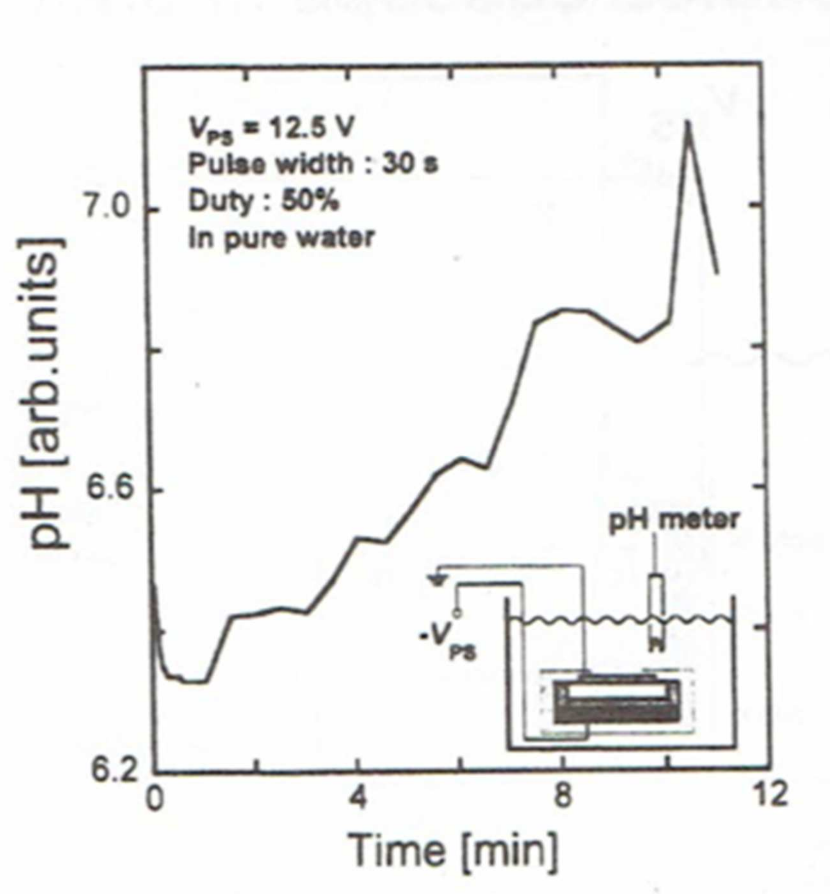

Figure 2.11 Time evolution of pH value during the operation of nc-Si ballistic hot electron emitter in pure water. The inset shows the experimental set up. A pulse-driven mode was employed here with an amplitude, width, and duty ratio of the bias voltage being 12.5 V, 30 s, and 50%, respectively [73].

In a metal-salt solution, since ballistic hot electrons preferentially reduce metallic ions, the thin metallic films are deposited on the emitter surfaces [49]. As in the case of hydrogen generation, unlike electroplating, this process proceeds with neither gas evolution nor byproducts at the counter electrode, and thus can be expected to form a thin film with less contamination compared to electroplating. It has been reported that ballistic electrons are injected into each of $CuSO_4$, $NiCl_2$,

$CoSO_4$, and $ZnSO_4$ solutions and thin Cu, Ni, Co, and Zn films are deposited on the emitter surface [50,51]. Furthermore, a Cu/Ni bilayer structure was also fabricated by sequential processes using different solutions (Figs. 2.12(a)-2.12(c)) [51].

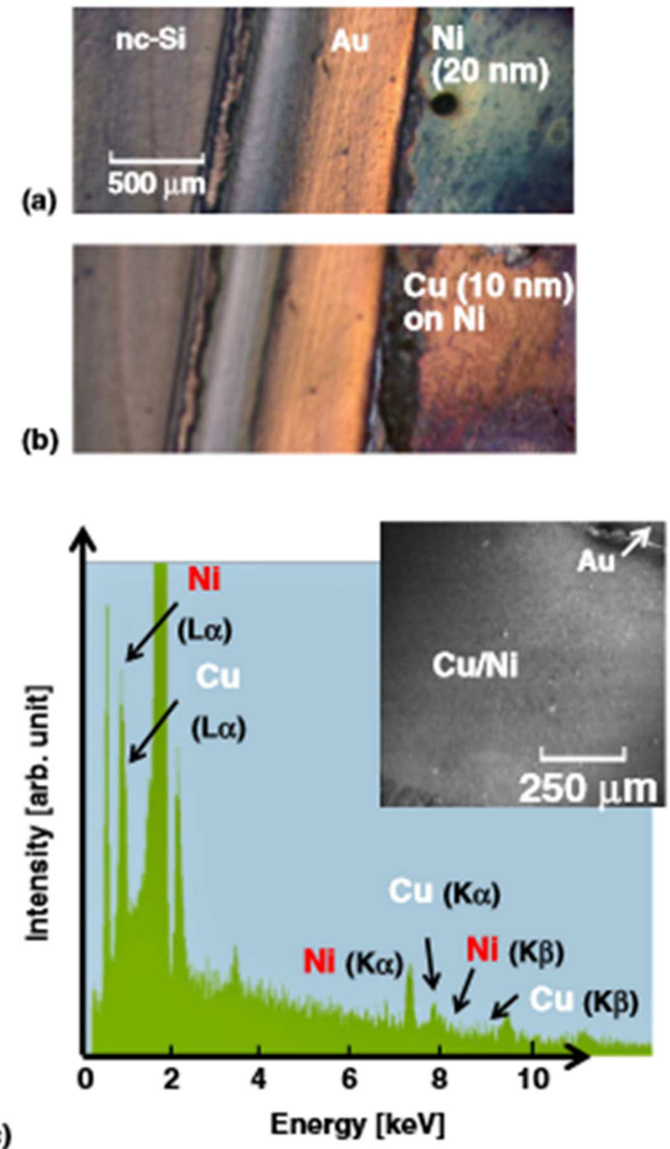

Figure 2.12 Optical micrographs of thin films of Ni (a) and Cu/Ni (b) deposited on nc-Si emitters. Characteristic X-ray signals of Cu and Ni was detected from the EDX spectrum for the Cu/Ni multilayer (c) [51].

Since the energy of ballistic hot electrons emitted from nc-Si diodes is as large as 5-7 eV, Si^{4+} and Ge^{4+} ions having a large reduction potential can be easily reduced. Deposition of Si and Ge thin films due to the reduction effect of ballistic electrons has been reported by Ohta and Koshida et al. [52,53]. In this study, electron diffraction measurement revealed that the deposited thin Si film was amorphous, as shown in Fig. 2.13 [52]. In addition, the Si wire array was formed by driving the nc-Si emitter patterned with resist mask in $SiCl_4$ solution (Figs. 2.14(a) and 2.14(b)) [52]. However, the deposited thin film was contaminated with carbon by the polytetrafluoroethylene (PTFE) film used to protect the nc-Si emitter [52]. Since thin films formed by this dipping method are deposited on the nc-Si emitter, it is difficult to apply it to the fabrication of devices such as thin film transistors (TFTs). The solutions to these problems are described in Chapters 3 and 4.

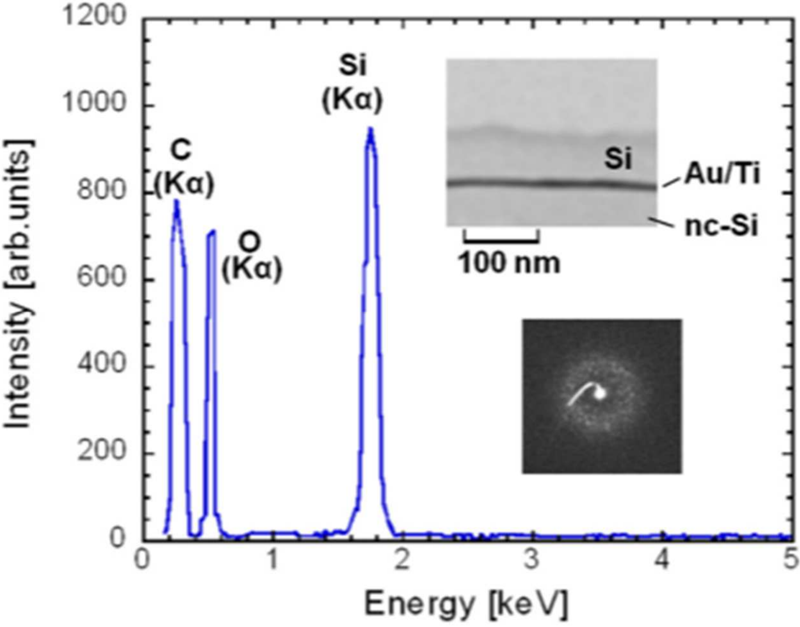

Figure 2.13 EDX spectrum of a thin Si film deposited on an nc-Si emitter. The insets show a cross sectional TEM image of the deposited film and the corresponding electron diffraction image (electron acceleration voltage: 200 kV). The diffraction analysis revealed that amorphous Si was deposited on the emitter [52].

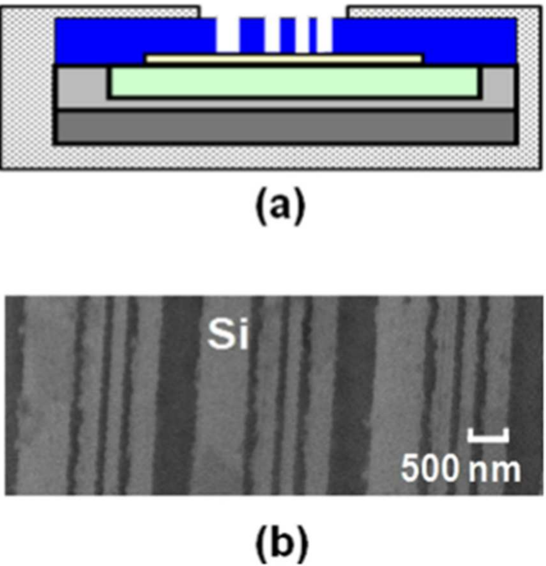

Figure 2.14 (a) Schematic device structure of nc-Si ballistic electron emitter patterned with electron beam resist. The actual device was fabricated such that the unit of four emission windows (500, 140, 100, and 180 nm in width) was arranged periodically. The SEM image confirmed that the arranged Si wires were deposited in parallel as designed (b) [52].

2.4 Summary

The characteristic features of nc-Si ballistic hot electron emitters and their applications has been made clear. The nc-Si diode emits ballistic electrons from the thin surface electrode by multiple tunneling under a high electric field in the nc-Si layer. The output electrons uniformly emitted from the surface electrode have high directionality. The electron energy of emitted electrons is much higher than that of thermally emitted electrons. From these features, the nc-Si emitter operates not only in vacuum but also in various media. In particular, in metal or semiconductor salt solutions, thin metallic and semiconducting films can be deposited due to the highly reducing activity of ballistic electrons. However, in the previous studies, there was a problem that the deposited thin films were contaminated by protecting films. Further, in the current thin film deposition method, since a thin film is deposited on the emitter surface, it is difficult to fabricate a device such as a TFT. The methods for solving these problems will be described in detail in the following chapters.

Chapter 3

Reductive thin-film growth under dripping mode

3.1 Introduction

As mentioned in previous chapter, the nc-Si ballistic emitter operates even in solutions as a supplier of highly reducing electrons into chemical species. In previous reductive deposition of thin film utilizing ballistic electrons, the nc-Si emitter was driven in a salt solution (dipping scheme). In this situation, the deposited film was contaminated with carbon by poly(tetrafluoroethylene) (PTFE) film used for device protection. A dripping scheme in which a very small amount of a solution is dripped onto the emitting surface is proposed here for avoiding such extrinsic contamination. This chapter reports deposition of thin Si and Ge films by dripping scheme and the detailed material characterizations of the deposited films. In addition, this deposition scheme was extended to thin SiGe film deposition.

3.2 Experimental

3.2.1 Emitter fabrication

The nc-Si emitters presented here were made from non-doped poly-Si on n^+-type Si wafers with a (100) crystal orientation. The wafers were back-deposited with a 300 nm thick Al film by vapor deposition before being vacuum annealed at 530 °C during 1 hour to form an ohmic contact. The wafer were sliced into small square pieces of 2×2 cm^2 followed by smoothing surface using chemical mechanical polishing (CMP). After that the wafers were cleaned in a pure acetone bath at room temperature under ultra-sonication during 15 min followed by a boiling pure ethanol 20 min as well.

The sample was anodized in an ethanoic HF solution (55% HF : ethanol = 1:1) under the illumination by a 500 W tungsten lamp. The anodization current was sequentially modulated in three cycles, at 2.5 mA/cm^2 for 1 s and 25 mA/cm^2 for 2 s to form a multilayer structure. High-quality

oxide films were then formed around Si nanodots by electrochemically oxidizing the prepared nc-Si layer in an ethylene glycol solution. Drying treatment was performed in supercritical CO_2 (pressure: 14 MPa) for removal of residual water molecules from the nc-Si layer. Finally, Au (10 nm)/Ti (1 nm) was sputtered on the nc-Si layer surface to form a thin surface electrode. On top of contacting layer, a small contacting pad of Al (300 nm) was deposited to provide higher mechanical support for the external contacting probe. The process flow is shown in Fig. 3.1.

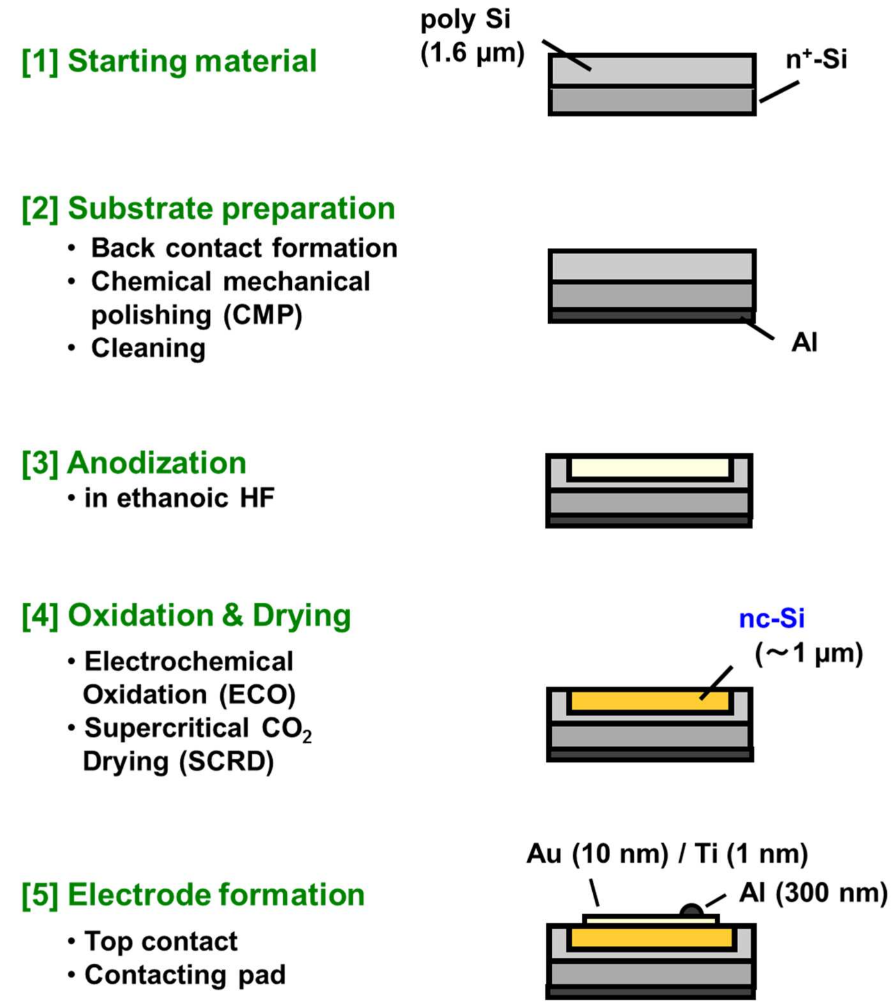

Figure 3.1 Process flow for fabrication of nc-Si emitter and its schematic structure.

3.2.2 Deposition scheme

The thin film deposition experiments were carried out with a simple configuration as shown in Fig. 3.2. A very small amount of a $SiCl_4$ or $GeCl_4$ solution dripping onto the limited nc-Si emitter surface area was controlled by a dispenser system (10-50 μl). The nc-Si electron emitter was then driven in the range of the applied voltage V_b from 10 to 15 V without using any counter electrode. A mixture solution of $SiCl_4$+$GeCl_4$ (1:1 in volume ratio) was used for deposition of a thin SiGe film. Since $SiCl_4$ and $GeCl_4$ are active in air, all the experiments were carried out in a N_2-gas-filled glove box. After the injection of ballistic electrons, residual solutions on the emitter surface were removed by elution or evaporation. The structure and chemical composition of the deposited thin films were characterized by scanning electron microscopy (SEM), energy dispersive X-ray (EDX) measurements, X-ray photoelectron spectroscopy (XPS), and secondary ions mass spectroscopy (SIMS).

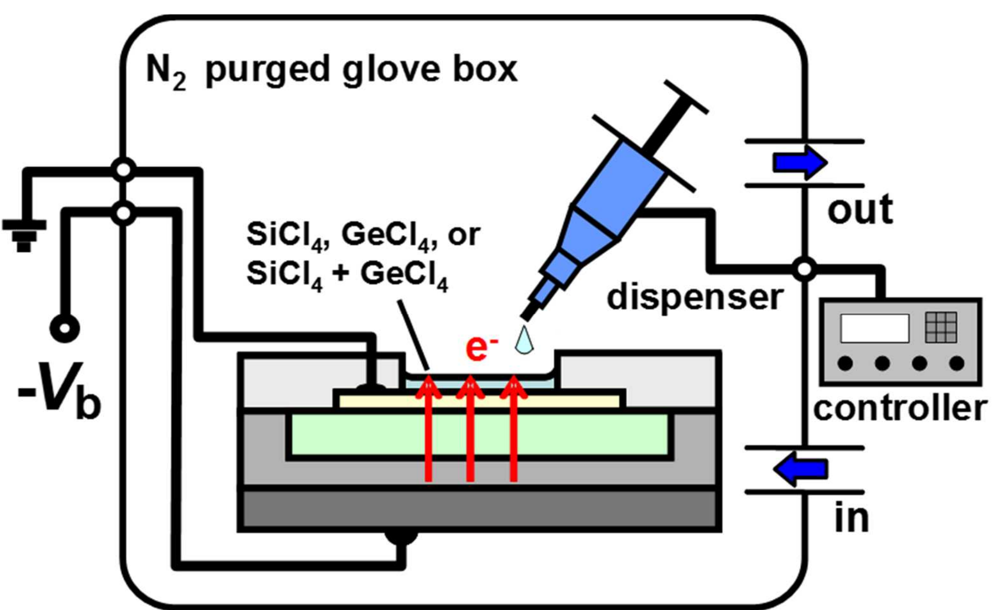

Figure 3.2 Schematic configuration for thin film deposition under dripping mode. The controlled dispenser system dripped a very small amount of solution onto the emitter surface regulated by a barrier mask. It is noted that no counter electrodes are used in this scheme.

3.3 Results and discussion

3.3.1 Thin Si and Ge films

As shown in Fig. 3.2, a $SiCl_4$ or $GeCl_4$ solution was dripped onto the nc-Si emitter surface, and then it was operated for 12 minutes. Thin film deposition was observed in the emitting area in each solution. Observed SEM images of thin Si and Ge films deposited near the boundary of the emission region are shown in Figs. 3.3(a) and 3.3(b). It appears that Si^{4+} and Ge^{4+} ions at the interface are preferentially reduced by injected energetic electrons, resulting in the deposition of a thin film as in the case of a thin metal film [49-51]. Unlike the usual electrode reaction, which proceeds following spontaneous migration of thermalized electrons, this reductive reaction unilaterally proceeds at the emitter surface due to the lack of the counter electrode. As a result, the Cl^- ion concentration in the solution relatively increases without gas evolution.

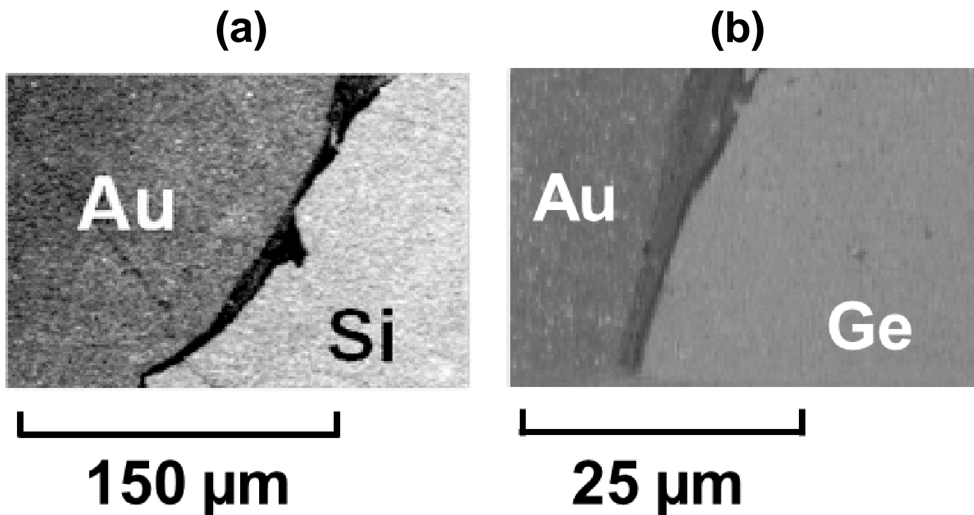

Figure 3.3 Observed SEM images of thin Si (a) and Ge (b) films deposited under dripping scheme (Samples 1 and 2). Ballistic electrons injection into the dripped $SiCl_4$ and $GeCl_4$ solutions leads to the thin film deposition at the electron emission area.

Figures 3.4(a) and 3.4(b) show the corresponding EDX spectra. It is noted that no contamination signals (such as Cl and C signals) are detected [74], in contrast to electroplating [26-28] and the previously reported dipping scheme [52,53]. This result suggests that unilateral reduction without byproducts proceeded at the electron emission surface. As suggested from the electron

diffraction image of thin Si film deposited by the dipping scheme [52], this deposited film is thought to be amorphous. The absence of a significant contamination of the deposited films is also supported by wide-scanned XPS spectra (0-1400 eV) measurements. In the XPS spectra of Figs. 3.5 (a) and 3.5 (b), it can be seen that the deposited films has no significant contamination signal except for O and C signals due to the exposure of samples to air before the XPS measurements. Figures 3.6(a) and 3.6(b) show XPS spectra for deposited Si and Ge films. The binding energy peak shift corresponding to the Si–O (SiO_2: 103.4eV) and Ge–O (GeO_2: 32.7eV) bonding [75] indicates the oxidation of deposited thin films. The lack of signals of Si–Si (Si 2p: 99.7eV) and Ge–Ge (Ge 3d: 29.3eV) [75] in the XPS spectrum will be discussed in Chapter 4. In this dripping mode, the C contamination previously observed in the dipping method is significantly suppressed in the dripping mode, and the sign of the Cl signal is below the detection limit of XPS. These results suggest the technical potential of this deposition mode.

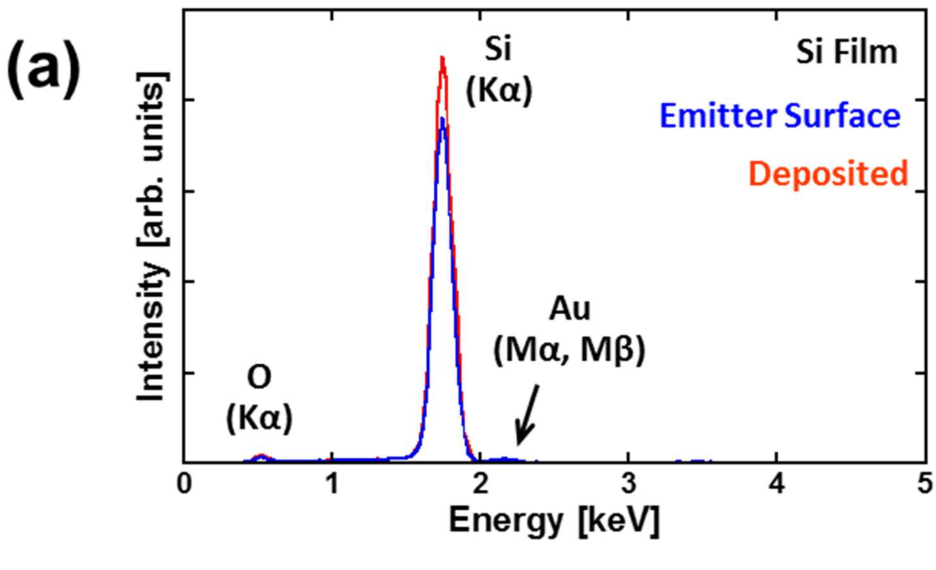

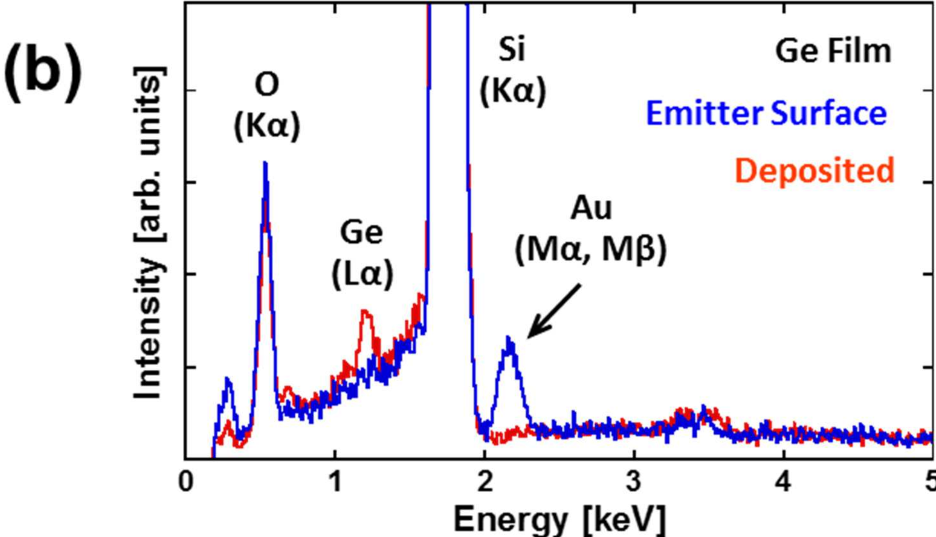

Figure 3.4 Measured EDX spectra of thin Si (a) and Ge (b) films deposited under dripping mode (Samples 1 and 2). For comparison, the spectrum of the original Au surface electrode is shown in each figure. It is important that no signs of C and Cl contaminations were detected in the deposited Si (a) and Ge (b) films.

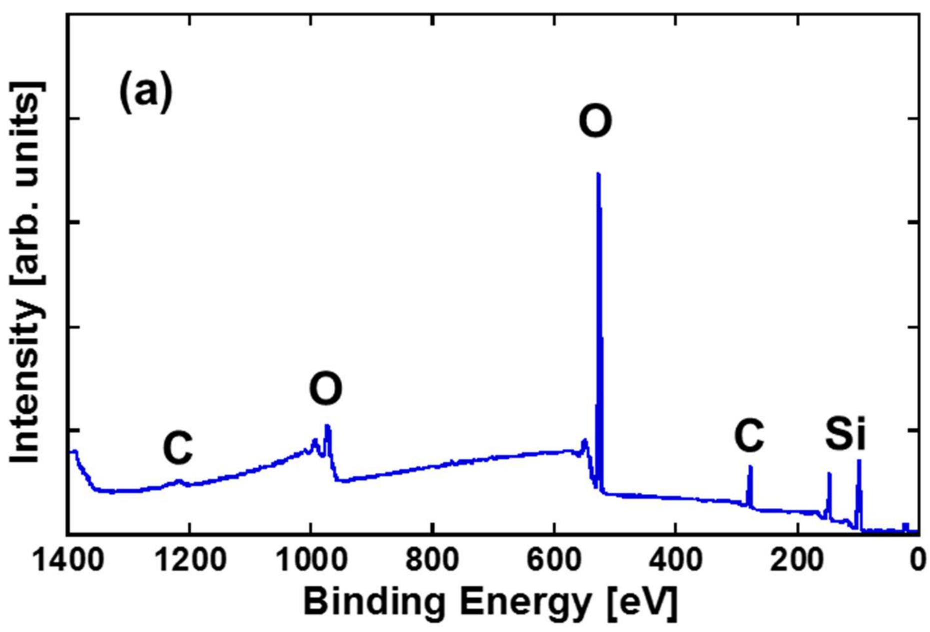

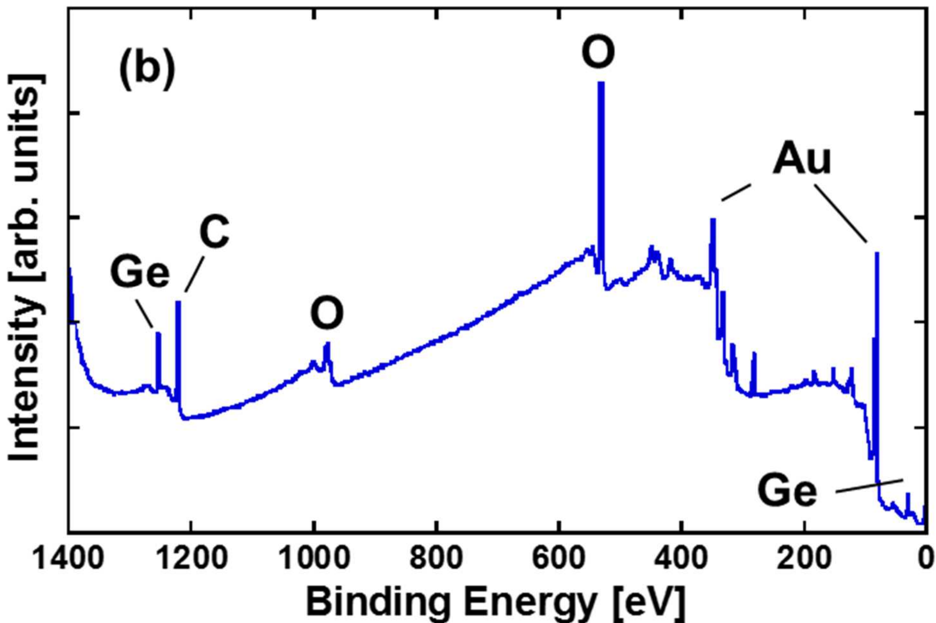

Figure 3.5 Measured wide-scanned XPS spectra of thin Si (a) and Ge (b) films deposited on the emitter surface (Samples 1 and 2).

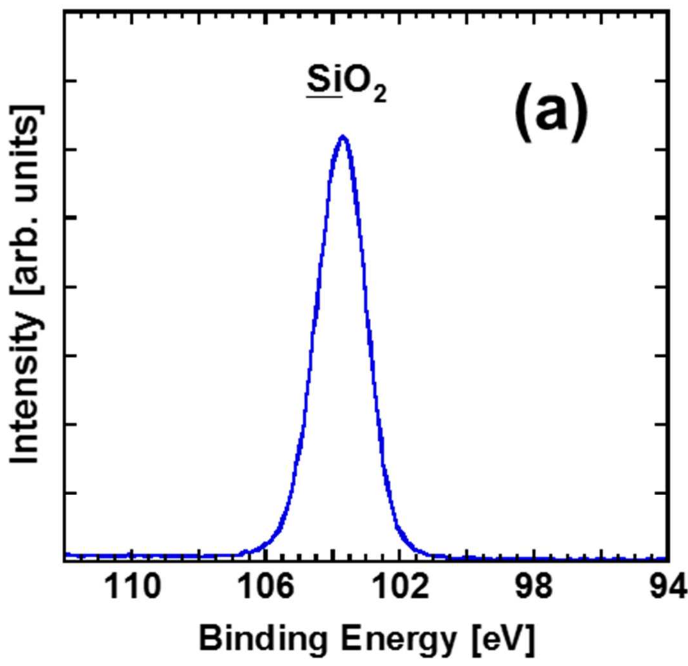

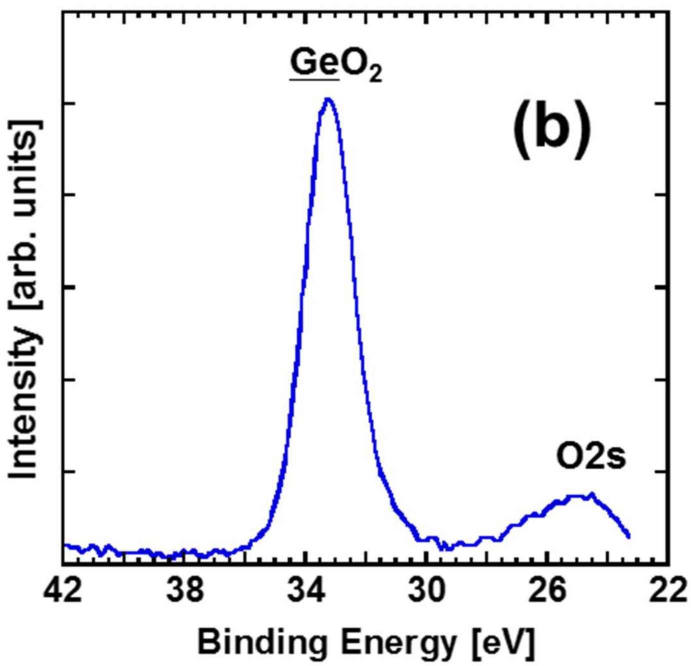

Figure 3.6 Measured XPS spectra of thin Si (a) and Ge (b) films deposited on the emitter surface (Samples 1 and 2).

Further evidence of this deposition mode is obtained from the SIMS measurements. The SIMS profiles of the deposited thin Si and Ge films are shown in Figs. 3.7(a) and 3.7(b). Both Si and Ge signal intensity profiles have obvious peaks near the surface region. The Au and Ti signals correspond to the materials of the thin surface electrode. The shaded area of the profiles (extremely outer surface) is excluded from consideration, as the SIMS profile is distorted by large fluctuations in the secondary ion yield. Because of the roughness of at least 10 nm on the original surface of the nc-Si emitter, the microscopic surface structures of the deposited Si and Ge films are not uniform. A diffusing behavior of the Au and Ti profiles in the deep region (>20 nm) is related to this surface roughness. In addition, the relatively high intensity of the Au signal is thought to be due to the local exposure of the surface electrode caused by a discontinuity of the deposited thin films.

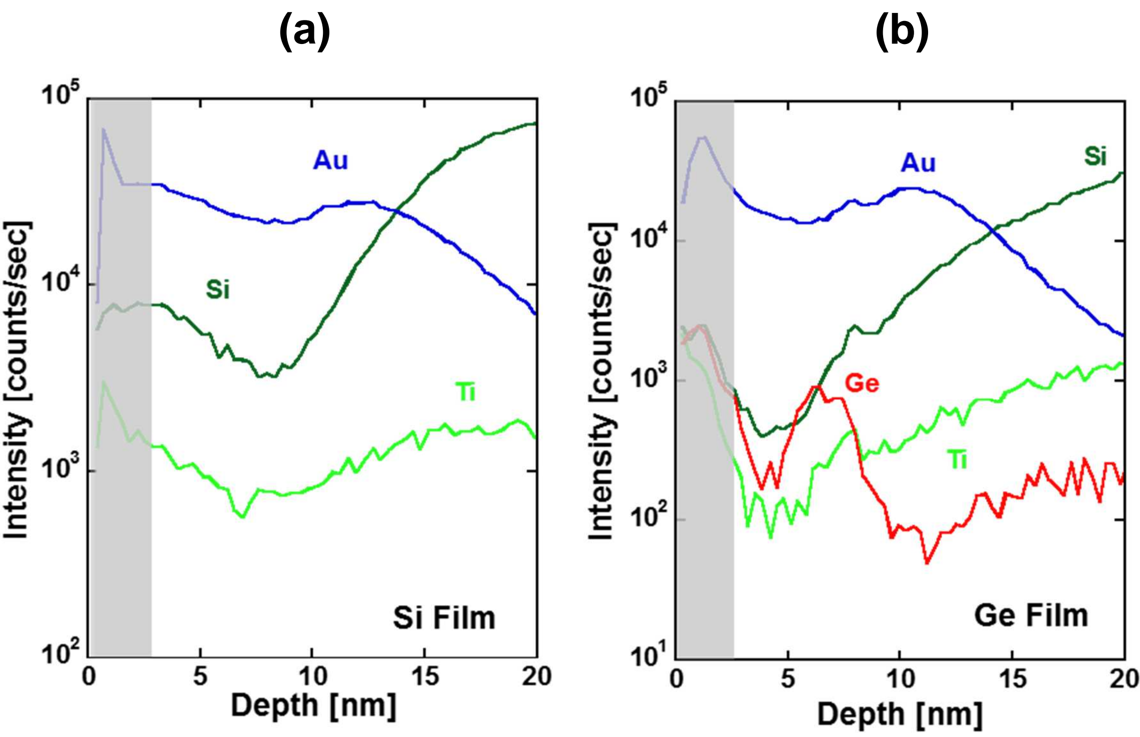

Figure 3.7 Measured SIMS profiles of deposited thin (a) Si and Ge (b) films (Samples 1 and 2). The extremely outer surfaces are excluded from consideration because of the fluctuation of the yield of secondary ions (gray area).

3.3.2 Thin SiGe films

Based on the above results, this dripping technique was applied to a thin SiGe film deposition using a mixture solution. After operation of the emitter in the condition of Fig. 3.2, thin film deposition was clearly seen in the electron emission area, as in the case of deposition of thin Si and Ge films. Figures 3.8(a)–3.8(c) show the surface SEM image and measured Si and Ge XPS spectra. The XPS measurements clearly detected the peaks corresponding to Si and Ge, as in the cases of thin Si and Ge films. It has been confirmed that a thin SiGe film is deposited in a self-regulated manner without using any complicated systems. The SIMS measurement as shown in Fig. 3.9 indicates that the peaks of both the Si and Ge signals clearly appear in the deposited region. The compositional ratio estimated from this SIMS intensity profile was $Si_{0.9}Ge_{0.1}$. The most important determining factor for deposition rate here is thought to be the chemical reduction kinetics. Another related factor is the energy difference between injected ballistic hot electrons and the reduction potentials of chemical species. There is a large difference in reduction potential between Si/Si^{4+} (–2.40 V vs SHE) [26] and Ge/Ge^{4+} (0.12 V vs SHE) [76]. In addition, the electrochemical window of $SiCl_4$ solution (3.76 V) is considerably larger than that of $GeCl_4$ solution (1.24 V). More detailed theoretical and experimental analyses of deposition of thin Si and Ge films need to be carried out on the basis of these differences. Other factors are the concentration of ions in solutions; the migration of reduced atoms, and the subsequent nuclei formation for the film growth. In the case of SiGe, mutual bonding formation of Si and Ge atoms is another issue. Although these factors are yet to be determined, the primary influential parameter for the control of the compositional ratio of SiGe is the initial mixture ratio of $SiCl_4$+$GeCl_4$ solution.

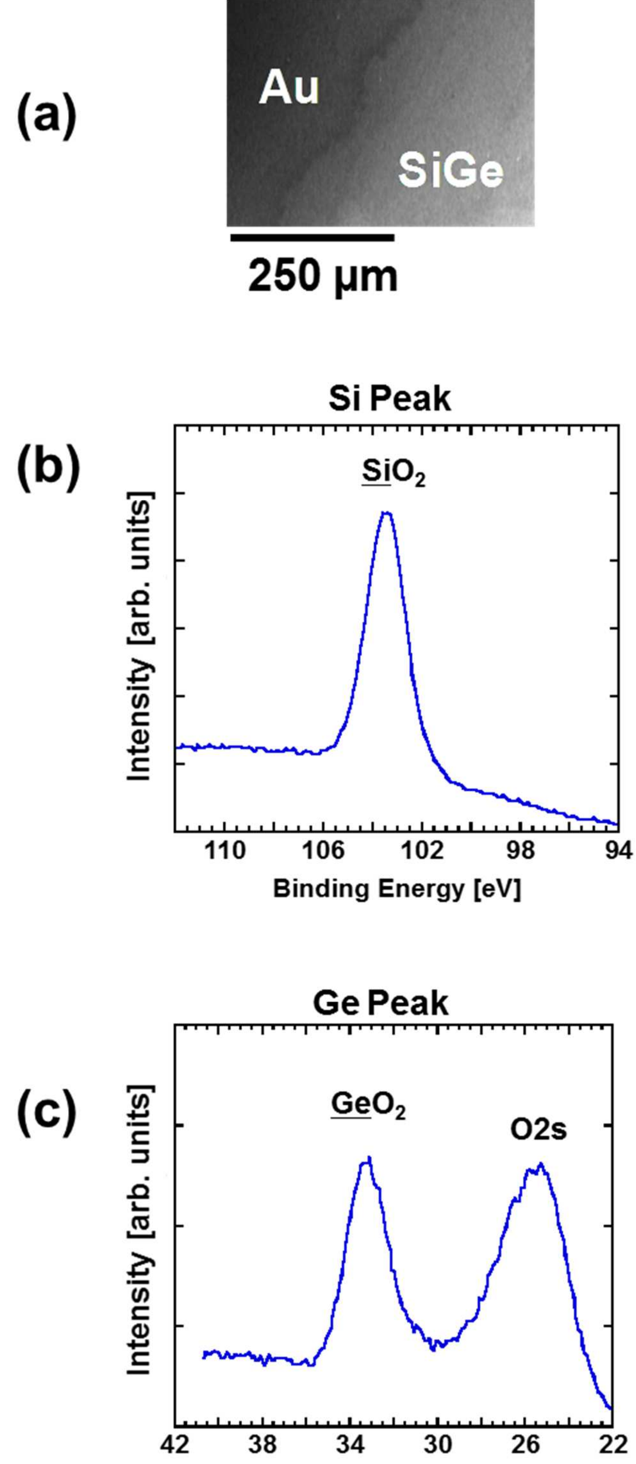

Figure 3.8 Observed SEM image (a) and the corresponding XPS spectra (b and c) of a deposited thin SiGe film (Sample 3).

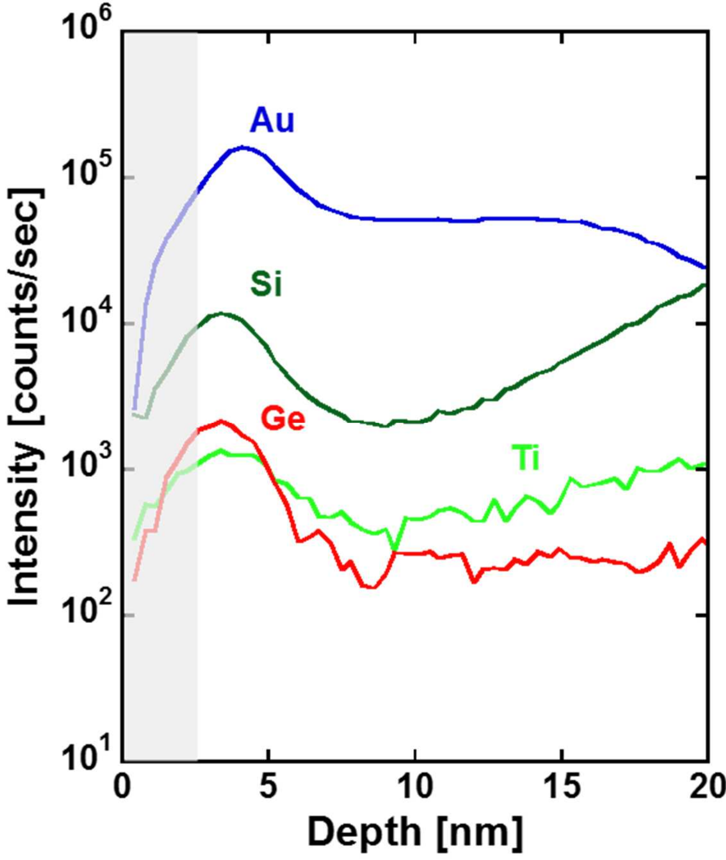

Figure 3.9 Measured SIMS profile of a thin SiGe film deposited on the emitting surface (Sample 3). The shaded area is excluded from consideration because of fluctuation of the yield of secondary ions.

3.3.3 Deposition rate

The deposition rate R of thin Si and Ge films under ballistic electron reduction can be explained by the previously reported model based on Faraday's law [52, 53]. According to this simplified model, the deposition rate R is given by

$$R = \frac{wJ_e}{nF\rho} \tag{3.1}$$

where w, J_e, ρ, n, and F are the atomic weight of Si or Ge, the injection current density, the density of Si or Ge, valence of the Si^{4+} or Ge^{4+} ion, and the Faraday constant, respectively. This equation suggests that it is possible to estimate the thickness of the deposited thin film from J_e and the operation time T_o. These experimental conditions and the corresponding estimated film thickness t_e are summarized in Table 3.1. In the case of $Si_{0.9}Ge_{0.1}$, the compositional ratio was taken into account for

the estimation. For comparison, the film thicknesses determined from the width of the SIMS profile, denoted by t_S, are also shown in this table. In each case, the t_S values are larger than the t_e values. This is attributed to a limited depth resolution in the SIMS profile owing to the surface roughness. It is possible to fabricate multilayered Si/Ge structures by a sequential drive of the emitter for dripped $SiCl_4$ and $GeCl_4$ solutions. This reductive deposition scheme is potentially useful for low-temperature, damage-free, and clean deposition of ultra-thin semiconductors, and possibly multilayered film structures the fabrication of photonic and electronic devices. Indeed, an efficient visible photoluminescence has been confirmed from a deposited thin Si film [52].

Table 3.1. Experimental parameters of the thin film deposition (V_b: applied bias voltage (ref. Fig. 3.2), J_e: injected current density, T_o: operation time) and the film thickness t_e estimated from the theoretical deposition rate. The values of thickness t_S, determined from measured SIMS profiles, are also shown for comparison.

Sample	Solution	V_b [V]	J_e [μA/cm^2]	T_o [min]	t_e [nm]	t_S [nm]
1	$SiCl_4$	11	8	12	1.7	8
2	$GeCl_4$	12	8	12	2.0	8
3	$SiCl_4$ + $GeCl_4$	12	5	12	1.1	5

Compared to the previously reported dipping scheme [49-53], the proposed dripping scheme significantly suppresses extrinsic carbon contamination. The amount of solution for thin film deposition can be minimized because of driving the nc-Si emitter without using any counter electrode. However, since electron emission from the nc-Si emitter tends to decrease as the thickness of the deposited thin film increases, there should be a self-limiting mechanism in this deposition process. The improved method is presented in the next chapter.

3.3.4 Structural and electrical characterization

The structural and electrical characteristics of the thin Cu film deposited by the dripping mode were evaluated. When a copper chloride solution was dripped on the emitter surface and then the emitter was driven, a thin metallic film was deposited on the emitter surface. SEM image and EDX spectrum of the deposited thin Cu film shown in Fig. 3.10(a) suggest that thin Cu film was deposited by ballistic electron injection into the copper salt solution. From AFM measurement (Fig. 3.10(b)), the average film thickness of deposited thin Cu film was estimated to be about 100 nm. According to the results of 4-probe and AFM measurements, the resistivity of an as-deposited thin Cu film was 561 μΩ·cm. This value is about 300 times larger than the Cu bulk resistivity (1.68 μΩ·cm). This can be attributed to the fact that the deposited film has a grain structure as observed in SEM image and AFM profile. The structural and electrical properties of the thin film deposited by this method should be improved by annealing treatment.

Figure 3.11 shows an In-plain XRD spectrum of thin Cu film deposited by ballistic electron injection reported by Ohta et al. [51]. In this spectrum, cubic lattice structure peaks were detected such as Cu(111), Cu(200), and Cu(220), suggesting that a polycrystalline Cu film has been deposited under ballistic electron reduction. The present deposited thin Cu film is thought to be polycrystalline as well.

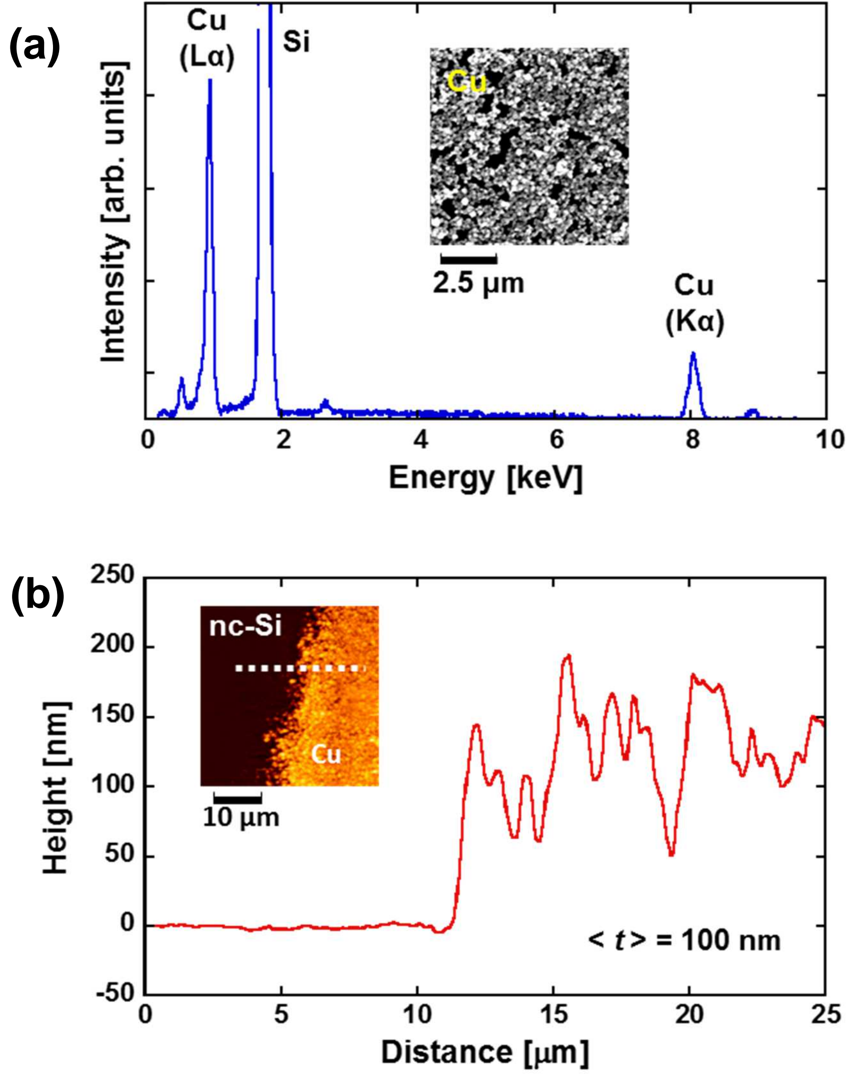

Figure 3.10 (a) EDX spectrum and corresponding SEM image of thin Cu film deposited by dripping mode. (b) AFM image and thickness profile of deposited thin Cu thin. The electrical resistivity of the deposited thin Cu film was estimated to be 561 μΩ·cm by 4-probe measurements.

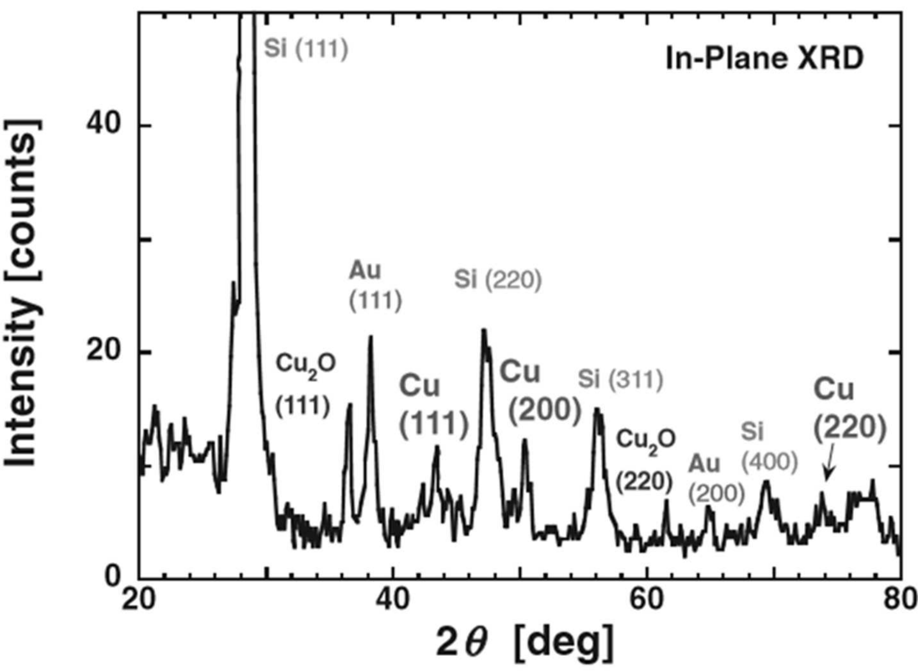

Figure 3.11 In-plain XRD spectrum of thin Cu film deposited by injection of ballistic electrons into copper salt solution. The spectrum indicates that polycrystalline Cu deposited on the emitter surface [51].

3.4 Summary

When ballistic hot electrons are injected into the dripped solution, it is shown that an amorphous thin group-IV film is uniformly deposited on the nc-Si emitter. Besides elemental Si and Ge, thin films of SiGe can also be deposited under proposed dripping scheme. This mode is triggered by preferential reduction of target ions without by-products. The emitted electron energy matches well with the requirements for reduction of Si^{4+} and Ge^{4+} ions. In contrast to the conventional dry process based on the decomposition of active gases, the ballistic electro-reduction proceeds at room temperature. However, this deposition scheme tends to saturate the thin film growth at a certain thickness due to the self-limiting effect on electron injection. It has been shown that the electrical resistivity of the thin Cu film deposited by the dripping mode is 561 Ω·cm, and that the structure is of polycrystalline feature.

Chapter 4

Ballistic-electron printing of thin films

4.1 Introduction

Previous chapter mentioned that the dripping scheme tends to saturate at a certain thickness because of a self-limiting mechanism. In addition, since the thin film is deposited on the emitter surface, handling of the deposited film is not easy for practical use. Therefore, a printing scheme has been proposed here for thin film deposition onto a counter substrate. The nc-Si emitter is located separately from the target substrate coated with the metal or semiconductor salt solution, and then ballistic electrons are irradiated onto the substrate. This deposition scheme can be expected to solve the above-mentioned problems. The experimental results are shown here for thin Cu, Si, and Ge films.

4.2 Experimental

The nc-Si emitters were prepared as described in Chapter 3. Figure 4.1 shows the experimental setup of printing scheme. All the experiments were carried out in a N_2-gas-filled glove box at room temperature. At first, a Cu, Si, or Ge salt solution was coated on a single-crystalline Si (c-Si) wafer substrate, a thermally oxidized (0.01 ~ 1 μm thick) c-Si, or a Cu substrate. Since $SiCl_4$ and $GeCl_4$ are very active with water molecules in ambient, propylene carbonate was used as a water-proof organic solvent. This substrate was located in front of the nc-Si emitter. A gap between them was controlled by a piezoelectric actuator in the range 500 nm ~ 5 mm at 10^1 ~ 10^5 Pa, taking the ambient pressure dependence of ballistic hot electrons' mean free path and vaper pressure of the coated solution into account. The salt solutions and target substrates are summarized in Table 4.1. For thin film deposition, the nc-Si electron emitter was driven in an intermittent pulse at V_b = 10 -16 V with a duty ratio of 20%. The voltage V_a between the emitter and the substrate was 0 - 20 V. The current density J_e was monitored during the emitter operation. After the processing, residual solutions were removed by

elution or evaporation. The deposited films were characterized by scanning electron microscope (SEM), energy dispersive X-ray (EDX), atomic force microscope (AFM), spectroscopic reflectometer, X-ray photoelectron spectroscopy (XPS), and Raman scattering measurements.

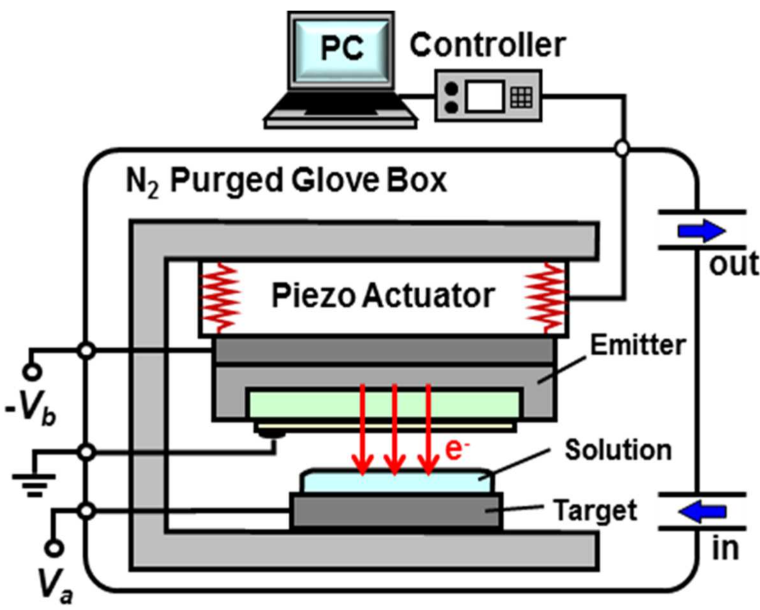

Figure 4.1 Schematic experimental configuration of thin-film deposition under an electron incidence scheme. A solution-coated target substrate is remote from an nc-Si emitter. A piezoelectric actuator allows us to control a gap between the nc-Si emitter and the target substrate in a N_2 purged glove box.

Table 4.1 Experimental parameters of the thin-film deposition [c, concentration of solution; V_b, applied bias voltage (refer to Fig. 4.1); V_a, voltage between nc-Si emitter and target substrate; J_e, electron emission current density; T_o, operation time]. EG, PC, and EMI-DCA represent ethylene glycol, propylene carbonate, 1-ethyl-3-methylimidazolium dicyanamide (ionic liquid), respectively.

Sample	Electrolyte	Solvent	c (M)	Target substrate	Pressure (Pa)	Gap	V_b (V)	V_a (V)	J_e (μA/cm²)	T_o (min)
1	$CuCl_2$	H_2O + EG	0.075	Si	10^4	0.1 mm	16	10	0.7	120
2	$CuSO_4$	H_2O	0.1	Si	ambient	0.5 μm	16	0	8.0	20
3	$CuCl_2$	H_2O + EG	0.075	SiO_2/Si	10^4	0.3 mm	15	5	0.1	60
4	CuCl	EMI-DCA	1.0	Si	$<10^2$	1 mm	16	5	5.2	40
5	$SiCl_4$	PC	0.5	Cu	10^3	5 mm	16	20	9.3	10
6	$GeCl_4$	PC	0.5	Cu	10^3	5 mm	16	20	6.2	10

4.3 Results and Discussion

4.3.1 Thin Cu films

After irradiating ballistic electrons on the target substrate coated with $CuCl_2$-solution under the above procedure, a color change appeared on the target substrate surface probably due to thin metallic film growth. The SEM images of the original c-Si and deposited thin film surfaces are shown in the insets of Fig. 4.2. These images indicate that the thin metallic films were deposited on the impinging area under the printing mode. As shown in Fig. 4.2, the EDX spectra and the corresponding SEM images clarify the composition of the deposited film. The characteristic X-ray signals of Cu corresponding to Lα, Kα, and Kβ [74] were clearly detected without contaminations such as carbon and chlorine. This result clearly suggests that the as-deposited thin film consists of pure Cu. As shown in Fig. 4.3, similar thin film deposition was obtained under the printing mode using $CuSO_4$ aqueous solution [65]. The implication is that preferential reduction of Cu^{2+} ions on solution surface due to impinging energetic electrons led to nucleation for the growth of Cu thin films. Although their electrical properties have not yet been evaluated, the adhesion strength between the deposited Cu films and the substrates is comparable with that formed by conventional vacuum deposition or sputtering.

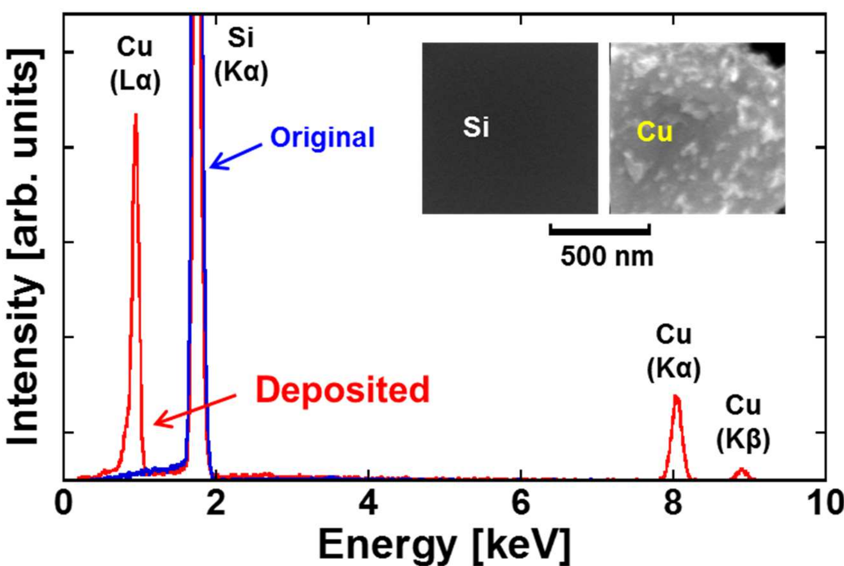

Figure 4.2 Measured EDX spectra of the original and deposited substrate surfaces (Sample 1). The inset shows the SEM images corresponding to each EDX spectrum.

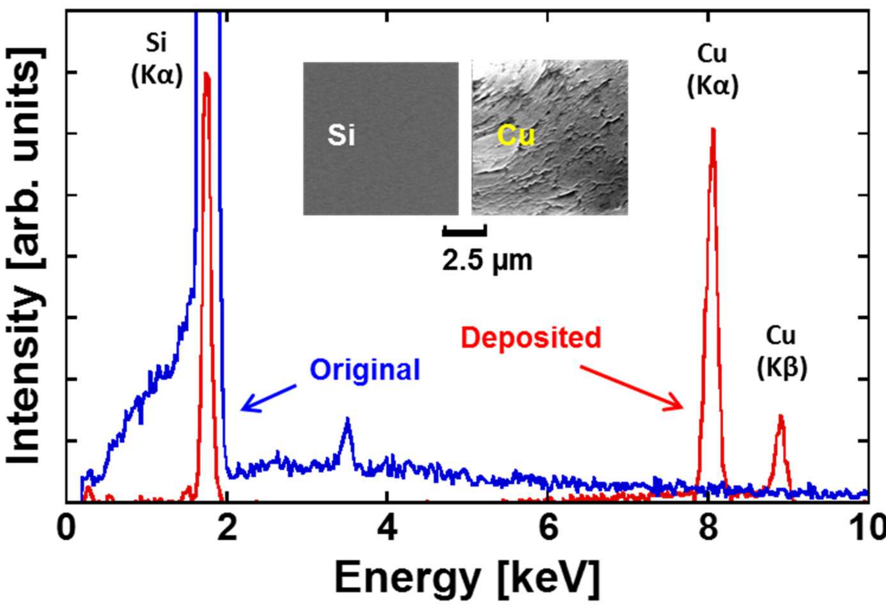

Figure 4.3 Measured EDX spectra of the original and deposited substrate surfaces (Sample 2). The respective SEM images are also shown in the inset [65].

Related evidence of this printing deposition mode has also been obtained from thickness measurements. The AFM image of the deposited thin Cu film and the corresponding thickness profile are shown in Figs. 4.4(a) and 4.4(b), respectively. From the AFM profile in Fig. 4.4(b) the average

film thickness was estimated to be 6.6 nm. Figure 4.5 shows the measured and simulated optical reflection spectra of the Cu film deposited on the Si substrate. The Cu film thickness suggested from the fitting of the simulation to the experimental curve is 5.7 nm that is nearly equal to the AFM result. As described in Chapter 3, it is expected that in the printing mode under the reductive reaction of X^{n+} ions, that is $X^{n+} + ne^{-} \rightarrow X$, the film deposition rate R is proportional to the electron emission current density J_e [52,53]. At J_e = 10 ~ 100 μA/cm^2, for instance, the expected R value of Cu is 0.22 ~ 2.2 nm/min. The value expected from the deposition rate and the emitter operation time is almost equal to the observed film thickness. A detailed discussion on deposition rate in the printing mode is given in Chapter 5.

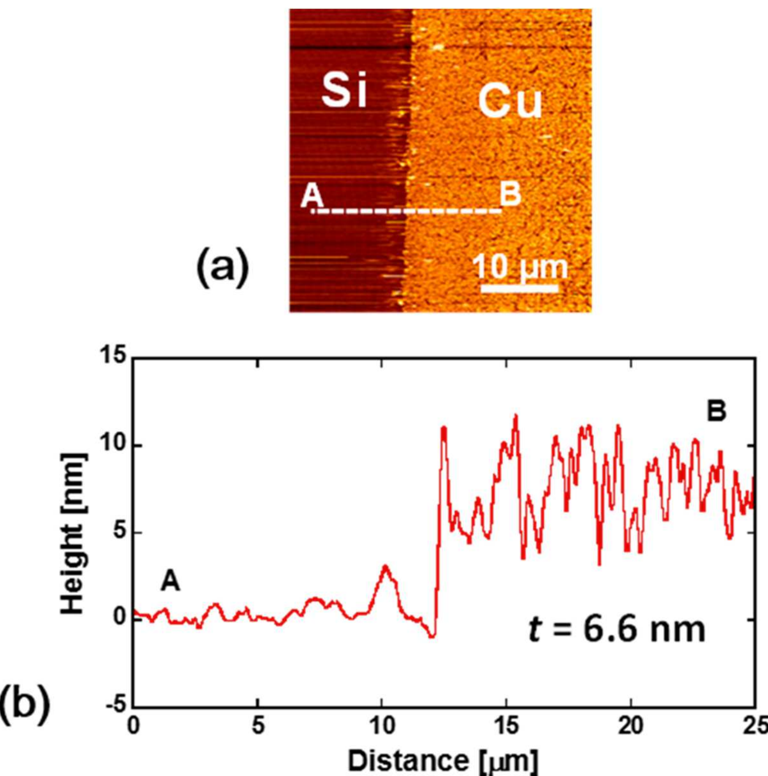

Figure 4.4 An AFM image obtained from the boundary between the deposited thin Cu film and the original the c-Si substrate (a), and corresponding thickness profile (b) (Sample 1). The film thickness can be estimated about 6.6 nm.

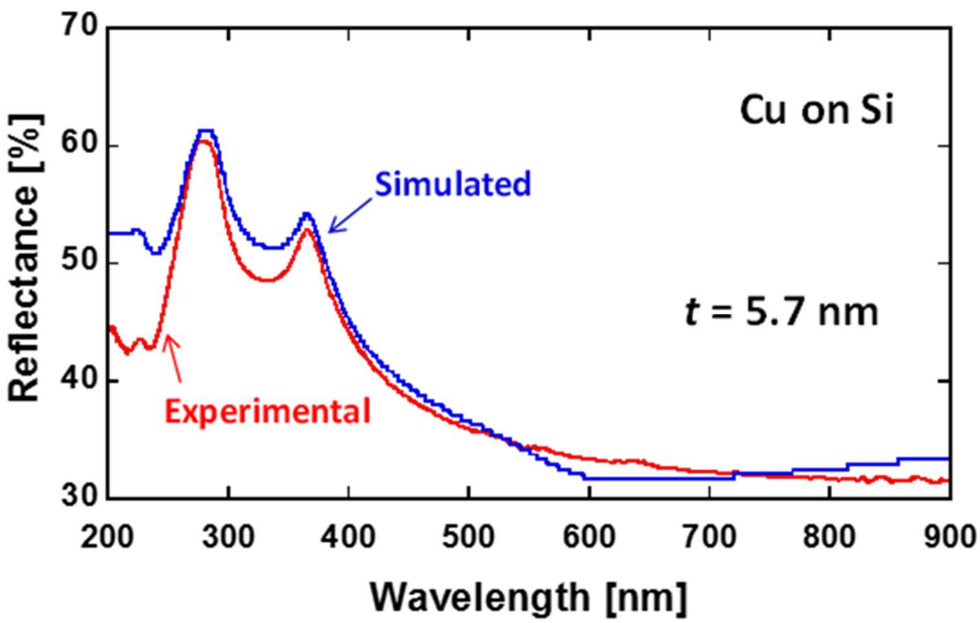

Figure 4.5 Reflection spectrum obtained from the deposited film (sample 1). Simulated spectrum assuming Cu deposited on Si is also shown here. By fitting the measured and simulated spectra, the thickness of the deposited thin Cu film is estimated to be 5.7 nm.

It was confirmed that no electrode reaction on the substrate contribute to present scheme under ballistic printing using a thermally oxidized c-Si wafer as a substrate. When printing deposition was performed on the same experimental conditions of Fig. 4.1, a pure thin Cu film was also deposited on SiO_2/Si as in the case of c-Si substrate case (Fig. 4.6). Apparently unilateral reduction under electron incidence is different from carrier exchange at the conventional electrode reaction. It is important from a technological viewpoint that the printing deposition scheme is potentially available for insulating substrates such as glass and polymers. The use of low vapor pressure ionic liquid as a solvent can further enhance its usefulness. For example, the printing experiments can be performed even at a vacuum pressure ($<10^2$ Pa) and a large emitter-target gap (>1 mm) by using a c-Si wafer coated with a CuCl-dissolved ionic liquid [77-79]. The deposition of thin Cu films has been successfully observed as well after electron emitter operation, as shown in Fig. 4.7. As the unilateral reduction of Cu^{2+} in solution proceeds, the relative concentration of negative ions (Cl^- in this case) should be increased without gas evolutions. As previously reported, the nc-Si emitter operation in pure water and metal salt solutions without using any counter electrode led to significant increase of

the pH value with increasing operation time of the emitter [73]. A possible explanation is that spontaneous neutralization by metastable positive ions in experimental environment might promote continuous thin film deposition by preventing infinite negative charging.

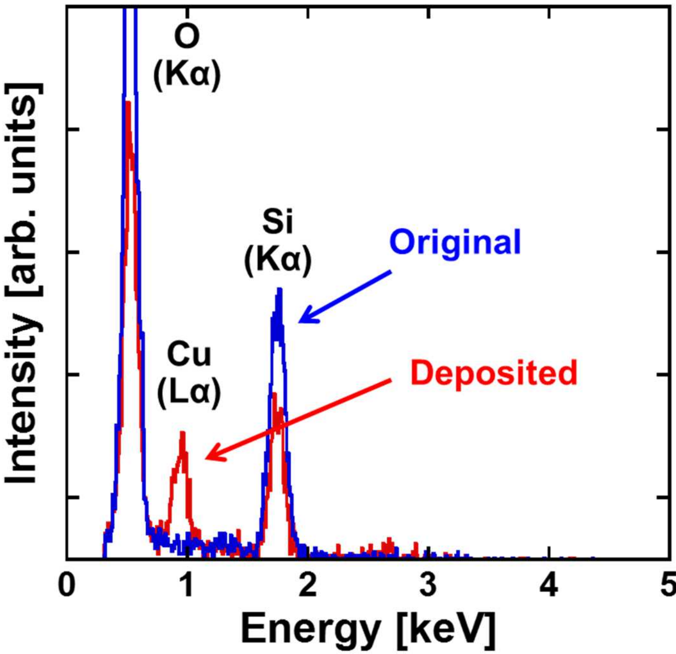

Figure 4.6 Measured EDX spectra of the original substrate and deposited film surfaces (Sample 3). A thermally oxidized c-Si wafer (SiO_2/Si) was used as the substrate in this case.

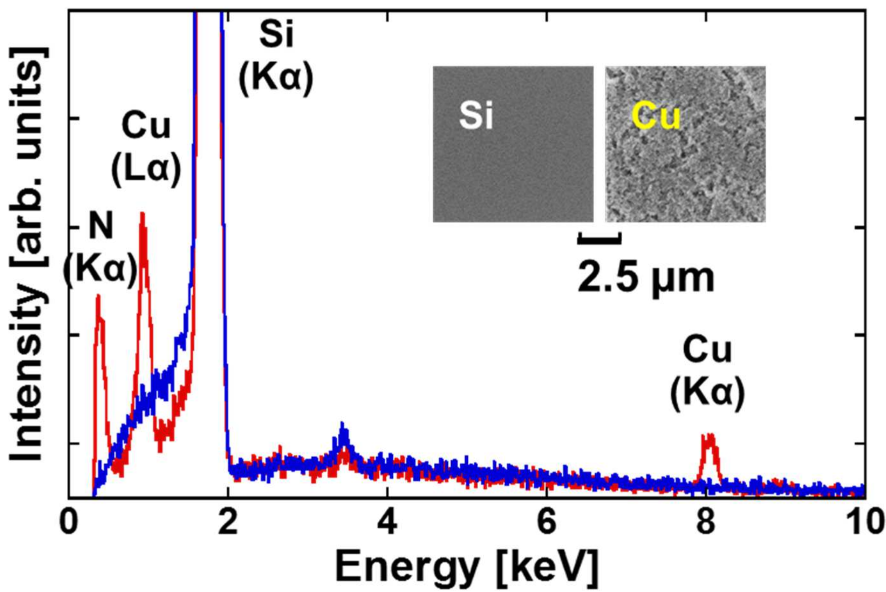

Figure 4.7 Measured EDX spectra of the original substrate and deposited film surfaces (Sample 4). A thermally oxidized c-Si wafer (SiO_2/Si) was used as the substrate in this case. 1.0 M CuCl (solvent: 1-ethyl-3-methylimidazolium dicyanamide) was used for the solution. By using ionic liquid as a solvent, irradiation of ballistic electrons becomes possible even in high vacuum condition. Contamination of nitrogen can be removed by additional cleaning method.

4.3.2 Thin Si and Ge films

During the above-mentioned incidence procedure, a color change appeared in the target substrate surface, due to the growth of a thin film. The insets in Figs. 4.8(a) and 4.8(b) show the SEM images of the boundary between deposited thin films and the original Cu area. Thin Si and Ge films are deposited on the impinging area after removing the residual solution, as in the case of the Cu deposition. The EDX spectra obtained from deposited thin films are shown in Figs. 4.8(a) and 4.8(b). The characteristic X-ray signals of Si and Ge [74] were clearly detected with no contaminations of chlorine. The peaks of the carbon are likely due to the solution residue. These components might be removed by complete dissolution treatments. Actually, in case of the Cu deposition, no signals of carbon contamination were detected in EDX spectra after a sufficient dissolving process.

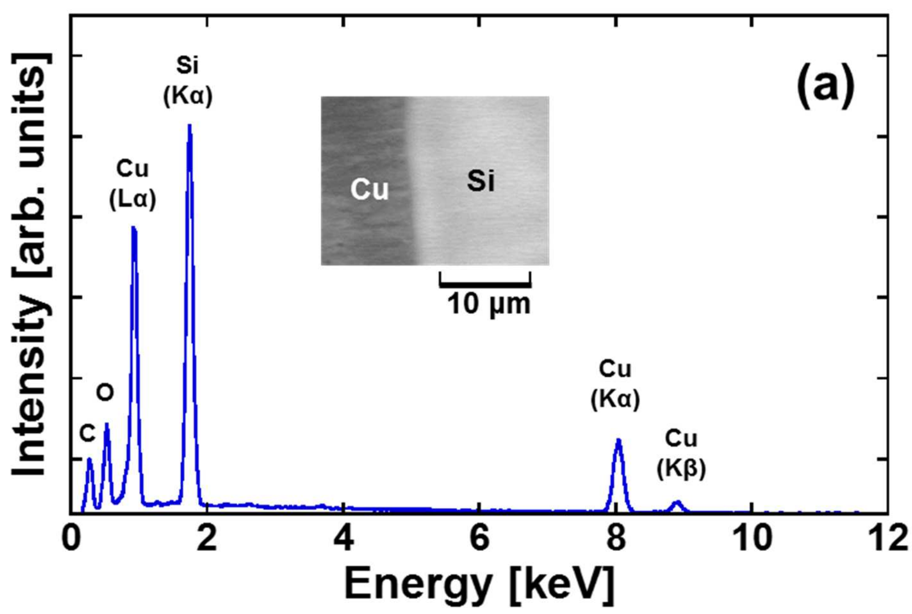

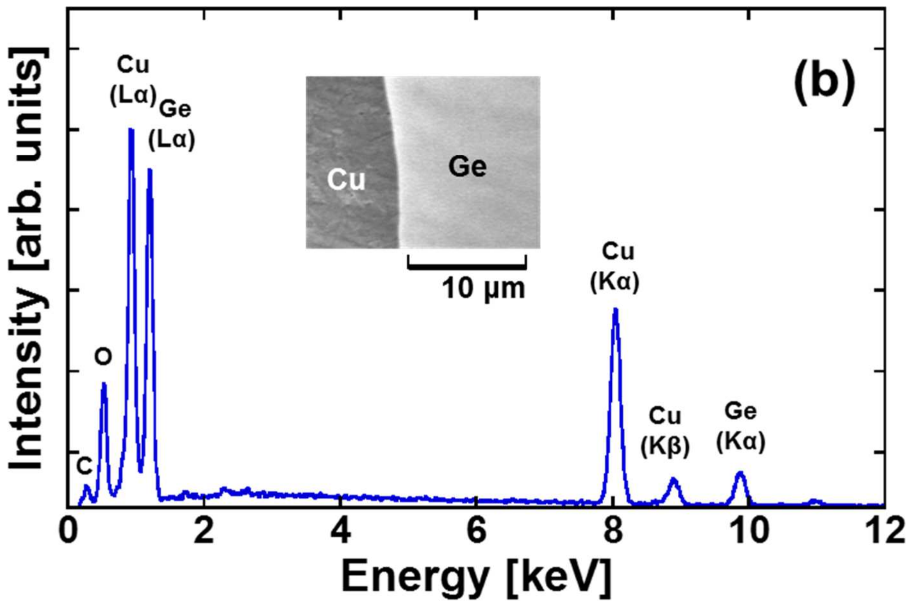

Figure 4.8 Measured EDX spectra of Si (a) and Ge (b) films deposited under an incidence mode (Samples 5 and 6). The observed SEM images near the boundary between the original Cu substrate and deposited thin films are shown in the insets.

The results of XPS measurements of deposited films are shown in Figs. 4.9(a) and 4.9(b). In both cases, thin films are oxidized, though the thin Ge film is not fully oxidized [75]. It is difficult from these results to suppose that thin films are deposited as continuous layers. Possibly the formation of very small nanoclusters occurs at the initial stage of electron incidence and subsequently fast oxidation proceeds in solutions associated with deposition, rather than natural oxidation (Fig. 4.10), though the details of competitive process of nucleation and oxidation should be clarified. As in the case of the previous dripping mode, no other signals like chlorine were observed in XPS spectra of deposited thin films measurements, as shown in Fig. 4.11(a) and 4.11(b).

On the other hand, secondary ions of Cl were detected in the SIMS analysis of the deposited thin Si film as shown in Fig. 4.12. Though the quantitative contamination level within the film is yet to be determined, the SIMS profile suggests that the Cl signal intensity tends to increase towards the interface between the deposited thin film and the Cu substrate. Taking into account that the secondary ion yield of Cl for Cs^+ is about one order and two orders of magnitude higher than that of Si and Cu [80], respectively, the observed Cl profile is related not to the intrinsic contamination, but to the extrinsic one like the residual solution. This assumption should be verified by more complete post-deposition cleaning to remove the residual solution. Judging from XPS measurements, the contamination level in the present deposited films is thought to be less than 300 ppm. It appears that impinging energetic electrons preferentially reduce Si^{4+} and Ge^{4+} ions at the solution surface, which is followed by the nucleation and oxidation. Similar to the printing deposition of thin Cu films, the resultant change in the solution is only a relative increase in the Cl^- ion concentration without gas evolutions.

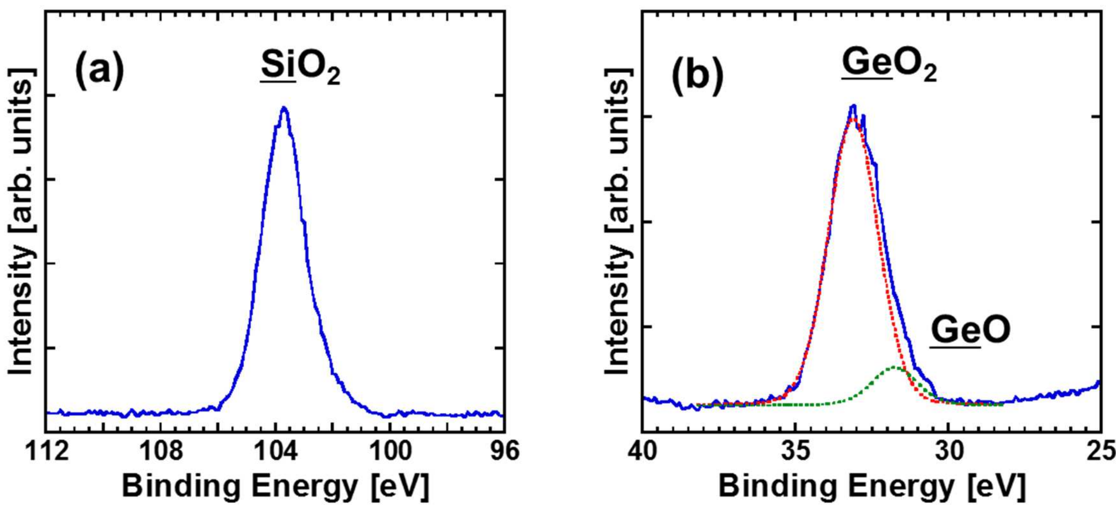

Figure 4.9 Measured XPS spectra of deposited thin Si (a) and Ge (b) films (Samples 5 and 6).

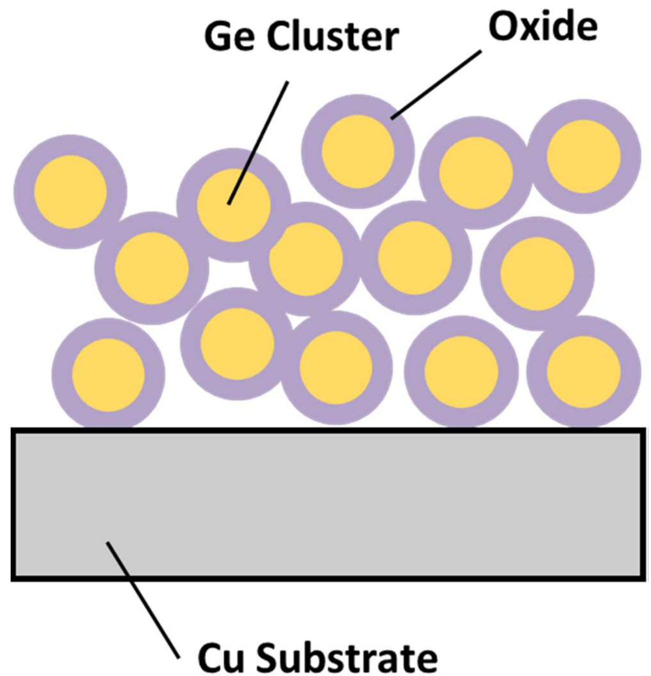

Figure 4.10 Schematic of the expected structure of the thin Ge film deposited by the printing mode. The thin Ge film consists of nanoclusters covered with thin oxide films.

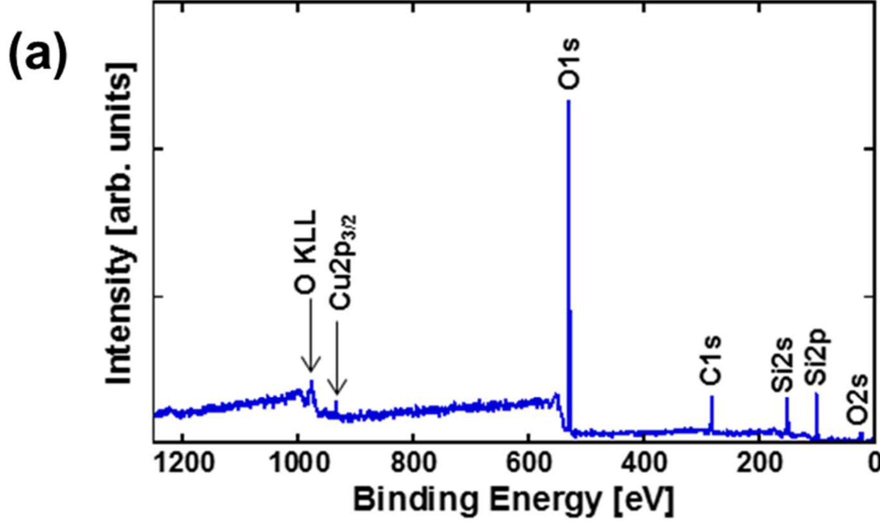

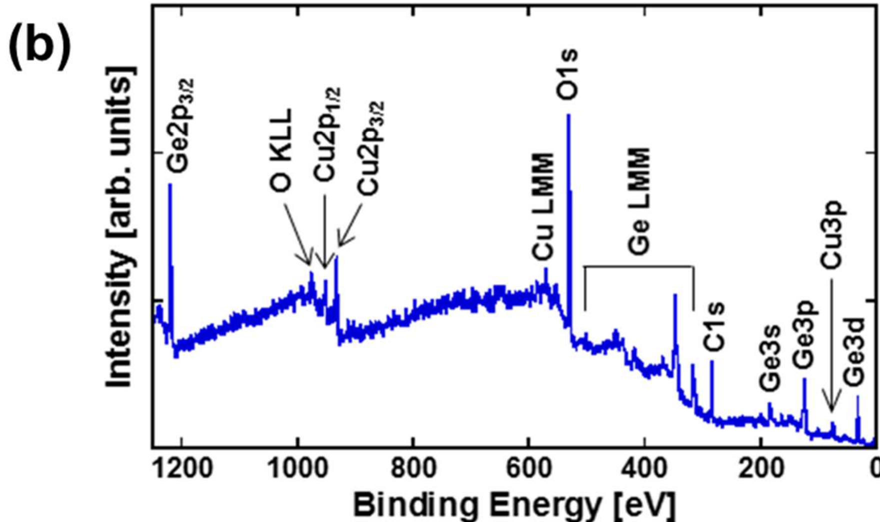

Figure 4.11 Wide-scanned XPS spectra of deposited thin Si (a) and Ge (b) films (Samples 5 and 6). Cl contamination is not detected in both deposited thin Si and Ge films.

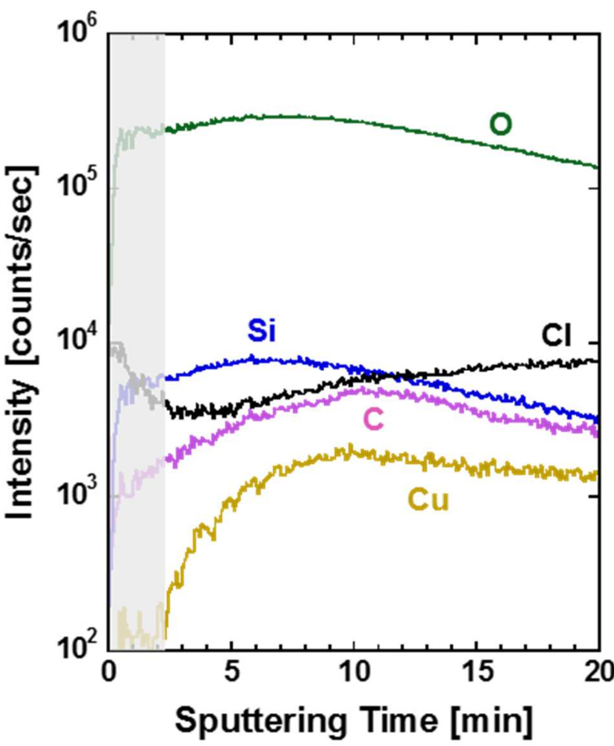

Figure 4.12 Measured SIMS profiles of thin Si film deposited on Cu substrate. The extremely outer surface surrounded by the shaded area is excluded from consideration because of fluctuation of the yield of secondary ions.

The model nanoclusters formation has been supported by Raman spectrum of thin Ge film as shown in Fig. 4.13. Owing to a sufficiently large absorption coefficient of incident laser (5.4×10^5 cm^{-1} at 532 nm in this case [81]), Raman shift features related to ordered Ge-Ge bonding at 300 nm [82] and amorphous phase at 280 nm [83-85] are detected. In thin Si films, significant Raman signals were not observed due to a relatively small absorption (1.1×10^4 cm^{-1} at 532 nm [81]).

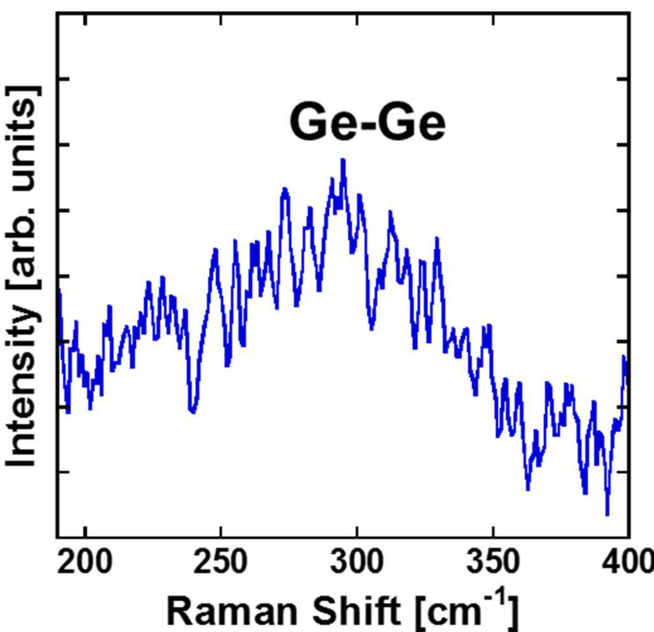

Figure 4.13 Measured Raman spectrum of a thin Ge film deposited on Cu substrate (Sample 6). A 532 nm laser was used.

4.3.3 Comparison with dripping mode

From scientific and technological viewpoints, there are distinct differences between the previous dripping and the present case.

i) It has been made clear by the present electron incidence mode that thin solid films can be deposited only by electron-induced reduction of ions within solutions without using any electrode reactions.

ii) In the case of previous deposition on emitter, the thin-film growth saturates at a certain thickness because of a self-limiting effect on electron injection. In the present case, in contrast, there is no limitation in the film thickness.

iii) The present mode makes it possible to deposit thin films onto various substrates including flexible sheets and insulating ones. In the previous deposition on the emitter surface, it was difficult to handle deposited films and to use them for further processing.

When the nc-Si emitter array with active-matrix driver [65,66] is used, high-throughput direct printing of nanostructured thin films can be realized in the same way as the parallel multi-beam

lithography. In addition, the printing scheme will make it possible to fabricate multi-layered and 3D nanostructures by sequential processes using different solutions. The more detailed discussion of the ballistic reduction mode are described in Chapter 5.

4.4 Summary

In summary, the printing deposition of thin Cu, Si, and Ge films using an nc-Si ballistic hot electron emitter was demonstrated. When Cu, Si, or Ge salt solution coated target substrates are irradiated with as-emitted electrons, reductive reaction of target ions efficiently proceeds followed by the growth of thin films. The compositional and structural analyses confirmed that Cl contamination of the deposited thin films is below the detection limit of XPS measurements. Further studies are required to determine whether the Cl signal detected from the SIMS analysis is attributed to the intrinsic contamination or the extrinsic one due to incomplete removal of residual solution. This approach is possibly available for deposition of other metals, group-IV semiconductors including SiGe, and their multilayers. As being a low-temperature, damage-less, and power-effective process, the electron incidence mode is potentially alternative means of thin film deposition on versatile substrates.

Chapter 5

Deposition mechanism

5.1 Introduction

Chapter 4 has showed experimental results of unilateral reduction effect of ballistic hot electrons emitted form nc-Si emitter. It has been demonstrated that thin Cu, Si, Ge, and SiGe films can be deposited under a printing scheme. This chapter discusses in more detail throughout the process from electron incidence to film deposition. A simplified deposition model in a printing process was designed based on classical nucleation theory and reaction-diffusion law. In the classical nucleation approach, the critical energy for nucleus formation in electron incidence was evaluated. This shows that the output electron energy of the nc-Si emitter is suitable for promoting preferential reduction of target ions within the penetration depth in solutions followed by the nuclei formation. To clarify mass transport in a solution, the space and time variation of the distribution of the generated nanoclusters are investigated by solving one dimensional reaction-diffusion equation. The dynamic behavior of the deposition rate in the printing mode is deduced from the theoretical analysis. The direct reduction model was supported separately by cyclic voltammetry analyses on the reducing activity of ballistic electrons. Finally, the characteristic features of the printing mode are summarized.

5.2 Modeling

In the electron printing scheme, unilateral reduction occurs in solutions differently from the exchange of thermalized electrons in the conventional electrode reaction. A schematic deposition model is shown in Fig. 5.1. Positive ions corresponding to a degree of dissociation are present in the solution coated on the target substrate. The existence of positive ions is consistent with the fact that $CuCl_2$, $CuSO_4$, $SiCl_4$, and $GeCl_4$ solutions used in the experiment are available for electroplating, and that thin Cu, Si, and Ge films are deposited on the cathodic substrate.

When ballistic electrons are irradiated on the solution, the electrons preferentially reduce the positive ions followed by nanocluster formation. At a typical electron incidence current density of J_e = 10 μA/cm^2, electrons impinge into a solution with a surface density of 6.2×10^{13} electrons·s^{-1}·cm^{-2}. This is comparable with the areal density of Cu^{2+}, Si^{4+}, and Ge^{4+} ions in the experimental solutions. Due to a fast reduction kinetics under electron incidence, a large number of nanoclusters are generated at an electron penetration depth (about 10 nm at an energy of 10 eV [86]), as indicated in Fig. 5.1. The thickness of the coated solution in our experiment is just about 100 nm that is much smaller than the diffusion length of nanoclusters in solution. Thus, densely generated nanoclusters are aggregated or deposited on the target substrate. Under a sequential electron incidence, a thin film is formed on the substrate surface. This deposition model is also supported by the fact that there is no gas evolution during the deposition process, and that thin films can be deposited onto insulating substrates.

In the reductive reaction of X^{n+} ions, that is $X^{n+} + ne^- \rightarrow X$, the film deposition rate R is expected to be proportional to the electron emission current density J_e [52,53]. At J_e = 10~100 μA/cm^2, for instance, the expected R values of Si and Ge are 0.19~1.9 and 0.21~2.1 nm/min, respectively. The observed film thicknesses of Si and Ge are consistent with the value expected from the deposition rate and the emitter operation time, as in the case of Cu deposition.

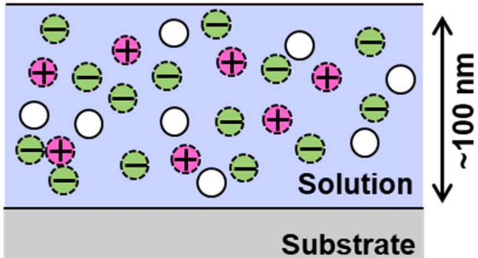

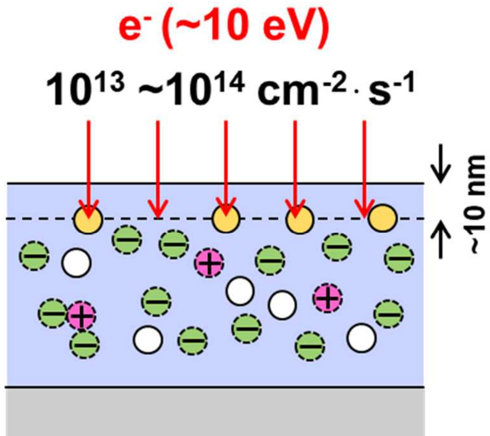

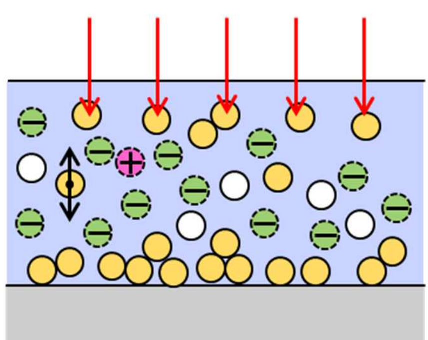

Figure 5.1 Schematic illustration of the thin film deposition process by ballistic electron printing. Under electron incidence, a significantly large number of atoms are generated at a penetration depth around the stopping power peak. This leads to the formation of nanoclusters, diffusion, and deposition onto the target substrate.

Figures 5.2 and 5.3 show schematic illustrations of the charge neutralization process and the current continuity in the dripping and the printing modes, respectively. In the dripping mode (Fig. 5.2), where a small amount of a salt solution is dripped on an emitter surface, associated with reduction of positive ions in a solution followed by nanocluster formation, the relative concentration of negative ions are increased. Possible pathway for preventing infinite negative charging and for promoting continuous thin film deposition is spontaneous neutralization of increased negative ions by meta-stable positive ions in the experimental ambient such as N_2^+、O_2^+、$H_3O^+(H_2O)_n$、$NH_4^+(H_2O)_n$ [87,88]. In fact, when the nc-Si electron emitter was driven in pure water and metal-salt solutions without using any counter electrodes, the pH value significantly increased with increasing the operation time as previously reported [73].

In thin film deposition on conductive target substrates under the printing mode, negative ions in solutions are relatively increased by reduction of positive ions under ballistic electron incidence as shown in Fig. 5.3. The diffused negative ions reach the target substrate surface and contribute to the external current flow through the carrier exchange for maintaining charge balance [89,90]. Thus, the current continuity is kept under the printing mode. Since the potential difference in the solution is much smaller than the voltage corresponding to the electrochemical window, no electrode oxidation reactions occurs at the target substrate surface. It is consistent with the facts that no gas evolution was observed during electron incidence and that the contamination level of thin Si and Ge films in the printing mode is considerably lower than that in electroplated ones. In the case of insulating target substrates (Fig. 5.3), on the other hand, relatively increased negative ions are steadily neutralized by meta-stable positive ions in experimental ambient similarly to the dripping case.

Another possible pathway for preventing negative charging and for promoting continuous thin film deposition in the printing mode is spontaneous neutralization by meta-stable positive ions generated by emitted ballistic electrons. Actually, in the case of low-vacuum varied-pressure scanning electron microscopy (VP-SEM), where effective electron energy is higher than the ionization energy of residual gas (e.g., 15.5 eV for N_2 gas [91]), it is possible to get stable images of insulating samples at higher pressures than 30 Pa without using any conductive coating owing to spontaneous charge

neutralization [92,93]. Further studies on this possibility should be sought for the printing mode in this study.

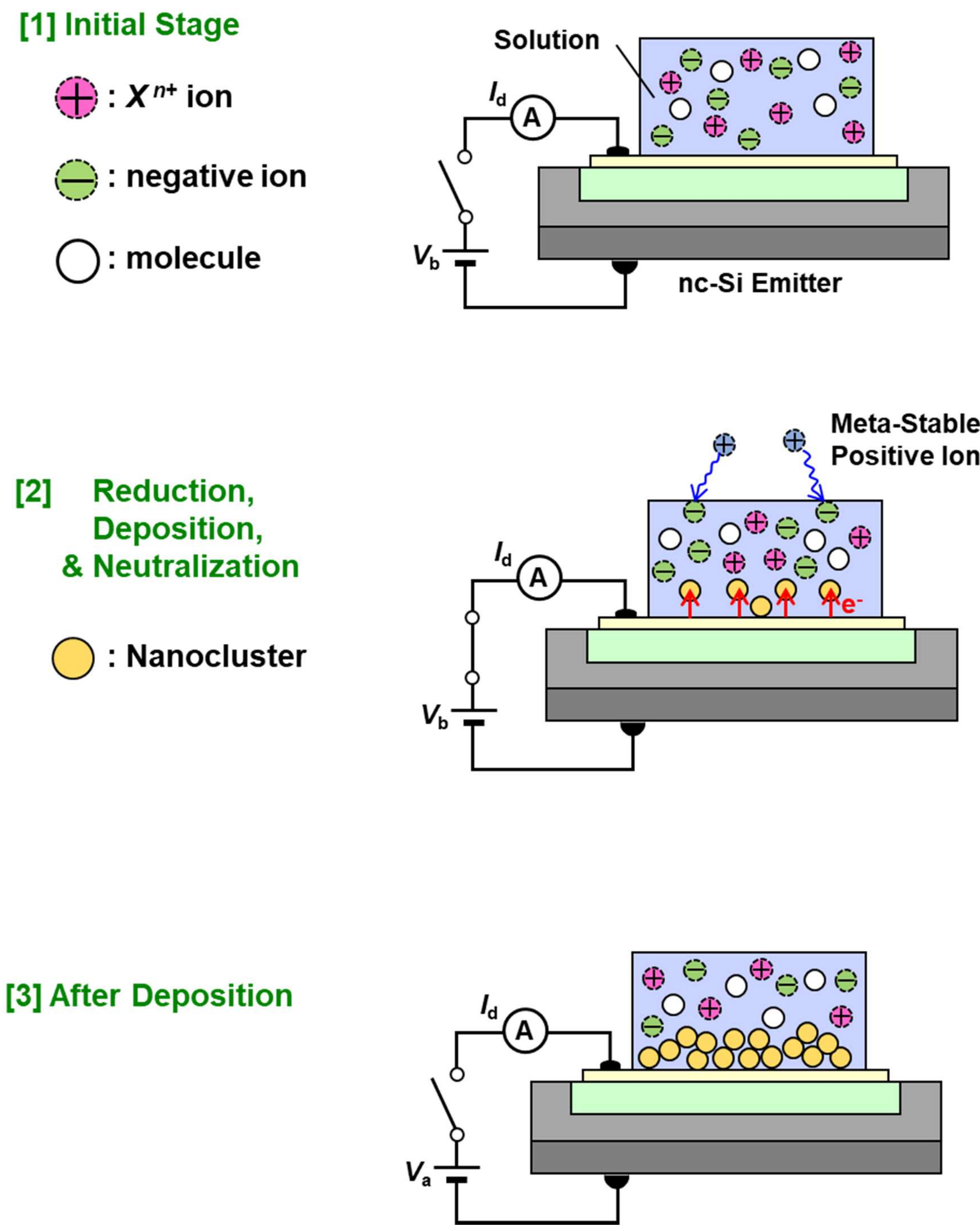

Figure 5.2 Schematic illustration of the charge neutralization in the dripping mode.

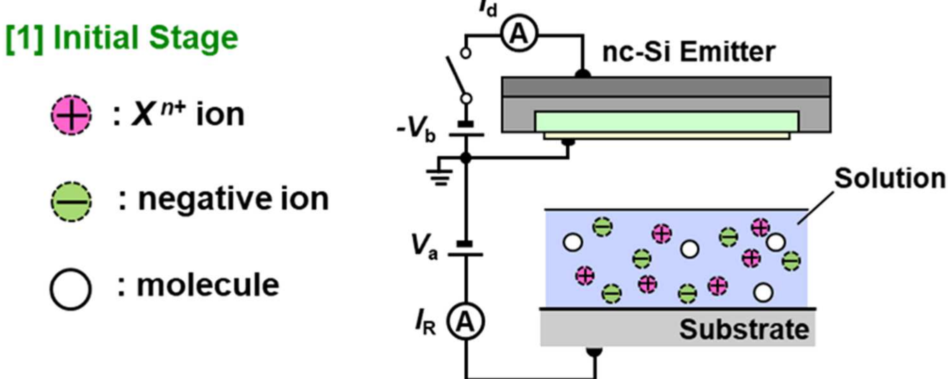

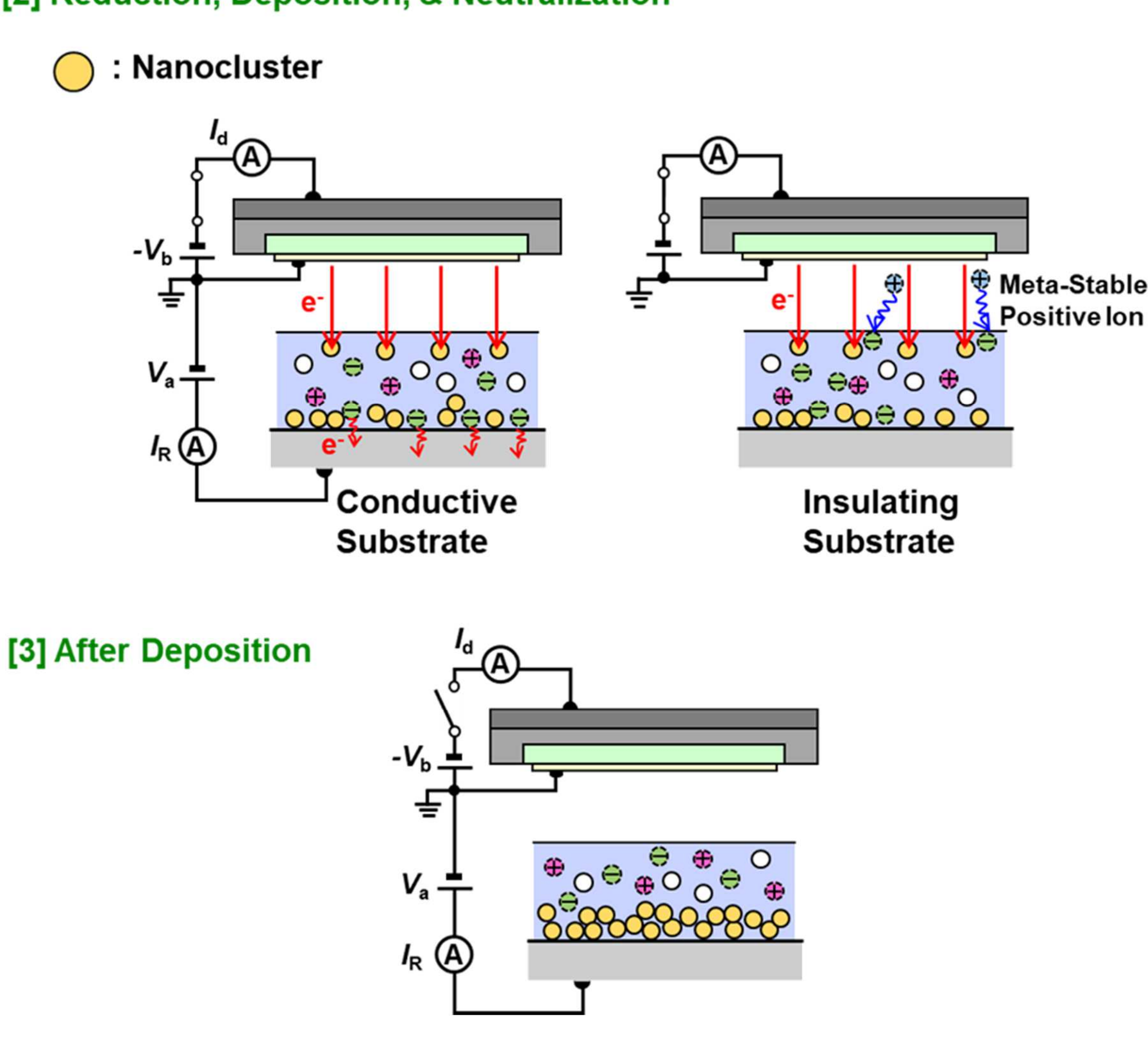

Figure 5.3 Schematic illustration of the current continuity (conducting target substrate) and the charge neutralization (insulating target substrate) in the electron printing mode.

5.3 Thermodynamic analysis

To clarify the triggering factor of nucleation, the free energy of a nanocluster formation ΔG is calculated as a function of incident electron energy on a basis of thermodynamic nucleation analysis. In contrast to the conventional electroplating, there are no electrode reactions in this deposition mode. Therefore, homogeneous nucleation scheme [94] is suitable for our modelling, where nuclei are directly formed in the solution. According to classical nucleation theory [94], the free energy of a nanocluster formation, ΔG, as a function of nanocluster radius r, is given by (assuming a spherical nucleus):

$$\Delta G = -\frac{4\pi}{3}\frac{\Delta\mu}{V}r^3 + 4\pi\alpha r^2 \tag{5.1}$$

where $\Delta\mu$ is the difference in chemical potential between a molecule in solution and that in the bulk of the crystal phase, and V is the volume occupied by each molecule in the crystal, and α is the surface free energy. The first term in the right side is related to the transfer of ions from solution to the crystal phase and the second to the increase of surface energy due to creation of the nanocluster. According to electroplating process [95], $\Delta\mu$ can be expressed as

$$\Delta\mu = en\eta \tag{5.2}$$

where e is the electron charge, n is the valence of the ion, and η is the overpotential. The V value is defined as $w/\rho N_A$ where w is the atomic weight, ρ is the density, and N_A is the Avogadro constant. Figure 5.4 shows the band diagram of ballistic electron emission from the nc-Si device and the subsequent reduction of X^{n+} ions. In this case ballistic hot electrons generated in the nc-Si layer are injected into a solution through a low-vacuum gap region. For simplicity, it is assumed here that the Fermi level in solution lies in the middle of the electrochemical window E_{EW}. From this figure, the relation between the electron energy E and the overpotential is given by

$$E = \eta + \frac{E_{EW}}{2} \tag{5.3}$$

Electron energy in this case corresponds to an effective external applied potential in the conventional electroplating. The calculation parameters [26,76,96] are summarized in Table 5.1.

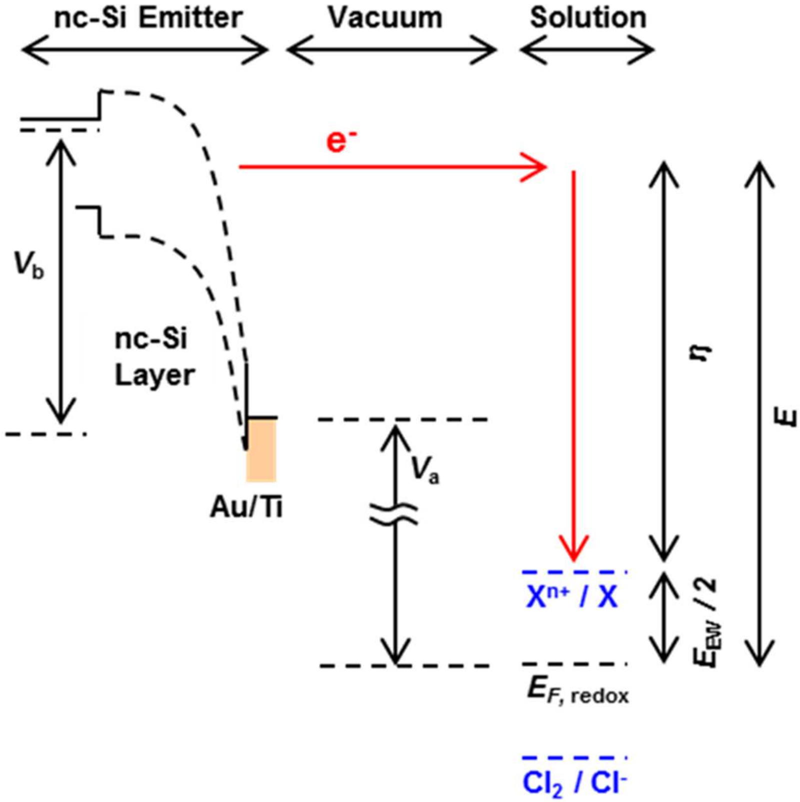

Figure 5.4 The band diagram of ballistic electron emission from the nc-Si device and subsequent reduction of X^{n+} ions followed by the thin film deposition (X= Cu, Si, or Ge). In this model, the Fermi level in the solution lies in the center of the electrochemical window. The electron energy E, the overpotential η, and the half of the electrochemical window $E_{EW}/2$ are shown in the figure.

Table 5.1. Material parameters used for calculation of the free energy of Si and Ge nanoclusters: density ρ, atomic weight w, surface tension α, and electrochemical window E_{EW} are referred to Refs. [26,76,96].

Material	ρ (g/cm^3)	w (g/mol)	α (mN/m)	E_{EW} (V)
Si	2.33	28.1	775	3.78
Ge	5.32	72.6	607	1.24

Figures 5.5(a) and 5.5(b) shows calculated ΔG vs. r curve for Si and Ge at different electron energies, where r is the radius of Si and Ge nanocluster. As suggested from Fig. 5.5(a), at electron incident energies of 1-2 eV, Si nanoclusters cannot be produced due to a positive value of the free

energy in any nanocluster radius. At an electron energy of 10 eV, on the other hand, the ΔG values of Si exhibits an abrupt decrease in the negative region with increasing r. The implication is that electron energy of 10 eV is suitable enough for promoting the spontaneous growth of Si nanoclusters followed by the formation of a thin film. This is consistent with the nanoclusters size of a thin Si film deposited by a dripping mode (about 10-20 nm) that was estimated from the transmission electron microscope (TEM) images [52,53]. Similar result was seen in the Ge case, as shown in Fig. 5.5(b), though the ΔG-r curves are different from Si at low electron energies due to a difference in the material parameter shown in Table 5.1. In either Si or Ge, output electrons of the nc-Si emitter meets well the requirement for the thermodynamic criterion. As a related experiment, thin film was deposited using a $SiCl_4$+$GeCl_4$ mixture (1:1 in volume ratio) solution, under incidence of electrons with a mean energy of 4 eV. In accordance with the result of EDX measurement, a significantly Ge-rich film (Si: Ge $\simeq$ 0.3:0.7) was deposited, as shown in Fig 5.6. Obviously Ge nanoclusters are preferentially formed at low electron energies. This is consistent with our model and the free energy behavior of Si and Ge shown in Figs. 5.5(a) and 5.5(b).

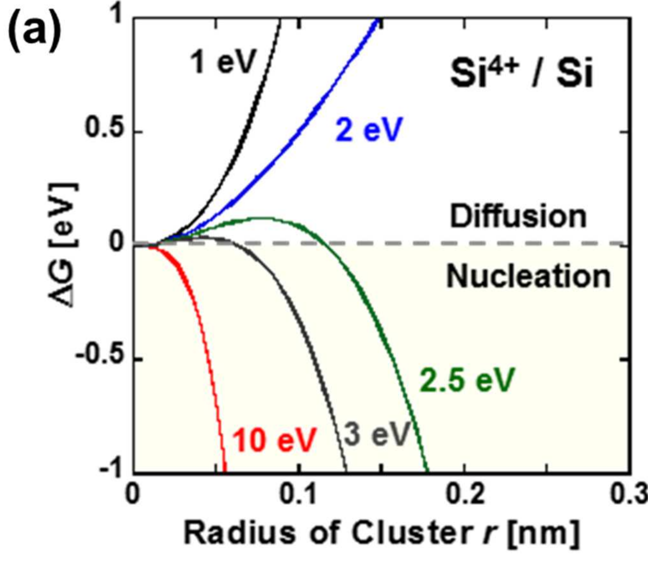

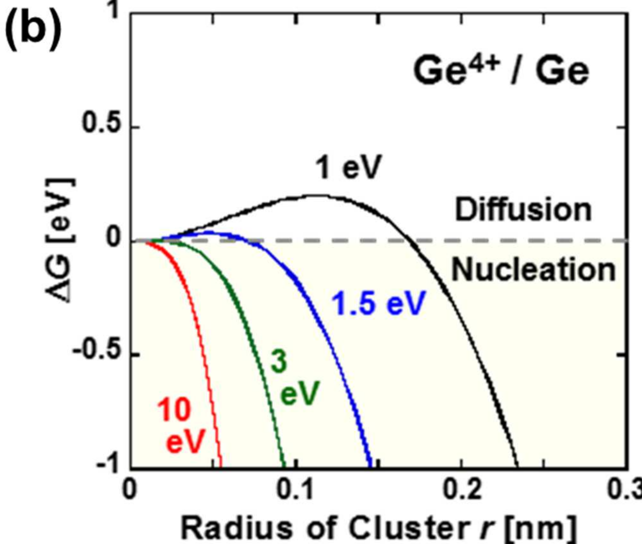

Figure 5.5 Free energy of formation of a Si (a) or a Ge (b) nanocluster as a function of nanocluster radius *r* at different electron incidence energies. There are two competitive processes in the incidence mode: diffusion and nucleation. The electron incidence at 10 eV meets well the requirement for the nucleation of Si and Ge.

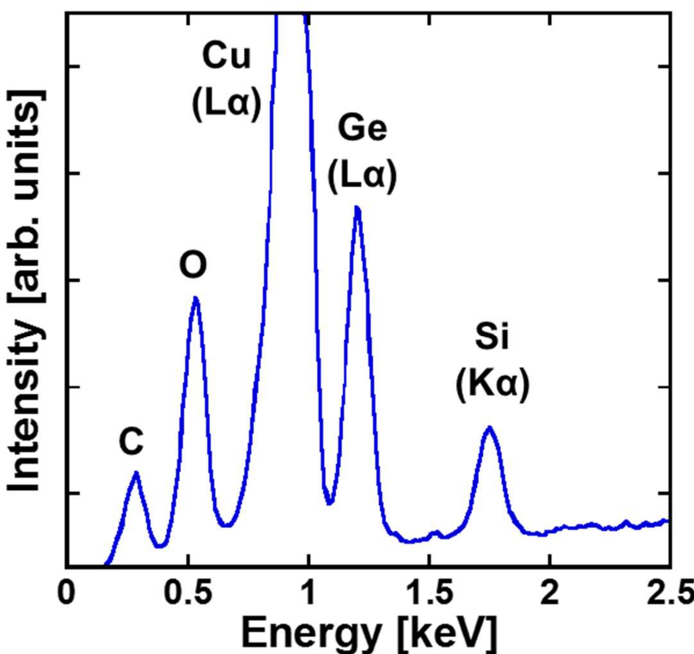

Figure 5.6 Measured EDX spectrum of thin SiGe film deposited by printing method. Ballistic electrons with an energy of 4 eV were irradiated to a mixture solution of $SiCl_4$+$GeCl_4$ (1:1). As a result of the quantitative analysis, it was found that the thin SiGe having a composition ratio of Si Ge of 0.3:0.7 was deposited on the Cu substrate.

5.4 Mass transport

The spatial and temporal change in the distribution of the generated nanoclusters is calculated for clarifying the deposition process. The schematic of the diffusion process of the nanoclusters in the printing scheme is shown in Fig. 5.7. Assuming that ballistic hot electrons uniformly impinge into a solution surface, the diffusion and generation of nanoclusters in the solution is described by 1D reaction-diffusion equation [97];

$$\frac{\partial [X]}{\partial t} = D\frac{\partial^2 [X]}{\partial x^2} + f \tag{5.4}$$

where $[X]$ is the density of the diffusing nanoclusters at location x and time t, D is the diffusion coefficient, and f describes a local reaction kinetics. The first and second terms on the right are the diffusion and reaction terms respectively. As discussed in thermodynamic analysis, all the ions at an electron penetration depth are instantaneously reduced into neutral atoms followed by formation nanoclusters. The local reaction kinetic f can be expressed as

$$f = \frac{1}{\sigma(r)} \frac{J_e}{nF} \delta(x - \lambda) \quad (5.5)$$

where J_e is the emission current density, n is the valence of the ion, F is the Faraday constant, λ is the penetration depth of incidence electrons, $\sigma(r)$ is number of atoms in a nanocluster, and $\delta(x)$ is Dirac delta function. Assuming a spherical nucleus, $\sigma(r)$ is given by

$$\sigma(r) = \frac{4\pi}{3} \frac{r^3}{V} \quad (5.6).$$

In a semi-infinite system, Eq. (5.4) has to be solved with the following initial and boundary conditions:

$$\begin{aligned} &[X] = 0 \quad (t = 0 \;\; or \;\; x = \infty) \\ &\frac{\partial [X]}{\partial x} = 0 \qquad (x = 0) \end{aligned} \quad (5.7)$$

When the virtual wave source is set so as to satisfy the boundary condition, the equation,

$$\frac{\partial [X]}{\partial t} = D \frac{\partial^2 [X]}{\partial x^2} + \frac{1}{\sigma(r)} \frac{J_e}{nF} \{\delta(x - \lambda) + \delta(x + \lambda)\} \quad (5.8)$$

is obtained. Since the Green's function of the diffusion equation [98] is

$$G(x, t; x', t') = \frac{1}{2\sqrt{\pi D(t - t')}} exp\left(-\frac{(x - x')^2}{4D(t - t')}\right) \quad (t > t') \quad (5.9)$$

the concentration distribution $[X]$ is

$$\begin{aligned} [X] &= \int_{-\infty}^{\infty} \int_{-\infty}^{\infty} G(x, t; x', t') \frac{1}{\sigma(r)} \frac{J_e}{nF} \{\delta(x' - \lambda) + \delta(x' + \lambda)\} dt' dx' \\ &= \frac{1}{\sigma(r)} \frac{J_e}{2nF\sqrt{\pi D}} \int_0^t \frac{1}{\sqrt{t - t'}} \left\{ exp\left(-\frac{(x - \lambda)^2}{4D(t - t')}\right) + exp\left(-\frac{(x + \lambda)^2}{4D(t - t')}\right) \right\} dt' \end{aligned} \quad (5.10).$$

Here, we denote

$$I = \int_0^t \frac{1}{\sqrt{t - t'}} exp\left(-\frac{(x - \lambda)^2}{4D(t - t')}\right) dt' \quad (5.11)$$

In order to solve Equation (5.11), the following variable conversion is performed.

$$A = \frac{(x - \lambda)^2}{4D} \quad (5.12)$$

$$T = t - t' \quad (5.13)$$

$$dT = -\mathrm{d}t' \quad (5.14)$$

Substituting the formulas (5.12), (5.13) and (5.14) into the formula (5.11) and rearranging it results in

$$I = -\int_{t}^{0} \frac{1}{\sqrt{T}} exp\left(-\frac{A}{T}\right) dT = \int_{0}^{t} \frac{1}{\sqrt{T}} exp\left(-\frac{A}{T}\right) dT \tag{5.15}$$

In order to solve the equation (5.15), the following variable transformation is further performed.

$$\epsilon = \frac{1}{T} \tag{5.16}$$

$$d\epsilon = -\frac{1}{T^2} dT \tag{5.17}$$

Substituting Equation (5.16) and (5.17) into the equation (5.15) yields the following equation

$$I = -\int_{\infty}^{\frac{1}{t}} \frac{1}{\varepsilon^{3/2}} exp(-A\varepsilon) d\varepsilon \tag{5.18}$$

Equation (5.18) can be solved by using the integral formula [99]

$$\int \frac{1}{x^{3/2}} exp(-Ax) dx = -\frac{2}{\sqrt{x}} exp(-Ax) - 2\sqrt{\pi A} erf(\sqrt{Ax}) \tag{5.19}$$

where

$$erf(x) = \frac{2}{\sqrt{\pi}} \int_{0}^{x} exp(-t^2) dt \tag{5.20}$$

Therefore, the solution of (5.15) is

$$I = 2\sqrt{t} exp\left(-\frac{(x-\lambda)^2}{4Dt}\right) - \sqrt{\frac{\pi}{D}} |x-\lambda| erfc\left(\frac{|x-\lambda|}{\sqrt{4Dt}}\right) \tag{5.21}$$

Substituting equation (5.18) into equation (5.7) yields

$$\begin{aligned} [X] = \frac{1}{\sigma(r)} \frac{J_e}{2nF\sqrt{\pi D}} \Bigg[& 2\sqrt{t} \left\{ exp\left(-\frac{(x-\lambda)^2}{4Dt}\right) + exp\left(-\frac{(x+\lambda)^2}{4Dt}\right) \right\} \\ & - \sqrt{\frac{\pi}{D}} \left\{ |x-\lambda| erfc\left(\frac{|x-\lambda|}{\sqrt{4Dt}}\right) + |x+\lambda| erfc\left(\frac{|x+\lambda|}{\sqrt{4Dt}}\right) \right\} \Bigg] \end{aligned} \tag{5.22}$$

where *erfc*(x) is complementary error function.

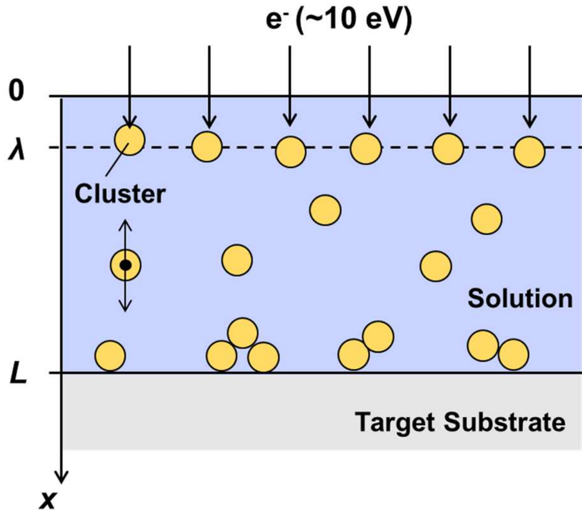

Figure 5.7 Schematic of boundary condition for solving one-dimensional reaction-diffusion equation. Nanoclusters generated at electron penetration length $x = \lambda$ diffuse in the solution and deposit on the target substrate ($x = L$).

Figure 5.8(a) shows the calculated spatial distribution of Si nanoclusters with r = 10 nm at three successive times. The diffusion coefficient is determined by the Stokes-Einstein equation [100]

$$D = \frac{k_B T}{6\pi\mu}\frac{1}{r} \tag{5.23}$$

where k_B is Boltzmann's constant, T is the absolute temperature, and μ is the viscosity of a solution. The calculation parameters are the same as those estimated for free energy (Table 5.1). When the concentration increases with increasing time, the spatial distribution of the concentration will flatten out, as suggested from the figure. For example, the nanocluster concentrations are uniformly distributed over 1 μm at >0.1 s. This means that generated nanoclusters easily propagate to a target substrate when a solution thickness is less than 1 μm. To investigate the nanocluster size dependence of the transport properties, the normalized spatial distributions with different nanocluster radius at t = 1 s are plotted, as shown in Fig. 5.8(b). The lager the nanocluster radius, the slower the nanoclusters diffuse into the solution. It is noted that the nanoclusters with radius of 1-100 nm easily diffuse from the solution surface to the target substrate within one second when the solution thickness is less than 1 μm. For Ge nanoclusters, the same results as Si nanoclusters are obtained, as shown in Figs. 5.9(a) and 5.9(b). These results support that diffusion kinetics plays an important role in the printing mode.

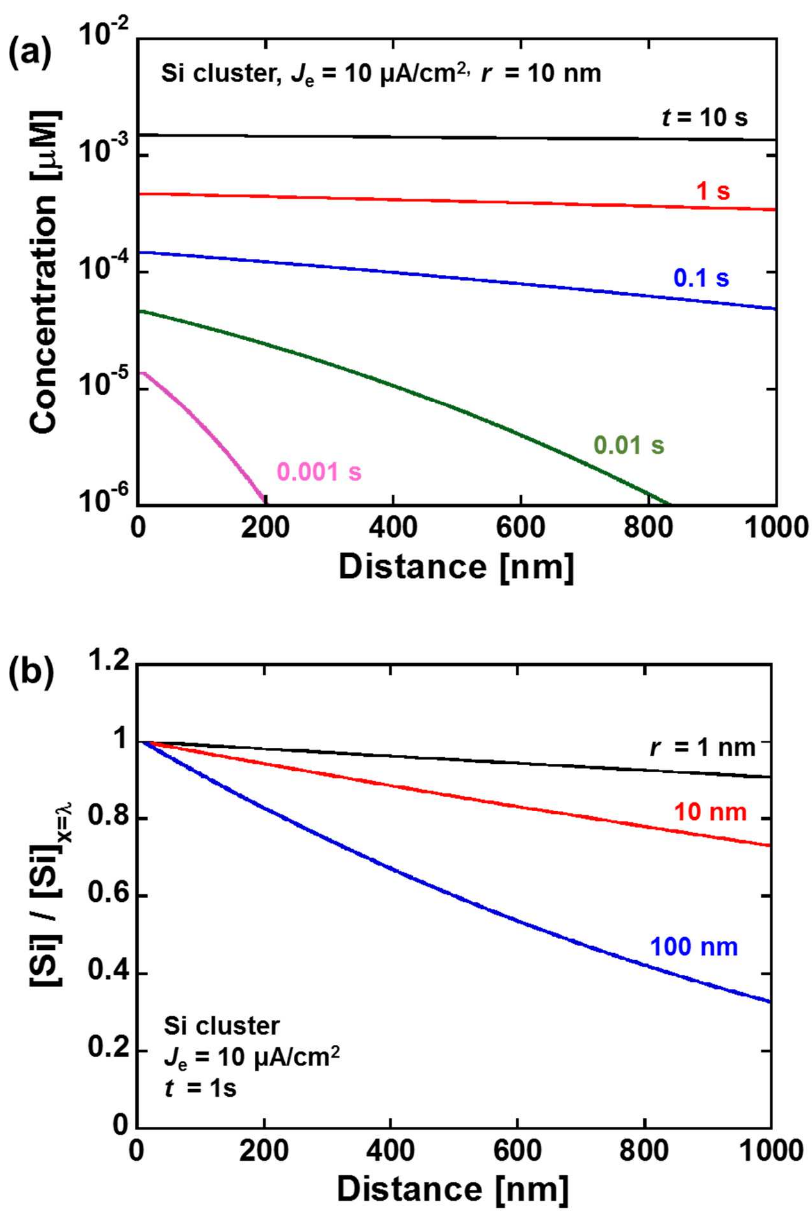

Figure 5.8 Spatial distribution of Si nanoclusters at each time (a) or nanocluster size (b). As the viscosity of the solution, the value of propylene carbonate (μ = 2.53 mPa·s) was used.

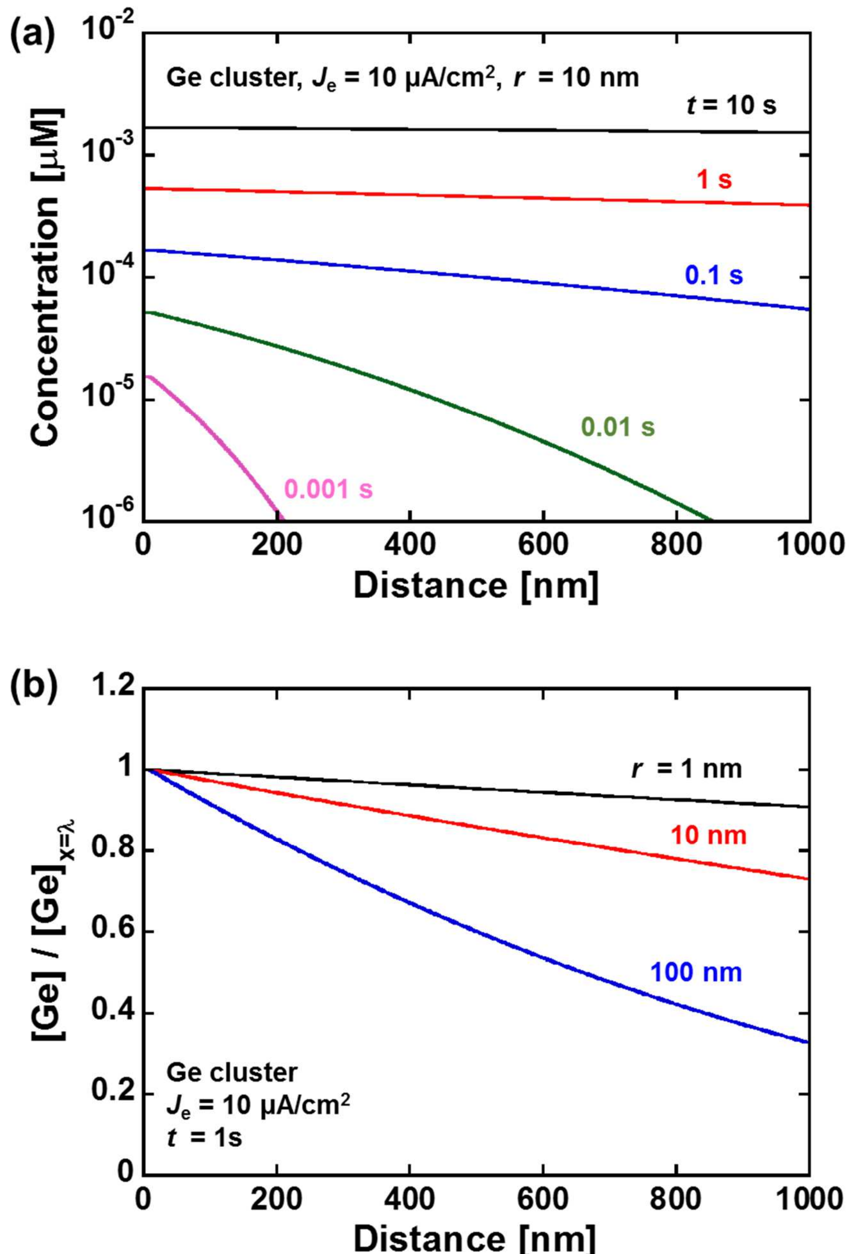

Figure 5.9 Spatial distribution of Ge nanoclusters at each time (a) or nanocluster size (b). As for the viscosity of the solution, the value of propylene carbonate (μ= 2.53 mPa·s) was used as in the case of Si.

Subsequently, the deposition rate under the printing scheme will be derived using Equation (5.22). The deposition rate R is expressed by the following equation using diffusion flux of the nanoclusters J.

$$R = \frac{w}{\rho}\sigma(r)J \tag{5.24}$$

From the Fick's law, the diffusion flux J is

$$J = -D\frac{\partial[X]}{\partial x} \tag{5.25}$$

By substituting Equation (5.23) into (5.25) and calculating it under the condition of $x > \lambda$, the following equation is obtained.

$$J = \frac{1}{\sigma(r)}\frac{J_e}{2nF}\left\{erfc\left(\frac{x-\lambda}{\sqrt{4Dt}}\right) + erfc\left(\frac{x+\lambda}{\sqrt{4Dt}}\right)\right\} \tag{5.26}$$

Substituting the above equation into Equation (5.24), the equation of the deposition rate is obtained.

$$R = \frac{w}{\rho}\frac{J_e}{2nF}\left\{erfc\left(\frac{x-\lambda}{\sqrt{4Dt}}\right) + erfc\left(\frac{x+\lambda}{\sqrt{4Dt}}\right)\right\} \tag{5.27}$$

This equation means that the deposition rate in the printing mode is determined primarily from the electron emission current density, as expected.

At a sufficient operation time, $t \rightarrow \infty$, the deposition rate is

$$R = \frac{wJ_e}{nF\rho} \tag{5.28}$$

This equation is consistent with the deposition rate obtained from Faraday's law (Equation (3.1)). The electron emission current density J_e plays an important role in the deposition rate as in the case of dripping mode. Figure 5.10(a) shows the relationship between calculated deposition rate of each material and electron irradiation time. The deposition rate rapidly increases at the initial stage of ballistic electron incidence and then saturates shortly at ~0.1 s. Its final value strongly depends on the electron emission current density. For the calculation of the deposition rate of Cu, the viscosity of the solvent was adjusted to the value of water (μ = 1.00 mPa·s). Figure 5.10(b) shows the relationship between the estimated thickness of deposited thin films and electron irradiation time for two different incident electron current densities. Since the deposition rate is saturated in a short time, the film thickness increases almost linearly with respect to the electron irradiation time. It has been made clear that the most important determining factor of this deposition mode is the dose of ballistic electrons rather than nucleation or diffusion process. These calculations are consistent with the experimental results as described in Chapter 4.

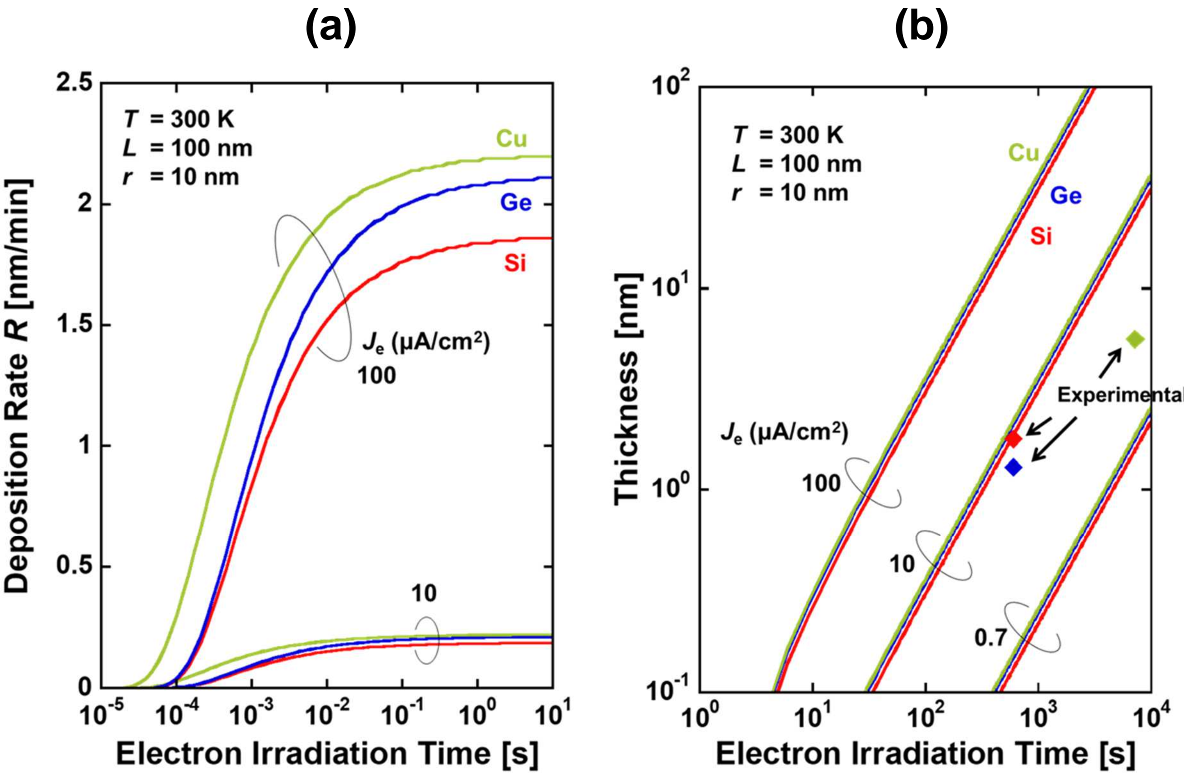

Figure 5.10 The deposition rate (a) and deposited film thickness (b) as a function of the electron irradiation time.

Then, the relation between time evolution of deposition rate and nanocluster size is investigated. Figure 5.11(a) is the time evolution of the deposition rate of thin Si films at each nanocluster radius. Although the saturation time of the deposition rate becomes longer with increase of the nanocluster radius, the deposition rate reaches to the steady value within 1 s even at r = 100 nm. Here, assuming that $L \gg \lambda$, the time $t_{80\%}$ at which the deposition rate reaches 80% of the saturation value, is

$$t_{80\%} \approx \frac{9L^2}{D} \tag{5.29}$$

Obviously the saturation time of the deposition rate is determined by the solution thickness and the diffusion coefficient. The $t_{80\%}$ of each solution thickness as a function of the radius of the Si nanocluster is shown in Fig. 5.9(b). The $t_{80\%}$ is proportional to the nanocluster radius. At L = 100 nm, thin film deposition starts within 100 s even at r = 10 μm. On the other hand, as L increases, $t_{80\%}$

abruptly changes. Especially at L = 10 μm, when the nanocluster radius is 100 nm, 1000 s or more is required to start thin film deposition. These results indicate that it is necessary to appropriately control the solution thickness coated to the target substrate under the printing scheme.

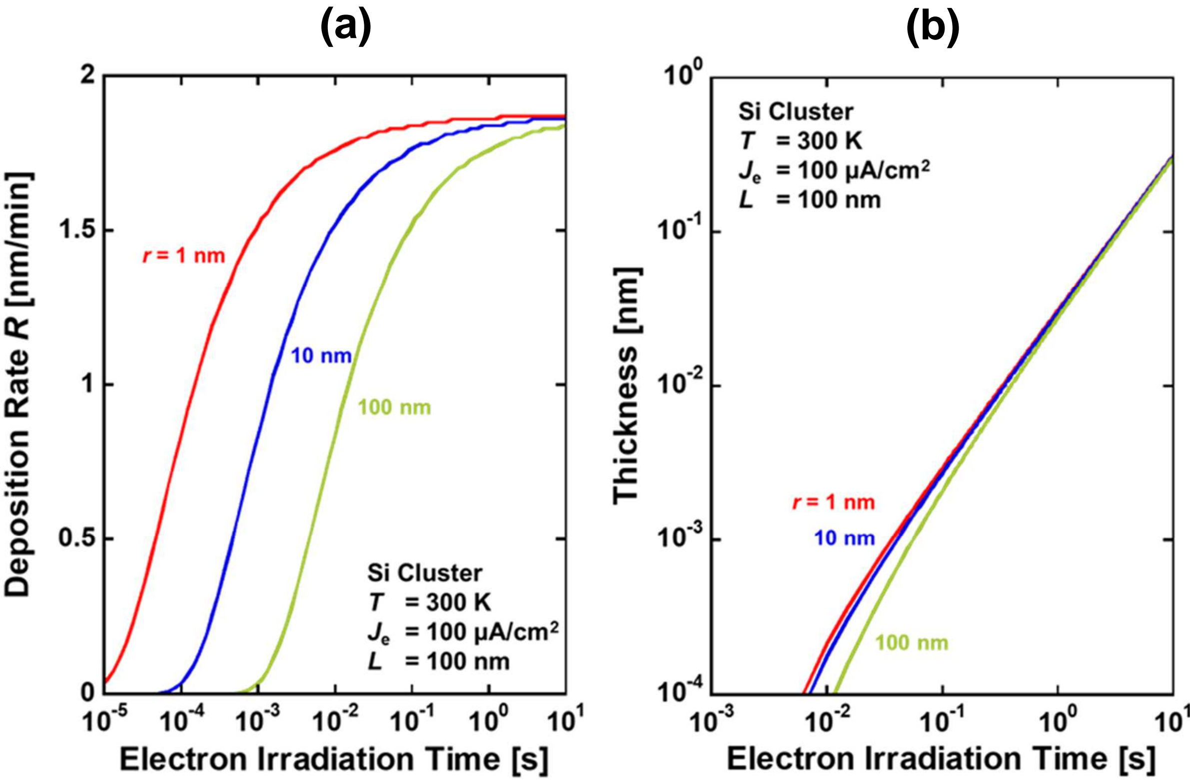

Figure 5.11 (a) Relationship between the deposition rate and electron irradiation time at different nanocluster sizes. (b) The time required for the thin film deposition rate to reach 80% of the steady value as a function of the nanocluster radius.

5.5 Further evidence

The electrochemical analysis shown in Fig. 5.12 provides further support for a unilateral reduction model. The mean kinetic energy of electrons emitted from nc-Si devices is quite larger than thermalized electrons. Thus, the nc-Si emitter can be used as an active cathode supplying highly reducing electrons. In fact, cyclic voltammogram measurements on several metal salt solutions in a standard three-electrode configuration suggested the reducing activity of the output electrons. The results of cyclic voltammetry measurement in a 0.1 M $CuSO_4$ aqueous solution are shown in Fig. 5.13. A significant anode current was clearly detected under operation of the nc-Si emitter at applied voltage higher than the onset of the emission (>5 V), as previously observed in either metal-salt, $SiCl_4$ or $GeCl_4$ solution [52,53]. In this figure, the result under the Pt–Pt configuration is also shown for reference. When a Pt sheet is used as a working electrode, in contrast, no significant anode current was observed in the range of electrochemical window. The increase of anode current becomes more apparent as the applied voltage increases. In addition, a color change presumably due to the thin film deposition appeared on the electron emitting area after the cyclic voltammetry measurement. It is expected that the ballistic hot electron injection leads to reduction reaction of $Cu^{2+} \rightarrow Cu$, followed by nucleation for thin film deposition, and then excess negative ions are collected at the counter electrode anode. As shown in Fig. 5.14, an increase of ionic conductivity due to ballistic electron injection under cyclic voltammogram has also been confirmed in semiconductor salt solutions [52,53]. This result supports that ballistic electron incidence leads to the thin film deposition under dripping or printing scheme.

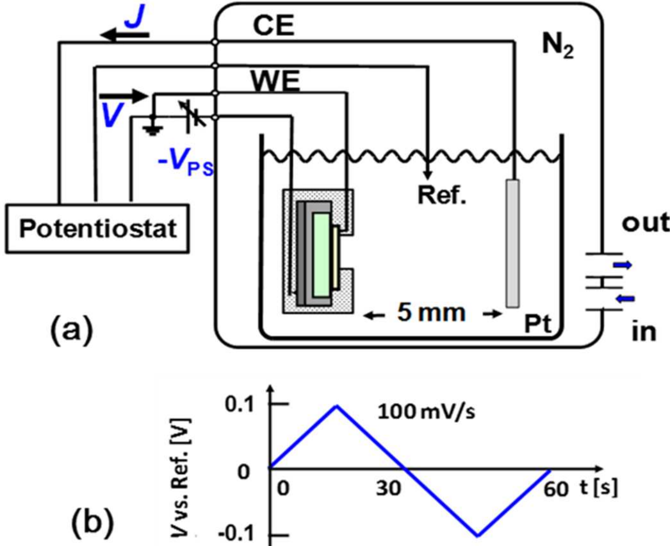

Figure 5.12 (a) The experimental setup of the nc-Si emitter operation for cyclic voltammetry measurements in 0.1 M $CuSO_4$ solution under a standard three-electrode configuration. (b) The emitter surface potential was scanned in the range of -0.1 to +0.1 V with respect to the standard electrode.

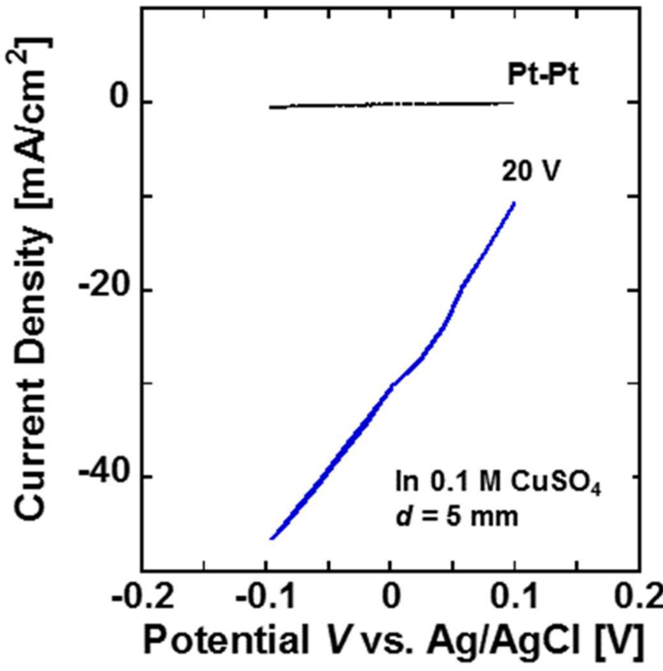

Figure 5.13 Measured cyclic voltammetry characteristics of the nc-Si emitter as a working electrode in 0.1 M aqueous solution of $CuSO_4$. The result under the Pt–Pt configuration is also shown for reference.

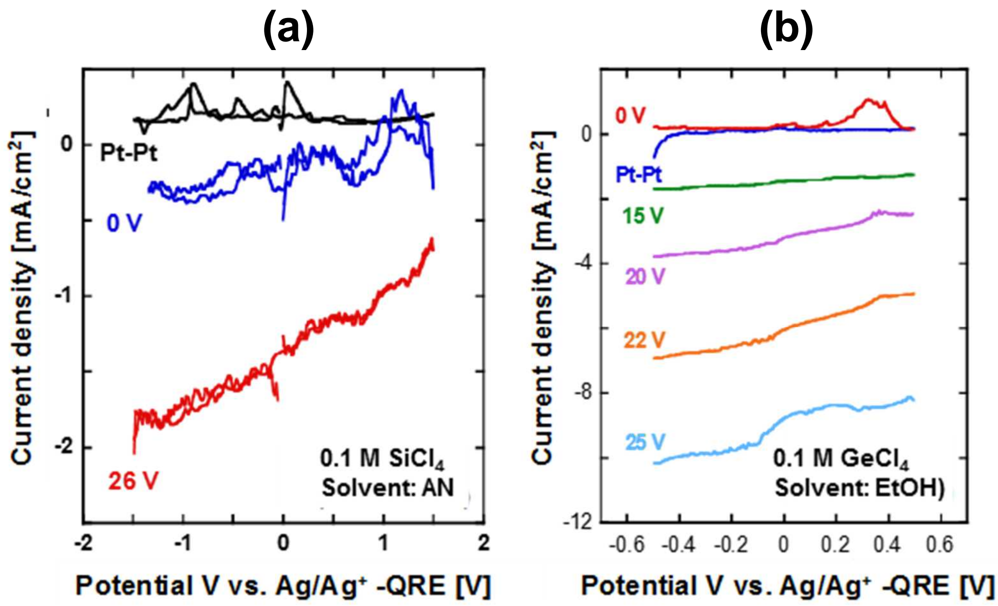

Figure 5.14 Cyclic voltammetry characteristics in $SiCl_4$ and $GeCl_4$ solution. Despite the sweep voltage within the range of the electrochemical window, injecting ballistic electrons into the solution markedly increases the ionic conductivity of the solution. Acetonitrile (AN) or ethanol (EtOH) is used as a solvent for $SiCl_4$ or $GeCl_4$ solution, respectively [52,53].

In addition, the nanoclusters size of the deposited films is 10-20 nm, as previously observed in TEM images for thin Si and Ge films deposited under a dipping mode, in which the emitter was dipped into the solution and electrons were injected into solutions. As suggested from Figs. 5.5(a) and 5.5(b), at an electron energy of 10 eV, the nanocluster formation immediately proceeds. Thermodynamically, there is no limitation in the nanocluster size. This point is discussed as a support of our model.

5.6 Characteristic features

The mechanisms for the present deposition mode and the previous mode (deposition on emitter) are common with each other in terms of the direct reduction of the target ions in the solution. In the previous dripping scheme, however, the thin-film growth tends to saturate at a certain thickness because of a self-limiting effect on electron injection. In contrast, there is no limitation in the film

thickness in the present case. Another advantage is that electron incidence mode is available for various substrates such as flexible and/or insulating ones. Actually, a thin Ge film was deposited on a thermally oxidized Si substrate as well, as shown in Fig. 5.15. In addition, handling of thin films deposited by electron incidence is easy for further processing.

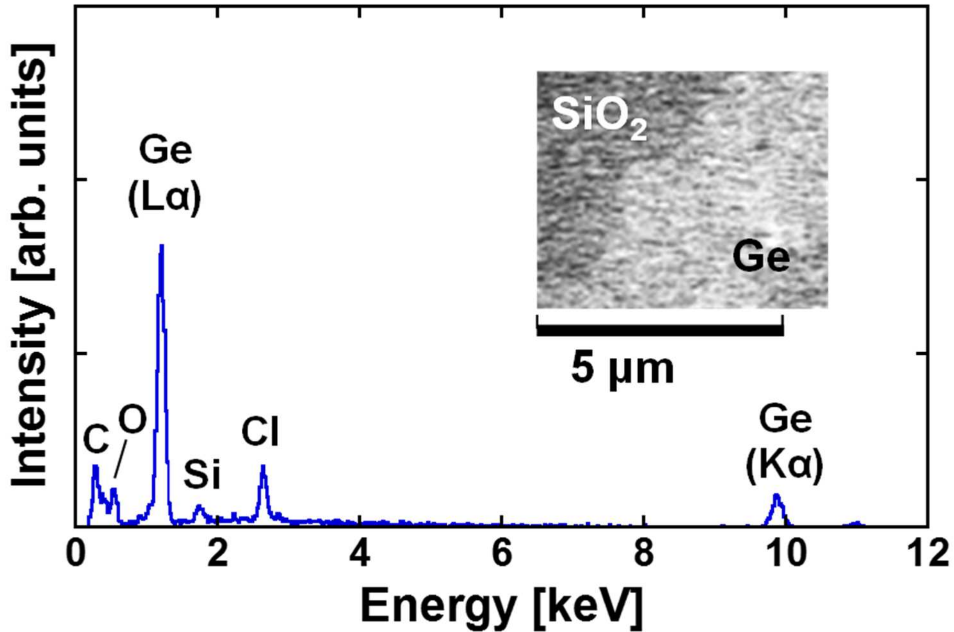

Figure 5.15 Measured EDX spectrum of thin Ge film deposited on thermally oxidized Si substrate by printing method. 0.5 M $GeCl_4$ (solvent: 1-ethyl-3-methylimidazolium dicyanamide) was used for the solution. Contamination of carbon and chlorine can be removed by additional cleaning method.

The characteristic features of a present scheme are summarized in Table 5.2 in comparison with conventional techniques. Chemical vapor deposition (CVD) has been used most widely in semiconductor manufacturing processes to form highly pure thin films with sufficiently suppressed contaminations less than ppb [1-11]. Many researchers have developed this deposition process since silicon was first deposited by hydrogen reduction of silicon tetrachloride in early 1900s [1,6]. Thermal CVD (T-CVD) has been used to deposit a wide range of materials including metals, semiconductors, and insulators. It is possible to control the nature of a deposited film structure by the proper manipulation of the deposition parameters such as temperature, pressure, and the selection of the

CVD reaction. Low-temperature growth of high-quality thin films has been required in semiconductor industry for the purpose of fabricating submicron electron devices like ultra-large scale integrated circuits (ULSI). For example, amorphous silicon films have been grown via plasma-enhanced CVD (PE-CVD) at 250 °C [1,14].

The electroplating has been used in interconnection and various surface coating areas [18]. In this thin film deposition technique, it is easily possible to deposit thin films on large substrates and structured surfaces. Actually, electroplating is effective for the formation of Cu wires in semiconductor manufacturing [18-20]. In addition, its application target have been extended to solar cell grade Si [37] and Si anode of lithium ion battery [38-40]. In the conventional electroplating approach for deposition of group-IV materials, electroplating of Si and Ge cannot be performed in aqueous solutions due to the low electrochemical stability of water. Though pure thin Si films have been already prepared by electrodeposition from molten salts, the experiments were carried at high temperatures range between 500 and 1400°C [21-23]. Several Si and Ge electrodepositions were demonstrated at room temperature using non-aqueous organic solutions [26-32] or ionic liquids [33-36]. In each case, however, the deposited films show non-uniform, porous, or contamination features of structure and composition. Generally, the structure and composition of electrodeposited films are strongly influenced by the electrode surface, solution, and supporting electrolyte. In addition, the evolution of Cl_2 gas at the counter anode is inevitable during the electrolysis. Thus, chemical contamination due to diffused Cl_2, O_2, and residual metals should be a critical issue in electroplating.

Electron beam induced deposition (EBID) techniques, on the other hand, have been demonstrated for thin-film deposition and nanowires formation. It is a direct write process where an electron beam with a high energy of 10-300 keV locally decomposes a precursor gas [44-47]. EBID traditionally relies on expensive gas phase metalorganic precursors that are not widely available for arbitrary elements and compounds. Large amounts of carbon and other species such as oxygen from the precursor fragments or incomplete precursor dissociation are deposited along with the metal, and the resulting material is often described as a matrix of carbon within which there is a little metal [46,47]. To overcome these problems, liquid-phase EBID (LP-EBID) techniques have been

developed using specially designed electrochemical cells [101-106] or ionic liquids [107-110]. Y. Liu et al. demonstrated electron beam induced deposition of Si nanodots from a $SiCl_4$ liquid precursor in a transmission electron microscope and a scanning electron microscope [106]. Silver microstructures were patterned by the electron beam irradiation to a room-temperature ionic liquid containing a silver salt, as reported by H. Minamimoto et al. [110].

Table 5.2 Comparison of thin film deposition method based on ballistic electron incidence with conventional dry or wet processes. T-CVD, PE-CVD EP, and EBID, represent thermal CVD, plasma-enhanced CVD, electroplating, and electron-beam-induced deposition, respectively.

Process		Phase	Mode	Temperature	Energy [eV]	Contamination	Pressure [Pa]	Material	Film structure
Dry	T-CVD	Gas	Decomposition	~1000 ℃	10^{-1}	<ppb	10^{5}	Metal, Semiconductor, Insulator	Amorphous, Polycrystalline, Single-crystal
	PE-CVD			~200 ℃	10^{3}		10^{1}		
Wet	EP	Liquid	Redox reactions	RT	10^{-2}	~1%	10^{5}	Metal	Polycrystalline
								Semiconductor	Amorphous
Electron incidence	EBID	Gas or liquid	Decomposition		10^{5}	>10%	10^{5}	Metal, Semiconductor	Amorphous
	This work	Liquid	Reduction		10^{1}	<300 ppm	10^{3}~10^{5}	Metal	Polycrystalline
								Semiconductor	Amorphous

The role of electron beam in EBID is completely different from the unilateral direct reduction in the incidence mode presented here in term of the energy and phenomenon. The simplicity of our system and cleanliness in deposition are other advantages to be noted. In contrast to the thin-film deposition under a dripping mode with the nc-Si emitter, there are no limitations in both the substrate materials and the film thickness in the printing mode. This technique is possibly applied to the deposition of a thin SiGe film using a mixture solution of $SiCl_4$+$GeCl_4$ as shown in Chapters 3 and 4. In addition, the present scheme will make it possible to fabricate multi-layered and 3D nanostructures by sequential processes using different solutions. This low-temperature, damage-free, and low-power process for depositing ultra-thin films and multilayered structure is potentially useful for fabrication of photonic and electronic thin film devices.

As discussed in Chapter 4, the Cl contamination of deposited thin films under printing mode was <300 ppm. In the deposition of thin semiconductor films by electroplating, in contrast, the Cl contamination is about 1% due to the influence of chlorine gas evolution and decomposition of the electrolyte at the anode electrode [8]. Although the EBID has some merits such as direct writing and high resolution capability, precursor gas decomposed by electron beam is inevitably included into the thin film. Thus, the contamination is remarkably as large as >10% [36]. The reductive electron printing scheme can deposit clean thin films as compared with electroplating or EBID.

In the electron printing scheme, thin film deposition is possible at room temperature like electroplating and EBID. Also, since the operating voltage of the nc-Si emitter is low (10-30 V), the printing scheme needs no high voltage power source as in the case of PE-CVD or EBID. However, there are some problems to be solved in this thin film deposition technique as follows.

i) As-deposited Si and Ge films are to be oxidized during electron incidence. To avoid the oxidation, it is necessary to keep the experimental condition such that the deposition system is completely free of oxygen and moisture.

ii) The deposited Si and Ge films include a certain amount of solution residue. More complete post-deposition cleaning process is required for removing the extrinsic contamination in the films.

iii) Microscopic mechanism of thin film deposition promoted by ballistic electron incidence should be further clarified to get high-quality thin films available for device fabrication.

5.7 Summary

The simple deposition model in the printing mode has been proposed. The thermodynamic nucleation analyses showed that the electron incidence at energy of 10 eV is a critical factor for triggering the nanocluster formation. The spatial distribution of generated nanoclusters was obtained by solving 1D reaction-diffusion equation in semi-infinite condition. The results indicate that the diffusion length of the nanoclusters is sufficiently larger than solution thickness. Furthermore, the calculated deposition rates were consistent with the experimental results. As being a low-temperature, damage-less, and power-effective process, the printing mode provides alternative means of thin film deposition on versatile substrates.

Chapter 6

Conclusions

6.1 Summary of each chapter

This study has investigated the thin film deposition effect utilizing highly energetic electrons emitted from the nc-Si ballistic hot electron emitter. By depositing thin Si, Ge, and SiGe films using the dripping mode, it was revealed that ballistic electrons easily reduce Si and Ge ions with high reduction potential. Subsequently, a printing method has been developed for depositing thin films on various substrates including insulating substrates. Deposition of thin Cu, Si, and Ge films using this printing method was demonstrated. The simple model of thin film deposition process was proposed based on classical nucleation theory and reaction-diffusion law from the experimental results. A summary of each chapter and future prospects will be described below.

Chapter 1

Flexible electronics technology for fabricating integrated circuits on bendable and stretchable substrates has attracted attention in recent years with the increase in the market. Compared with organic semiconductors commonly used in flexible electronics, inorganic semiconductors such as Si and Ge are expected to realize high mobility and high performance devices. However, these materials require an environment of high temperature and high vacuum for thin film deposition, so it is difficult to form a thin film on a heat-sensitive plastic substrate. Several present conditions and problems of deposition technology of thin inorganic semiconductor films including group-IV semiconductors for flexible electronics were summarized, and thus the purpose of this research was clarified.

Chapter 2

The principle and features of the nc-Si emitter used in this research, and the application in each medium were briefly summarized. In this electron emitter, electrons injected from a Si wafer substrate multiply tunnel through the nc-Si dots under high electric field, thereby emitting ballistic electrons with high directivity from the surface electrode. Based on these feature, applications as flat electron source of flat panel display and multi beam electron beam lithography has been considered. Since the energy of emitted electrons is higher than that of a thermalized electrons, this electron emitter operates also in air and solution, and particularly in metal or semiconductor salt solution, ballistic electrons directly reduce positive ions to form a thin film . In the previous research, there was a problem that polytetrafluoroethylene (PTFE) film used for protecting the emitter contaminates the deposited thin film with carbon.

Chapter 3

The dripping method was proposed in which a very small amount of solution is dripped on the nc-Si emitter surface to deposit thin films. It was confirmed by this method that Si and Ge thin films with Cl contamination below the detection limit of EDX and XPS deposited on the emitter surface. It was shown that SiGe thin film deposited by using mixture solution of $SiCl_4$+$GeCl_4$. The structure and the resistivity of the thin Cu film deposited on the emitter surface under the dripping mode was polycrystalline and 561 μΩ·cm, respectively.

Chapter 4

The printing method was developed in which an nc-Si emitter is placed in close proximity to a target substrate coated with a solution, and then ballistic electrons are irradiated on the target substrate to deposit the thin film. Thin Cu films were deposited by irradiating ballistic electrons on Si or thermally oxidized Si substrates coated with $CuCl_2$ solution. It has been demonstrated that thin film deposition is also possible by this printing mode. Using $SiCl_4$ and $GeCl_4$ solutions, thin Si and Ge films can be deposited also on Cu substrates. Spectroscopic measurements indicate that the deposited

thin Si and Ge films consisted of very small nanoclusters. The Cl contaminations suggested from XPS and SIMS measurements for these films were below 300 ppm.

Chapter 5

Based on the results in Chapter 4, a simple thin film deposition model was proposed. Using the thermodynamic nucleation theory, it was shown that the energy of incident ballistic electrons meets well the requirement for nucleation. The electron energy difference for nucleation between Si and Ge affect the composition ratio of SiGe films deposited using a mixture solution of $SiCl_4$+$GeCl_4$ (1:1 in volume ratio). According to the reaction-diffusion analyses, nanoclusters formed at the electron penetration depth (~10 nm) in the solutions quickly reaches the target substrate. The derived deposition rate suggests that the most important determining factor in the reductive deposition mode is the dose of ballistic electrons rather than nucleation or diffusion process. The reducing activity of ballistic electrons was also supported in cyclic voltammogram measurements. Finally, comparison of this printing method with other dry or wet processes showed that the present method is useful as a, low cost, and low temperature process.

6.2 Future prospects

The future prospects of this research are summarized below. In order to understand the deposition process from the nucleation by ballistic electron irradiation, it is necessary to elucidate the thin film deposition process from a microscopic viewpoint. By using different solutions, multilayer film structures and three dimensional structures will be fabricated. This technique is potentially useful for fabricating devices such as thin film transistors.

References

[1] Handbook of Thin Film Deposition, 3rd ed. edited by K. Seshan (William Andrew Publishing, Waltham, 2012).

[2] 日本学術振興会薄膜第 131 委員会編: 薄膜ハンドブック, オーム社, (1983).

[3] J. L. Vossen and W. Kern, Thin Film Processes II, (Academic Press, 1991).

[4] J.A. Venables, Introduction to Surface and Thin Film Processes (Cambridge, 2000).

[5] H. Park and T. S. Sudarshan, Chemical Vapor Deposition, (ASM International, Metals Park, OH, 2001).

[6] H.O. Pierson, Handbook of Chemical Vapor Deposition: Principles, Technology, and Applications, (William Andrew Inc, 1999).

[7] M.L. Hitchman and K.F. Jensen, Chemical Vapor Deposition, (Academic Press, 1993).

[8] K. Nagamine, A. Yamada, M. Konagai, and Kiyoshi Takahashi, Jap. J. Appl. Phys. 26 L951 (1987).

[9] L. Guo, M. Kondo, M. Fukawa, K. Saitoh, and A. Matsuda, Jpn. J. Appl. Phys. 37 L1116 (1998).

[10] C.-H. Lee, A. Sazonov, and A. Nathan, Appl. Phys. Lett. 86 222106 (2005).

[11] S. E. Babayan, J. Y. Jeong, V. J. Tu, J. Park, G. S. Selwyn, and R F Hicks, Plasma Sources Sci. Technol. 7 286 (1998).

[12] K. Suganuma, Introduction to Printed Electronics, (Springer, New York, 2014).

[13] http://www.aist.go.jp/Portals/0/resource_images/aist_j/aistinfo/aist_today/vol13_01/vol13_01_p07.pdf

[14] Y. Sun and J. A. Rogers, Adv. Mater. 19 1897 (2007).

[15] M. G. Kane, L. Goodman, A. H. Firester, P. C. Wilt, A. B. Limanov, and J. S. Im, Tech Dig. - Int. Electron Devices Meet. 939 (2005).

[16] E. M. C. Fortunato, P. M. C. Barquinha, A. C. M. B. G. Pimentel, A. M. F. Gonçalves, A. J. S. Pereira, Appl. Phys. Lett. 85 2541 (2004).

[17] I.-D. Kim, Y. Choi, H. L. Tuller, Appl. Phys. Lett. 87 043509 (2005).

[18] Modern Electroplating, Electrochemical Society Series, 5th ed, edited by M. Schlesinger, M. Paunovic, (Wiley, New York, 2010).

[19] P. C.Andricacos, C. Uzoh, J. O. Dukovic, J. Horkans, and H. Deligianni, IBM J. Res. Dev. 42 567 (1998).

[20] A. W. Topol, D. C. La Tulipe Jr., L. Shi, D. J. Frank, K. Bernstein, S. E. Steen, A. Kumar, G. U. Singco, A. M. Young, K. W. Guarini et al., IBM J. Res. Dev. 50(4/5) 491 (2006).

[21] R. Boen and J. Bouteillon, J. Appl. Electrochem. 13 277 (1983).

[22] D. Elwell, J. Appl. Electrochem. 18 15 (1988).

[23] A. L. Bieber, L. Massot, M. Gibilaro, L. Cassayre, P. Taxil, and P. Chamelot, Electrochim. Acta 62 282 (2012).

[24] Y. Takeda, R. Kanno, O. Yamamoto, T. R. R. Mohan, C.-H. Lee, and F. A. Koger, J. Electrochem. Soc. 128 1221 (1981).

[25] J. Gobet and H. Tonnenberger, J. Electrochem. Soc. 135 109 (1988).

[26] M. Qiu-Ping, L. Wen, W. Bao-cheng, and M. Qing-sen, Adv. Mater. Res. 79 1635 (2009).

[27] J. P. Nicholson, J. Electrochem. Soc. 152 C795 (2005).

[28] Y. Nishimura and Y. Fukunaka, Electrochim. Acta 53 111 (2007).

[29] M. Bechelany, J. Elias, Pierre Brodard, J. Michler, and L. Philippe, Thin Solid Films 520 1895 (2012).

[30] M Saitou, K Sakae, and W. Oshikawa, Surf. Coat. Technol. 162 101 (2003).

[31] M. S. Z. Abidein, R. Matsumura, M. Anisuzzaman, J-H Park, S. Muta, M. R. Mahmood, T. Sadoh, and A. M. Hashim, Materials 6 5047 (2013).

[32] M. S. Z. Abidin, Shahjahan, M. R. Mahmood, A. M. Hashim, Jurnal Teknologi, 72:1 77 (2015).

[33] S. Z. E. Abedin, N. Borissenko, and F. Endres, Electrochem. Commun. 6 510 (2004).

[34] Y. Nishimura, T. Nohira, T. Morioka, and R. Hagiwara, Electrochem. Commun. 77 683 (2009).

[35] G. Pulletikurthi, A. Lahiri, T. Carstens, N, Borisenko, S. Z. E. Abedin, F. Endres, J. Solid State Electrochem. 17 2813 (2013).

[36] M. Wu, N. R. Brooks, S. Schaltin, K. Binnemans, and J. Fransaer, Phys. Chem. Chem. Phys. 15 4955 (2013).

[37] P. Peinado, S. Sangiao, and J. M. D. Teresa, ACS Nano 9 (6) 6139 (2015).

[38] G. Zhao, Y. Meng, N. Zhang, and K. Sun, Mater. Lett. 76 55 (2012).

[39] R. Epur, M. Ramanathan, F. R. Beck, A. Manivannan, and P. N. Kumta, Mater. Sci. Eng. B 177 1157 (2012).

[40] B. Gattu, R. Epur, P. M. Shanti, P. H. Jampani, R. Kuruba, M. K. Datta, A. Manivannan, and P. N. Kumta, Inorganics 5 27 (2017).

[41] T. Shimoda, Y. Matsuki, M. Furusawa, T. Aoki, I. Yudasaka, H. Tanaka, H. Iwasawa, D. Wang, M. Miyasaka, Y. Takeuchi, Nature 440 783 (2006).

[42] Y. Jin, J. Wang, B. Sun, J. C. Blakesley, and N. C. Greenham, Nano Lett. 8 1649 (2008).

[43] E. Menard, K. J. Lee, D.-Y. Khang, R. G. Nuzzo, J. A. Rogers, Appl. Phys. Lett. 84 5398 (2004).

[44] S. Randolph, J. Fowlkes, and P. Rack, Critical Rev. of Solid State and Mater. Sci. 31(3) 55 (2006).

[45] K. Furuya, Sci. Technol. Adv. Mater. 9(1) 014110 (2008).

[46] W. F. van Drop and C. W. Hagen, J. Appl. Phys. 104 081301 (2008).

[47] A. Botman, J. J. L. Mulders, and C. W. Hagen, Nanotechnology 20 372001 (2009).

[48] J. Xu and G. M. Haarberg, High Temp. Mater. Proc. 32(2) 97 (2013).

[49] N. Koshida, T. Ohta, B. Gelloz, and A. Kojima, Current Opinion in Solid State and Mater. Sci. 15 183 (2011).

[50] T. Ohta, B. Gelloz, and N. Koshida, Electrochem. Solid-State Letters 13 D73 (2010).

[51] T. Ohta, B. Gelloz, and N. Koshida, Jpn. J. Appl. Phys. 50 06GG03 (2011).

[52] T. Ohta, B. Gelloz, and N. Koshida, Appl. Phys. Lett. 102, 022107 (2013).

[53] N. Koshida, A. Kojima, T. Ohta, R. Mentek, B. Gelloz, N. Mori, J. Shirakashi, ECS Solid State Lett. 3(5) P57 (2014).

[54] O. Bisi, S. Ossicini, and L. Pavesi, Surf. Sci. Rep. 38(1-3) 1 (2000).

[55] Properties of Porous Silicon, edited by L. Canham (Institute of Electrical Engineers, London, 1997).

[56] B. Gelloz and N. Koshida, in: Handbook of Luminescence, Display Materials, edited by H.S. Nalwa and L. S. Rohwer (American Scientific Publishers, Stevenson Ranch, CA, 2003).

[57] H. Shinoda, T. Nakajima, K. Ueno, and N. Koshida, Nature 400 853-855 (1999).

[58] N. Koshida, X. Sheng, and T. Komoda, Appl. Surf. Sci. 146 371 (1999).

[59] K. Nishiguchi, X. Zhao, and S. Oda, J. Appl. Phys. 92 2748 (2002).

[60] 小島明, 池上尚克, 須田隆太郎, 越田信義, 第 64 回応用物理学会春季学術講演会, 講演予稿集, 14p-424-14.

[61] N. Mori, H. Minari, S. Uno, H. Mizuta, and N. Koshida, Appl. Phys. Lett. 98 062104 (2011).

[62] A. Kojima and N. Koshida, Appl. Phys. Lett. 86 022102 (2005).

[63] T. Ichihara, T. Hatai, K. Aizawa, T. Komoda, A. Kojima, and N. Koshida, J. Vac. Sci. & Technol. B 22 57 (2004).

[64] A. Kojima, T. Ohta, N. Koshida, and H. Ohyi, Proc. SPIE Adv. Lithography 7637 763712 (2010).

[65] N. Koshida, A. Kojima, N. Ikegami, R. Suda, M. Yagi, J. Shirakashi, H. Miyaguchi, M. Muroyama, S. Yoshida, K. Totsu, and M. Esashi, J. of Micro/Nanolithography, MEMS, and MOEMS 14 (3) 031215 (2015).

[66] H. Nishino, S. Yoshida, A. Kojima, N. Ikegami, S. Tanaka, N. Koshida, and M. Esashi., Electron. Comm. Jpn. 99 146 (2016).

[67] M. Esashi, A. Kojima, N. Ikegami, H. Miyaguchi, and N. Koshida, Microsystems & Nanoengineering 1 15029 (2015).

[68] A. Kojima, N. Ikegami, H. Miyaguchi, T. Yoshida, R. Suda, S. Yoshida, M. Muroyama, K. Totsu, M. Esashi, and N. Koshida, Proc. SPIE Adv. Lithography 10144 101440L (2017).

[69] T. Ichihara, T. Hatai and N. Koshida, J. Soc. Information Display 18 (3) 223 (2010).

[70] T. Ohta, A. Kojima, H. Hirakawa, T. Iwamatsu, and N. Koshida, J. Vac. Sci. Technol. B 23 2336 (2005).

[71] T. Ohta, A. Kojima, and N. Koshida, J. Vac. Sci. Technol. B 25 524 (2007).

[72] N. Koshida, T. Ohta, and B. Gelloz, Appl. Phys. Lett. 90 163505 (2007).

[73] T. Ohta, B. Gelloz, and N. Koshida, J. Vac. Sci. Technol. B 26 716 (2008).

[74] J. A. Bearden, Rev. Mod. Phys. 36 78 (1967).

[75] Practical Surface Analysis by Auger and X-ray Photoelectron Spectroscopy, ed. M.P. Seah and D. Briggs (Wiley, Chichester, U.K., 1983) Appendix 5.

[76] Handbook of Chemistry and Physics, 90th ed. edited by D. R. Lide (CRC Press, New York, 2009).

[77] M. J. Deng, P. Y. Chen, T. I. Leong, W. Sun I, J. K. Chang, and W. T. Tsai, Electrochem. Commun. 10, 213 (2008).

[78] T. I. Leong, I. W. Sun, M. J. Deng, C. M. Wu, and P. Y. Chen, J. Electrochem. Soc. 155 F55 (2008).

[79] L. D'Urzo, S. Schaltin, A. Shkurankov, H. Plank, G. Kothleitner, C. Gspan, K. Binnemans, and J. Fransaer, J. Mater. Sci: Mater. Electron. 23 945 (2012).

[80] Practical Surface Analysis: volume 2, Ion and Neutral Spectroscopy, 2nd ed., edited by D. Briggs and M.P. Seah (Wiley, Chichester, U.K., 1992).

[81] D. E. Aspnes and A. A. Studna, Phys. Rev. B 27 985 (1983).

[82] J.H. Parker, Jr., D. W. Feldman, and M. Ashkin, Phys. Rev. 155 712 (1967).

[83] J. Fortner, R. Q. Yu, and J.S. Lannin, Phys. Rev. B 42 7610 (1990).

[84] M. Mulato, D. Toet, G. Aichmayr, P. V. Santos, and I. Chambouleyron, Appl. Phys. Lett. 70 3570 (1997).

[85] S. Hayashi and H. Abe, Jpn J. Appl. Phys. 23 L824 (1984).

[86] D. Emfietzoglou, I. Kyriakou, I. Abril, R. Garcia-Molina, I. D. Petsalakis, H. Nikjoo, A. Pathak, Nucl. Instr. & Meth. Phys. Res. B 267 45 (2009).

[87] 静電気学会編: 静電気ハンドブック, オーム社, (1981).

[88] 高分子学会編: 静電気ハンドブック, 地人書館, (1967).

[89] A. J. Bard and L. R. Faulkner, Electrochemical Methods: Fundamentals and Applications, 2nd ed., (Wiley, 2001).

[90] 電気化学会編: 電気化学便覧 第 6 版, 丸善, (2013).

[91] E. Kuffel, W. S. Zaengl and J. Kuffel, High Voltage Engineering: Fundamentals (Oxford, 2000).

[92] D. J. Stokes, Principles and Practice of Variable Pressure/Environmental Scanning Electron Microscopy (VP-SEM), (Wiley, 2008).

[93] 日本顕微鏡学会関東支部編: 新・走査電子顕微鏡, 共立出版, (2011).

[94] Crystal Growth Theory and Techniques, vol. 1, edited by C. H. L. Goodman (Plenum, London, 1974); pp 54-68.

[95] M. Paunovic and M. Schlesinger, Fundamentals of Electrochemical Deposition, 2nd ed. (John Wiley & Sons, New York, 2006); pp 113-138.

[96] B.J. Keene, Int. Mater. Rev. 38 157 (1993).

[97] J. Crank, THE MATHEMATICS OF DIFFUSION, 2nd ed. (Oxford University Press, London, 1976).

[98] 小泉義晴, 微分方程式と量子統計力学のグリーン関数, (東海大学出版会, 2010).

[99] 大槻義彦 監修, 室谷義昭 訳, 新数学公式集 I 初等関数, (丸善, 1991).

[100] I. N. Levine, PHYSICAL CHEMISTRY, 6nd ed. (McGraw-Hill, New York, 2009).

[101] G. Schardein, E. U. Donev, and J T Hastings, Nanotechnology 22 015301 (2011).

[102] E. U. Denov, G. Schardein, J. C. Wright, and J. T. Hastings, Nanoscale 3 2709 (2011).

[103] K. W. Noh, Y. Liu, L. Sun, and S. J. Dillon, Ultramicroscopy 116 34 (2012).

[104] M. Bresin, A. Chamberlain, E. U. Donev, C. B. Samantaray, G. S. Schardien, and J. T. Hastings, Angew. Chem. Int. Ed. 52 8004 (2013).

[105] M. den Heijer, I. Shao, A. Radisic, M. C. Reuter, and F. M. Ross, APL Mater. 2 022101 (2014).

[106] Y. Liu, X. Chen, K. W. Noh, and S. J. Dillon, Nanotechnology 23 385302 (2012).

[107] P. Roy, R. Lynch, and P. Schmuki, Electrochem. Commun. 11 1567 (2009).

[108] A. Imanishi, M. Tamura, and S. Kuwabata, Chem. Commun. 1775 (2009).

[109] T. Tsuda, T. Sakamoto, Y. Nishimura, S. Seino, A. Imanishi, and S. Kuwabata, Chem. Commun. 48 1925 (2012).

[110] H. Minamimoto, H. Irie, T. Uematsu, T. Tsuda, A. Imanishi, S. Seki, and S. Kuwabata, Chem. Lett. 44 312 (2015).

Publications list

< Papers >

1) R. Suda, M. Yagi, A. Kojima, R. Mentek, N. Mori, J. Shirakashi, and N. Koshida
   "Deposition of thin Si and Ge films by ballistic hot electron reduction in a solution-dripping mode and its application to the growth of thin SiGe films"
   Jpn. J. Appl. Phys. 54 (2015) 04DH11. DOI: http://dx.doi.org/10.7567/JJAP.54.04DH11
2) R. Suda, M. Yagi, A. Kojima, N. Mori, J. Shirakashi, N. Koshida
   "Reductive Deposition of Thin Cu Films Using Ballistic Hot Electrons as a Printing Beam"
   J. Electrochem. Soc. 163 (6) (2016) E1-E4. DOI: http://dx.doi.org/10.1149/2.0921606jes
3) R. Suda, M. Yagi, A. Kojima, N. Mori, J. Shirakashi, N. Koshida
   "Liquid-phase deposition of thin Si and Ge films based on ballistic hot electron incidence"
   Mater. Sci. Semicond. Process. 70 (2017) 44-49.
   DOI: https://doi.org/10.1016/j.mssp.2016.12.022

< International Conferences >

1) R. Suda, M. Ito, M. Yagi, A. Kojima, R. Mentek, N. Mori, J. Shirakashi and N. Koshida
   "Ballistic Electro-Deposition of Thin Si, Ge, and SiGe Films"
   2013 International Conference on Solid State Devices and Materials (SSDM 2013), September 24-27, 2013, Fukuoka, Japan.
2) R. Suda, M. Yagi, A. Kojima, J. Shirakashi, and N. Koshida
   "THIN Cu FILM DEPOSITION UNDER INCIDENCE OF BALLISTIC HOT ELECTRONS EMITTED FROM NANOCRYSTALLINE POROUS SILICON DIODE"
   Int. Conf. on Porous Semiconductors Science and Technology (PSST) 2016, March 24, 2016, 11-P2-10/452 (La Pineda, Tarragona-Costa Dorada; Spain).
3) R. Suda, M. Yagi, A. Kojima, N. Mori, J. Shirakashi, and N. Koshida
   "Criterion for Ballistic-electron Printing of Thin Metal and Group IV Films"
   2016 International Conference on Solid State Devices and Materials (SSDM 2016), September 26-29, 2016, Tsukuba, Japan.

4) R. Suda, M. Yagi, A. Kojima, N. Mori, J. Shirakashi, and N. Koshida
"Liquid-Phase Deposition of Thin Si and Ge Films Based on Ballistic Hot Electron Printing"
7th International Symposium on Control of Semiconductor Interfaces (ISCSI-VII), June 7-11, 2016, Nagoya University Chikusa-ku, Nagoya, Japan.

5) R. Suda, A. Kojima, N. Mori, J. Shirakashi, and N. Koshida
"Deposition mechanism of thin Si and Ge films promoted by liquid-phase reduction under ballistic hot electron incidence"
2017 International Conference on Solid State Devices and Materials (SSDM 2017), September 19-22, 2017, Sendai, Japan.

< Domestic Conferences >

1) 須田隆太郎、伊藤光樹、小島明、白樫淳一、越田信義
"ナノシリコン弾道電子源の還元効果による Si 薄膜堆積"
第 60 回応用物理学会春季学術講演会、28p-G6-6、2013 年春季、神奈川

2) 須田隆太郎、八木麻実子、小島明、Romain Mentek、白樫淳一、越田信義
"ナノシリコン弾道電子源を用いた Si, Ge, SiGe 薄膜の堆積"
第 61 回応用物理学会春季学術講演会、18p-E14-20、2014 年春季、神奈川

3) 須田隆太郎, 八木麻実子, 小島明, R. Mentek, 白樫淳一, 越田信義
"ナノシリコン弾道電子源を用いた Cu 薄膜のプリンティング堆積"
第 62 回応用物理学会春季学術講演会、11a-A29-4、2015 年春季、神奈川

4) 須田隆太郎, 八木麻実子, 小島明, 白樫淳一, 越田信義
"弾道電子の近接照射による Cu 薄膜のプリンティング堆積"
第 76 回応用物理学会春季学術講演会、14p-1C-7、2015 年秋季、愛知

5) 須田隆太郎, 八木麻実子, 小島明, 白樫淳一, 越田信義
"弾道電子の還元効果を利用した Cu 薄膜のプリンティング堆積"
第 63 回応用物理学会春季学術講演会、19p-S423-5、2016 年春季、東京

6) 須田隆太郎, 八木麻実子, 小島明, 白樫淳一, 越田信義
"ナノシリコン弾道電子源を利用した IV 族半導体薄膜のプリンティング堆積"
第 77 回応用物理学会秋季学術講演会、16a-B10-7、2016 年秋季、新潟

7) 須田隆太郎, 八木麻実子, 小島明, 白樫淳一, 越田信義
“弾道電子の近接照射による IV 族半導体薄膜のプリンティング堆積”
第 64 回応用物理学会春季学術講演会、17p-E206-6、2017 年春季、神奈川

8) 須田隆太郎, 小島明, 白樫淳一, 越田信義
“弾道電子照射による還元性薄膜堆積過程のモデリング”
第 78 回応用物理学会秋季学術講演会、6p-C21-6、2017 年秋季、福岡

Acknowledgements

I would like to express my sincere gratitude to Professor Jun-ichi Shirakashi for giving me valuable research opportunities and guidance on this research. I am grateful to Prof. Nobuyoshi Koshida for helpful advices on pursuing the study. Useful comments from Prof. Yoshiyuki Suda, Prof. Toshiyuki Sameshima, Prof. Tomo Ueno, and Associate Prof. Hiromasa Shimizu are greatly appreciated.

XPS, SIMS, and Raman spectroscopy measurements and analyses were made by helpful and fruitful advices from Dr. Toshikazu Shimada (Quantum 14), Prof. Nobuya Mori (Osaka Univ.), Mr. Hitoshi Kubo (Osaka Univ.), Ms. Nao Eguchi (Osaka Univ.), and Dr. Akihiro Tanaka (Tokyo City Univ.). The author thanks Dr. Toshiyuki Ohta for his help in the experiments.

I would like to thank the staffs of Quantum 14, Koshida Lab., Esashi Lab., and Shirakashi Lab. for their every help in many aspects during my studies here. In particular, Mr. Masamitsu Mori (Quantum 14), Dr. Naokatsu Ikegami (Tohoku Univ.), Dr. Akira Kojima (Tohoku Univ.), Dr. Romain Mentek (SanDisk), Mr. Mitsuki Ito (TUAT), Ms. Mamiko Yagi (TUAT), kindly supported my daily research activities.

My special thanks to my parents and older sister for their continuing support.